HEV Energy Management Considering Diesel Engine Fueling Control and Air Path Transients

HEV ENERGY MANAGEMENT CONSIDERING DIESEL ENGINE FUELING CONTROL AND AIR PATH TRANSIENTS

BY

YI HUO, B.A.Sc., (Mechanical Engineering)

Shanghai Jiaotong University, Shanghai, China

A THESIS

SUBMITTED TO THE DEPARTMENT OF MECHANICAL ENGINEERING

AND THE SCHOOL OF GRADUATE STUDIES

OF MCMASTER UNIVERSITY

IN PARTIAL FULFILMENT OF THE REQUIREMENTS

FOR THE DEGREE OF

PH.D. OF MECHANICAL ENGINEERING

Doctor of Philosophy (2018) McMaster University

(Mechanical Engineering) Hamilton, Ontario, Canada

TITLE:	HEV Energy Management Considering Diesel Engine Fueling Control and Air Path Transients
AUTHOR:	Yi Huo M.A.Sc., (Automotive Engineering) Shanghai Jiaotong University, Shanghai, China B.A.Sc., (Mechanical Engineering) Shanghai Jiaotong University, Shanghai, China
SUPERVISOR:	Dr. Fengjun Yan
NUMBER OF PAGES:	xviii, 167

This thesis is dedicated to my beloved father and mother

Abstract

This thesis mainly focuses on parallel hybrid electric vehicle energy management problems considering fueling control and air path dynamics of a diesel engine. It aims to explore the concealed fuel-saving potentials in conventional energy management strategies, by employing detailed engine models. The contributions of this study lie on the following aspects: 1) Fueling control consists of fuel injection mass and timing control. By properly selecting combinations of fueling control variables and torque split ratio, engine efficiency is increased and the HEV fuel consumption is further reduced. 2) A transient engine model considering air path dynamics is applied to more accurately predict engine torque. A model predictive control based energy management strategy is developed and solved by dynamic programming. The fuel efficiency is improved, comparing the proposed strategy to those that ignore the engine transients. 3) A novel adaptive control-step learning model predictive control scheme is proposed and implemented in HEV energy management design. It reveals a trade-off between control accuracy and computational efficiency for the MPC based strategies, and demonstrates a good adaptability to the variation of driving cycle while maintaining low computational burden. 4) Two methods are presented to deal with the conjunction between consecutive functions in the piece–wise linearization for the energy management problem. One of them shows a fairly close performance with

the original nonlinear method, but much less computing time.

Acknowledgements

This research was undertaken, in part, thanks to funding from the Natural Sciences and Engineering Research Council of Canada Discovery Grant Program and the FCA-LEAP program.

I would like to express my great gratitude to my supervisor, Dr. Fengjun Yan, for his support and guidance throughout my research. Under his supervision, I developed many skills to confront challenges and solve problems more effectively. These skills will help me a lot in all my future endeavors.

I would like to give my special thanks to my committee members, Dr. Emadi and Dr. Habibi, for their wise comments and valuable counsel during my Ph.D. study.

I would like to thank my family. Their unconditional love and support is the basis of keeping me on my way. I could never overcome so many difficulties without their help.

Contents

List of Tables

List of Figures

Chapter 1

Introduction

1.1 Background

Electrification and hybridization upon fuel-powered ground vehicles have attracted great interests of researchers in the past decade due to the increasing concerns about fossil fuel consumption and air pollution [1, 2]. A report in Fig. 1.1 from U.S. Department of Energy shows that sales of Hybrid Electric Vehicles(HEVs) have grown substantially in the U.S. market from 1999 to 2015. The main reason for this trend is the expectation that HEVs represent an effective and short-term approach to save fuel and reduce emissions. So what characteristics of HEVs make them draw people's attention? Specifically, in HEVs, an Internal Combustion Engine(ICE) and an Electrical Motor(EM) combine their power to move the vehicle. Compared to conventional vehicles, the presence of the additional energy source gives more freedom in delivering the requested power; therefore, more possibilities of shifting ICE operating points to efficient regions. For example, in the situation of low vehicle load, the engine in HEVs can simply shut down to avoid operating in low-speed-low-torque

regions, where the efficiency is low; HEVs can also improve its overall fuel economy in the whole driving cycle by maneuvering the output powers of the engine and motor; Besides, HEVs can regenerate part of vehicle kinetic energy and store it in the battery during braking stages [3, 4]. These advantages of HEVs are obviously unreachable in conventional vehicles in which ICEs are the only power source.

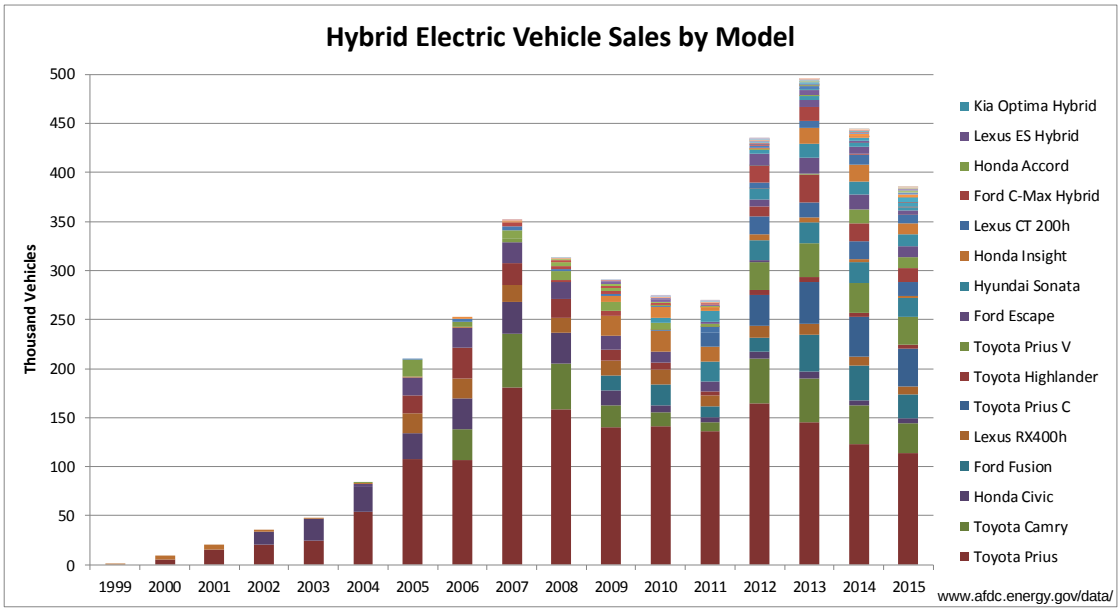

Figure 1.1: Summary of sales for Major HEVs in U.S. automotive market from year 1999 to 2015

There are three major HEV powertrain architectures: series, parallel and power split (also named as compound) [5–7]. The series topology is an electric–powered vehicle with an on-board charging system. The ICE can alway operate in the optimal torque–speed point which indicates the best efficiency. However, it needs both charging and discharging system, which leads to low efficiency and expensive cost. In the parallel topology, both ICE and motor are mechanically connected to the drive

train. It provides a higher level of hybridization than the series topology, and allows the torque distribution according to the requested driving demand. The complexity of structural and control is considered moderate in parallel HEVs. The power split topology normally uses a planetary gear set as a power split device. The multi–degree–of–freedom nature gives power split HEVs more opportunity of optimizing ICE and motor operating conditions. As a result, it is also the most complicated topology among the three and has the highest cost.

The studies in this thesis all adopt a parallel topology considering its moderate structural and control complexity. The coordinative control of multiple power devices is a major issue. To take advantage of the hybridization, the energy management or supervisory control problem has been proposed and researched extensively. The objective of HEV energy management is to reduce fuel consumption in a driving mission and satisfy the requirements from driver's demands, battery energy storage and the physical limits of components. There have been generally two trends that deals with HEV energy management problems: rule-based and optimization-based solutions. In paper [8], Farzad et al. gives a comprehensive overview of these two categories of strategies. Briefly, in rule-based methods, the "rules" are designed intuitively based on human expertise without a priori knowledge of a driving cycle and detailed vehicle models. It manages the on-board power distribution mainly according to "load level" and does not involve optimization [9–11].

Optimization-based strategies, however, exploit the hybrid powertrain system, process information from engine and motor operating conditions, gear shifting, acceleration and brake signals etc., and generate the setpoints for the individual control of each component. Normally, they form a cost function of decision variables

to minimize the fuel consumption either globally or instantaneously [12] [13]. The underlying mathematics of this group of strategies relies on optimal control theory, such as dynamic programming(DP), Pontryagin minimization principle(PMP) [14]. Optimization-based strategies have been implemented as off-line and on-line approaches. The off-line approach is performed over a known driving cycle and commonly a noncausal, globally optimal solution can be found. DP and PMP have been successfully adopted in off-line energy management problems [15–17], [18, 19]. For on-line implementations, the problem is updated by present conditions of vehicle powertrain and driving demand, so global optimality cannot be guaranteed and suboptimal solutions are admitted. The ideology of model predictive control(MPC) exceptionally aligns with the needs of on-line energy management strategies, because of its model–based, performance-index-driven nature, and receding horizon mechanism. MPC has been shown to be good candidates for generating near-optimal power split laws [20–22].

1.2 Motivation and contributions

Based on the literature review, in traditional energy management strategies, the engine is modeled by an efficiency map or brake specific fuel consumption (BSFC) map with regard to engine speed and torque. The engine torque is directly used as a decision variable in control law design. This implies two drawbacks of traditional strategies. First, the process of engine torque generation is not sufficiently explicated to exploit the benefits from hybridization. If the factors that strongly affect the engine torque, such as cylinder air charge, fuel injection and ignition control(for gasoline engines), are employed in energy management optimization as manipulated variables,

the flexibility of the control system increases and the potential of saving fuel can be explored further. For example, the fueling control in a diesel engine provides fuel mass flow rate and injection timing to obtain the best BSFC at the same output torque [23] [24]. The start time of injection affects the auto ignition in diesel engine so that the combustion and torque production change accordingly. Fig. 1.2 shows BSFC curves from paper [24]. It illustrates that an optimal injection timing at constant engine load and speed occurs where BSFC reaches its lowest point.

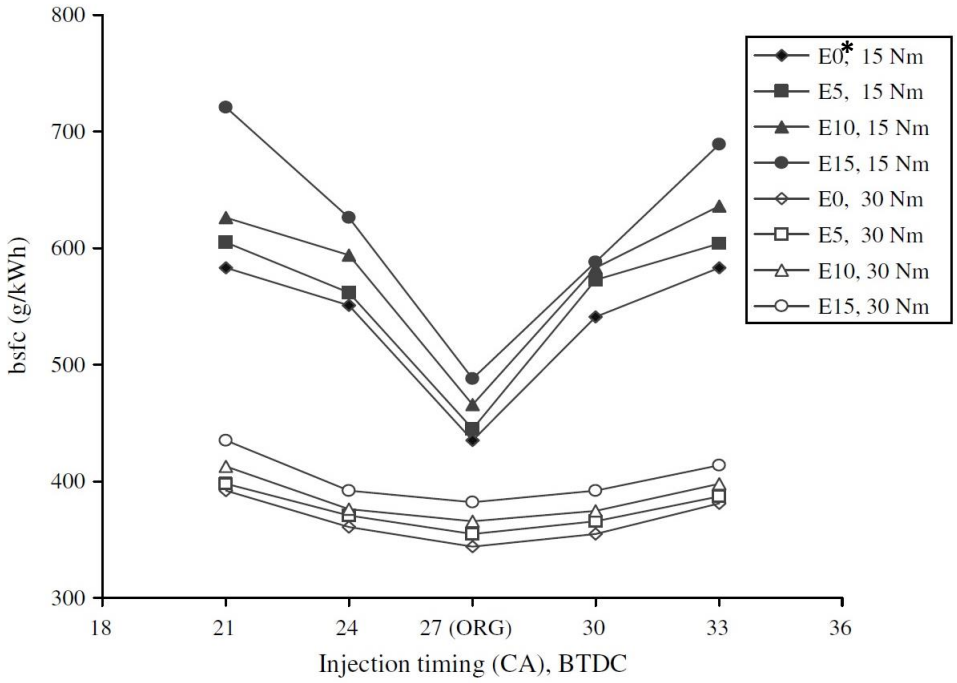

Figure 1.2: BSFC results at different injection timings and loads (1800 rpm).

*E0-E15 represent the volume ratio of ethanol in diesel fuel

The second shortcoming is that the inherited steady-state assumption leads to

inadequate analysis on engine transient behavior which adversely influences the decision of the supervisory controller. Given that the derived engine setpoints cannot be achieved instantly, especially in rapid transient processes, the expected powertrain output power is not guaranteed without delay. Therefore, energy management strategies tend to apply actions that spend more power due to the requirement of vehicle speed tracking. It could introduce extra fuel or battery energy consumption than predicted. The more delay of the engine torque response is, the more energy can be consumed. In paper [25] an experimental test shows the sluggish response of boost pressure and indicated mean effective pressure (IMEP) for a turbocharged diesel engine during 0-100% load transient at 1200 RPM. Paper [26] has proposed a multivariable controller to improve the abilities of tracking engine torque/speed trajectories generated from the HEV energy management strategy during transients, and revealed its benefit on fuel economy and emissions. However, it did not consider transients when deriving those trajectories. No matter how accurately the actual operating points can be controlled to approach the desired ones, the desired setpoints still cannot precisely predict the engine and hybrid powertrain torque. Hence, the original problem still cannot be solved. In [27,28], Martin et al. proposed a method to calculate the optimal transient control trajectories in a diesel-generator system. The trajectory that realizes the best fuel performance was successfully obtained when given step output power request in short-time driving missions. However, this method has not been verified for HEV energy management problems in a standard driving cycle, either through experiments or high–fidelity simulations.

The use of diesel engine in this research considers the utility of this engine type as an alternative to conventional SI–ICE HEVs. This idea is driven by the emergence of

homogeneous charge compression ignition (HCCI) that could be an advancement in diesel engine technologies. Motivated by the two aforementioned issues, it is necessary to properly incorporate a detailed diesel engine model into the energy management strategy to further improve fuel economy. The key elements of the expected model should reflect the main characters of engine torque generation and response. Fuel injection and air charge are two major factors for diesel engine control [29]. A few modern engine techniques, such as variable valve timing, exhaust gas recirculation, turbocharger, fuel split injection, etc, all aim to enhance the coordinative control of fuel and air in the cylinder to achieve better mixture, combustion, torque response and fuel economy [30–33]. When these techniques are employed to HEV energy management problems, the system complexity grows as more state and control variables are involved.

Thus, it is crucial to find an effective way to deal with these complexities, including nonlinearity, time-variant and multi-input-multi-output systems. To this end, the contributions of this thesis are listed as follows:

A. A new energy management strategy is developed for a parallel hybrid powertrain with a naturally aspirated diesel engine. By combining fuel injection timing control into an instantaneous optimal control algorithm based on Pontryagin minimization principle, the proposed strategy has an additional decision variable that makes it possible to move engine operating points to more efficient regions than strategies that do not. The improvement of the HEV fuel economy is verified by simulations conducted in GT-SUITE/Simulink platform.

B. An air path dynamic and engine transient torque model are adopted for a turbocharged diesel engine and calibrated through the simulation data from GT-SUITE. A four-state system is established for the studied HEV powertrain. An on-line model predictive energy management strategy is developed to minimize the fuel consumption in the finite receding horizon. The proposed strategy demonstrates the benefits on fuel saving by comparison to other strategies that do not capture engine transients.

C. Continuing with the problem in Contribution B, a novel learning framework is designed and incorporated with the MPC based energy management strategy to adaptively regulate control step according to the performance in the previous control horizon. The proposed method, which is referred as adaptive control-step learning MPC (ACLMPC), avoids intuitively selecting control step which may lead to poor control performance. Through the simulation results it demonstrates an excellent trade-off between the fuel economy and computational effort. Moreover, it shows a strong improvement of adaptability to the variation of driving cycle, while maintaining low computational effort.

D. In MPC based strategies, solving a nonlinear mathematical programming problem is time-consuming. In order to reduce the computational effort, linearization is conducted to obtain linear approximations of state equations, cost functions and constraint functions. Two linear methods with different function-conjoining approaches are compared with the original nonlinear method. The results show that the proposed linear method largely decreased the computing time and maintain fairly close fuel and SOC trajectories of the original method.

1.3 Thesis outline

The remaining parts of the thesis are organized as follows:

In Chapter 2, a technique of diesel engine fueling control is involved in optimization-based energy management strategy and shows its benefits on fuel economy.

In Chapter 3, an on-line supervisory controller considering transient characteristics of a turbocharged diesel engine is developed to improve the accuracy of the decision making in the energy management strategy and reduce fuel consumption.

In Chapter 4, a new mechanism, ACLMPC, is proposed to automatically regulate the control step when implementing the MPC based energy management strategy. It shows the benefit on fuel economy, computational effort and robustness.

Chapter 5 continues the work in Chapter 3 by linearizing related models and converting the original problem into a linear programming problem, which is less computationally expensive without sacrificing much accuracy.

In Chapter 6 the thesis is summarized and future work is discussed.

Chapter 2

Diesel engine fueling control application in HEV energy management strategies

This chapter includes the following **published** paper:

Huo, Yi, Fengjun Yan, and Daiwei Feng. "A hybrid electric vehicle energy optimization strategy by using fueling control in diesel engines." Proceedings of the Institution of Mechanical Engineers, Part D: Journal of Automobile Engineering (2018): 0954407017747372.

Huo, Yi is with the Department of Mechanical Engineering, McMaster University, Hamilton, ON L8S 4L8, Canada.

Fengjun Yan is with the Department of Mechanical Engineering, McMaster University, Hamilton, ON L8S 4L8, Canada.

Daiwei Feng is with School of Mechatronics Engineering, University of Electronic Science and Technology of China, China

Co-authorship declaration: The idea of adopting fueling control techniques in HEV energy management problems was jointly developed by me and Prof. Yan. I had primarily completed the strategy design and simulation in GT-SUITE. Prof. Yan gave me some suggestions about how to debug the program efficiently. He helped me develop the scenarios in the simulation to verify the idea. Dr. Feng gave me some helpful comments about paper writing and revision.

Abstract

This paper addresses a control scheme for a parallel hybrid vehicle powertrain by introducing fueling control techniques. Since a diesel engine is involved in the proposed configuration, the control of fuel injection mass and timing becomes a crucial issue. In this study, these two variables are selected as control inputs for the hybrid powertrain system. Meanwhile, an optimization-based control strategy is designed to solve the hybrid electric vehicle power management problem by incorporating engine brake specific fuel consumption characteristics with regard to fuel injection control variables. To show the advantages of the proposed control scheme, another optimization-based strategy with fixed fuel injection timing is developed and implemented for comparison. The influence of NOx emission is also considered in control strategy and simulation results to show that the proposed fuel control technique has limited impact on NOx emission but imposes a considerable improvement on fuel saving.

Kewwords: Fuel injection control, diesel engine, HEV energy management, optimal control, power distribution

2.1 Introduction

Over the past several decades, people have been focusing on energy saving technologies for ground vehicles due to concerns on increasing crude oil demand and stringent regulations on vehicle emissions. The hybrid electric vehicle (HEV), as a promising vehicle configuration, provides one of the most feasible solutions to reduce fuel consumption and air pollution without largely compromising vehicle performance [1]. HEVs are expected to have a considerable contribution to social and environmental requirements for both passenger cars and heavy-duty vehicles [2–4]. Architectures of HEVs have been extensively studied and several hybrid powertrain prototypes were developed [5, 6]. The layouts of three commonly used HEV architectures, as described by Emadi et al., [5] illustrate their characteristics: series HEV has at least one traction motor, one generator, and one engine integrated in powertrain; parallel HEV generally has one engine, traction motor, and one torque coupler; series–parallel combined HEV has two electric motors and a power split device, such as a planetary gear set. Based on different topological complexities and potential costs of these three types of HEVs, the parallel configuration is adopted in this paper since it does not require many design changes from conventional vehicle powertrains.

Commonly, a hybrid powertrain system is composed of two types of power sources, namely, internal combustion engines (ICEs) and electric motors (EMs). As a result of their dual-source property, a major challenge for controlling hybrid vehicles is energy management, which aims at determining power demands on mechanical and electrical sources. A properly optimized energy distribution can greatly improve the fuel performance of HEVs [7]. Three currently developed optimization-based energy management strategies are dynamic programming (DP), the equivalent consumption

management strategy (ECMS), and the Pontryagin minimization principle (PMP). The pros and cons of these strategies are comprehensively discussed in several papers [8–12]. This paper adopts the PMP approach to solve the energy management problem.

In the literature, there are a large number of studies addressing issues of HEV energy management [8, 13–17]. The majority of them focus on implementing an engine model based on performance maps with regard to engine torque and speed, ignoring other significant factors such as fuel path and air path controls, particularly in diesel engines [2, 17–19]. However, for a naturally aspirated diesel engine, which is proposed in the setup of this paper, fuel injection control is quite important from an engine control perspective. Fuel injection control involves two variables, fuel injection mass and timing. They have a large influence on the cylinder combustion, torque production, fuel consumption, and emissions of a diesel engine [20–22]. In the study by Sayin and Canakci [23], the effects of fuel injection timing are presented to show that at certain operation points with the same engine speed and torque, the value of brake specific fuel consumption (BSFC) can be reduced by up to 30% by regulating fuel injection timing to the "sweat" point. Advanced or retarded fuel injection timing can lead to a big difference on fuel economy because the combustion condition and cylinder pressure vary dramatically according to the change of fuel injection timing [22, 24]. However, commonly-used engine models in dealing with HEVs energy management problems do not consider the influence of fuel injection control. When applying such models in energy management problems, only engine torque and speed will be manipulated in their feasible regions rather than fuel injection control variables. Therefore, it may conceal the potential to further improve the fuel economy.

The main contribution of this paper is that we choose fuel injection mass and timing as engine control inputs for the studied parallel HEV. Thus, engine output torque can be modeled as a function of these two control inputs by given a particular engine speed. Moreover, engine fuel consumption and nitrogen oxide (NOx) emission are considered as functions of fuel injection mass and timing, and engine speed. The proposed energy management strategy instantaneously optimizes a cost function, which is the sum of fuel mass flow rate and state of charge (SOC) consumption rate at each step. To show the effectiveness of employing fuel injection control variables, two different optimization-based strategies are compared based on simulations in an FTP75 driving cycle, one with fixed fuel injection timing and one with optimized fuel injection timing. Meanwhile, due to the significance of NOx emission in diesel engine applications [25, 26], NOx emission (g/kwh) is involved as the emission index and added in the cost functions of both strategies. Particulate matter (PM) and noise, vibration, and harshness (NVH) are also two factors traditionally considered in diesel engine applications. However, PM and NVH trade-off are not addressed in this paper since we have limited resources to obtain the characteristics of NVH and PM.

This paper is organized as follows. In the next section, major components of the proposed HEV model are described. Then, the development of energy management strategies is explained. The simulation results on fuel consumption and vehicle performance for the strategies are then demonstrated and compared. Finally, conclusions are presented.

2.2 Plant model description

2.2.1 Model overview

In Figure 2.1, a free-body diagram illustrates the structure of the HEV powertrain and its control signals. As a parallel configuration, an ICE is connected to a automatic manual transmission via a pressure-controlled clutch, and the output of an EM is directly linked to the transmission and then connects to a Differential (DF). The engine torque and motor torque are coupled only when the clutch is fully engaged. This structure is selected because the powertrain is still controlled by the EM even when the clutch is disengaged.

The plant model of studied HEV is developed in GT-SUITE 7.3. Co-simulation between Matlab/ Simulink and GT-SUITE is conducted for the purpose of validating energy management strategies. The models used for the design of energy management strategies are described for each component in the following subsections, including engine, motor, battery, vehicle, etc. To be noted, the modeling approaches and parameters of the motor, battery, and vehicle are all replications of those in GT-SUITE. The engine is modeled based on quasi-static assumptions [27]. The maps that characterize fuel consumption and NOx emission are calibrated in the detailed engine model in GT-SUITE.

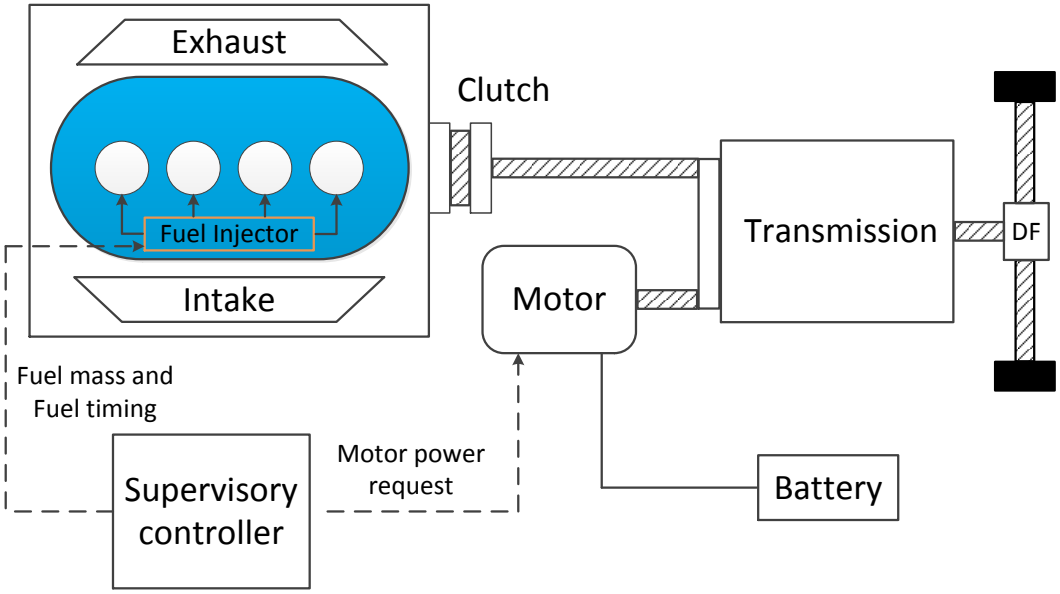

Figure 2.1: Schematic diagram of the parallel HEV powertrain system.

Some important model parameters are listed in Table 2.1. They are carefully chosen to satisfy the requirement of maximum power demand in the specific driving cycle.

Table 2.1: Parameters of HEV model

Component	Parameters	Values
Vehicle	Mass M_v	1900kg
	Frontal area A_f	1 m^2
	Air drag coefficient C_d	0.32
	Final Drive ratio(Differential)	3.2
	Tire rolling resistance C_r	0.015
	Tire rolling radius r_w	0.3m
	One wheel inertia	1.25 kg-m^2
Engine	Displacement	2.0L
	Maximum torque	183 Nm
Electric Motor	Motor max Torque	238 Nm
	Mortor max Power	25 kw
Battery	Capacity	20 Amp-h
	Modules	25
	Voltage per module	12.3 V
Transmission	1st/2nd/3rd speed ratio	2.125/1.36/0.72

2.2.2 Vehicle longitudinal model

A longitudinal vehicle dynamics model is adopted considering vehicle as a single mass. The driving torque and drag torque are both applied on the vehicle. The vehicle dynamic is given by

$$\frac{dV}{dt} = \frac{F_d - F_{drag}}{M_v r_w} \tag{2.1}$$

where V is vehicle speed, M_v and r_w are vehicle mass and tire rolling radius, and F_{drive} is the driving force provided by powertrain. The drag force, F_{drag}, which is the sum force resulting from road resistance and air drag effects, is defined as

$$\frac{dV}{dt} = \frac{1}{2}\rho A_f C_d V^2 + C_r M_v g \tag{2.2}$$

Here, ρ is air density and C_d is air drag force coefficient, A_f is frontal area, C_r is rolling resistance coefficient, and g is acceleration due to gravity.

The models of transmission, differential, and other drive shafts are simplified as gear ratios, and their inertias are lumped into vehicle inertia. The requested torque on vehicle wheels is scaled by gear ratios of the differential and transmission to obtain the requested torque on transmission input shaft.

2.2.3 Motor-battery system description

In studies of HEVs, the motorbattery system is normally composed of the mechanical and electrical parts. The mechanical part of the motor is an inertia system described as a first-order differential equation. For the electrical part, an efficiency map with respect to motor speed and torque is used to specify the relationship between the produced mechanical power and the required electrical power, as shown by

$$P_{ele,m} = \begin{cases} P_{mec,m}/\eta_m(T_{mec,m}, \omega_{mec,m}) & , T_m > 0 \\ P_{mec,m} \cdot \eta_m(T_{mec,m}, \omega_{mec,m}) & , T_m < 0 \end{cases} \tag{2.3}$$

$$T_{mec,\min}(\omega_{mec,m}) \leq T_{mec,m} \leq T_{mec,\max}(\omega_{mec,m}) \tag{2.4}$$

Here, the output mechanical power of the motor $P_{mec,m} = T_{mec,m} \cdot \omega_{mec,m}$. The actual motor torque $T_{mec,m}$ has both upper and lower limits $T_{mec,max}$ and $T_{mec,min}$, which are all functions of motor speed, as shown in Equation 2.3. Here η_m is motor efficiency with respect to motor torque and speed, which is inherited from the GT-SUITE HEV model.

An accurate battery model is extremely complicated and computationally inefficient considering thermal effects. Many studies on HEVs use simplified battery models ignoring thermal effects. In this paper, we only consider the electrical features of a battery. Consequently, three variables, open circuit voltage, V_{oc}, internal resistances during discharging, R_{dis}, and charging, R_{cha}, are involved. To be noted, these variables are all SOC-dependent. The battery current and output voltage can be calculated as follows

$$I = \frac{V_{oc} - V_b}{R_b} \tag{2.5}$$

$$V_b = \frac{P_{ele,m}}{I} \tag{2.6}$$

where R_b is the internal resistance of the battery depending on discharge and charge mode, I is the circuit current, and V_b is the battery output voltage. The characteristics of V_{oc} and R_b related to SOC are shown in Figure 2.2.

SOC can be obtained by integrating the current, as shown in Equation 2.7. When the current is positive, it means that the battery is discharging. On the other hand,

the battery is recharging if the current has a negative value.

$$SOC = SOC_{ini} - \int_0^t \frac{I}{Q_b} d\tau \tag{2.7}$$

Here, $SOCini$ is the initial value of SOC, and Q_b refers to the storage capacity of the battery.

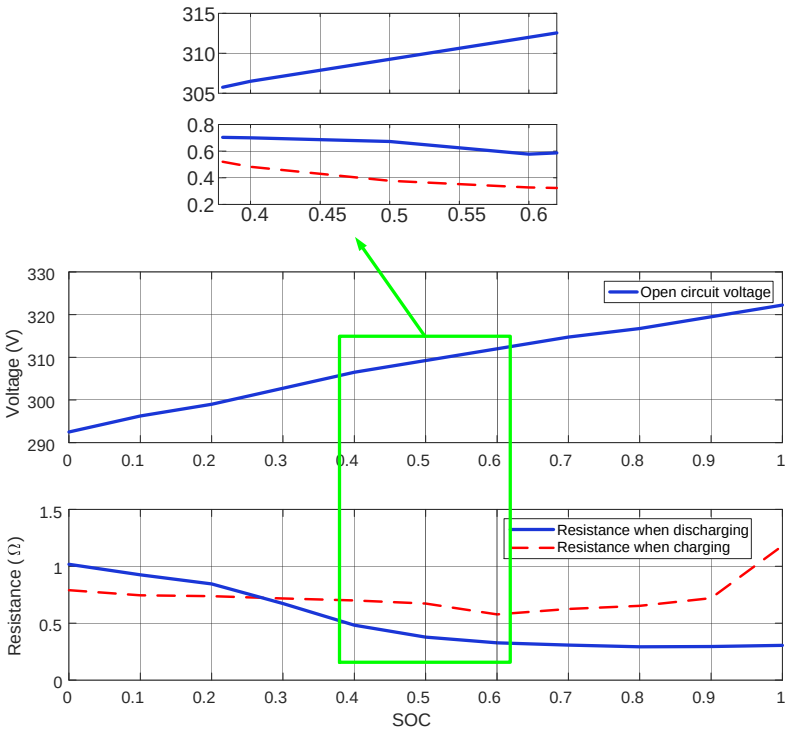

Figure 2.2: Battery open circuit voltage and internal resistance with respect to SOC.

2.2.4 Engine model

The plant model of engine used in this paper is a one-dimensional diesel engine model from GT-SUITE involving the dynamics of air path, fuel path, and combustion. This model has sufficient information to fulfill the requirements of fuel injection control. Engine BSFC and NOx emission are calibrated as maps with regard to three variables: engine speed, fuel injection mass and fuel injection timing. As the scope of this study focuses on a quasi-static problem, the situations in which fuel consumption and NOx emission may be affected by vehicle transient processes, such as start-stop and gear-shifts, are not involved in the strategy design. Therefore, the fuel injection control is determined based on those maps, which will be thoroughly illustrated in Section 2.3.

2.3 Control algorithm

2.3.1 Review of energy management strategies

As mentioned in the Introduction, three mainstream optimization-based strategies are DP, ECMS, and PMP. Generally, DP is almost a perfect method as it can guarantee the global optimality of fuel consumption in the entire driving cycle. However, the tremendous computational effort of its numerical implementation reveals that DP is extremely time-consuming. Thus, DP is barely utilized in real-time control but often considered as a benchmark for validating other strategies [8].

ECMS and PMP can be implemented as real-time energy management approaches. They have very similar form of cost function that is typically the sum of fuel energy and electrical energy consumption at each time step. Their cost functions are updated

and minimized at every time instance as the algorithm is proceeding forward. The major difference between PMP and ECMS is that they are conceived in different ways. PMP is formulated mathematically and can be proved as a necessary condition of the global optimality and even a sufficient condition in some special cases [28]. ECMS is developed intuitively based on experiences, and it is not a candidate of globally optimal solutions. However, ECMS and PMP have close connections. In fact, the cost function in ECMS can be viewed as an approximation of that in PMP [11]. Following PMP method, the proposed control strategy is formed below.

2.3.2 Architecture of control strategy

Figure 2.3 shows the control structure for the HEV powertrain. It mainly consists of a power split controller and a proportional–integral–derivative (PID) controller. The Feedforward PID controller first estimates the total requested power for driving the vehicle based on the vehicle acceleration and identified powertrain system, and then corrects it depending on the error between the actual and required vehicle speeds. As long as the requested power is sufficiently provided by the engine and motor, vehicle speed tracking performance can be guaranteed. The power split controller is the core of energy management strategies and decides control inputs for HEVs: fuel injection mass, fuel injection timing and power split ratio (abbreviated to split ratio) R_p. The split ratio is defined in Equations 2.8 and 2.9 as a proportion of engine requested power to total requested power.

$$P_{eng,req} = R_p P_{tot,req} \tag{2.8}$$

$$P_{mot,req} = (1 - R_p)P_{tot,req} \tag{2.9}$$

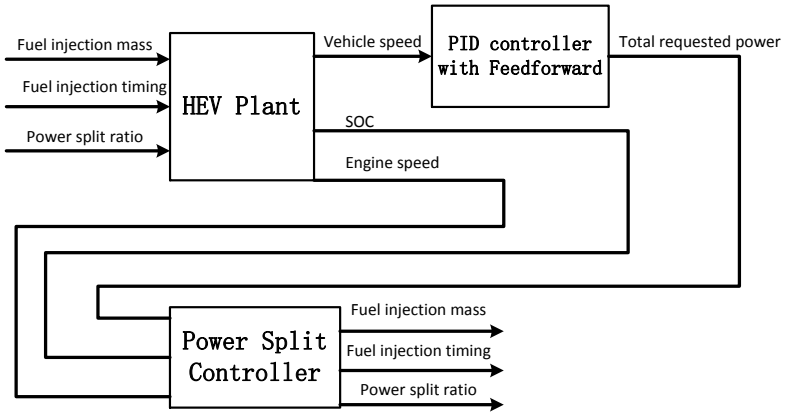

Figure 2.3: The structure of HEV powertrain control

Thus, the engine requested power $P_{eng,req}$ and the motor requested power $P_{mot,req}$ are calculated by giving the total power demand $P_{tot,req}$ and the split ratio.

In order to bridge fuel injection control variables and engine performances, maps of BSFC, engine torque, and NOx emission are calibrated in detailed engine model from GT-SUITE to obtain prior knowledge that is needed in energy management strategies. These maps use fuel injection mass and timing, engine speed as inputs. A predefined range of each input variable is applied on calibration to ensure the feasibility of engine operation. Figure 2.4 shows three two-dimensional band diagrams that illustrate BSFC, engine torque, and NOx emission with regard to the three inputs. Each diagram has four subplots that depict the characteristics at four constant engine speeds, 1200, 1600, 2000, and 3000 r/ min. Lines in different colors indicate different values of fuel injection mass. To be noted, the characteristics at other engine speeds (1000, 1400, 1800, 2500, 3500, 4000 r/min) are not shown but they are considered

in the calibration and energy management strategy designs. As shown in the figure, the BSFC value has obvious discrepancies when fuel injection timing is changed, but NOx emission stays relatively constant.

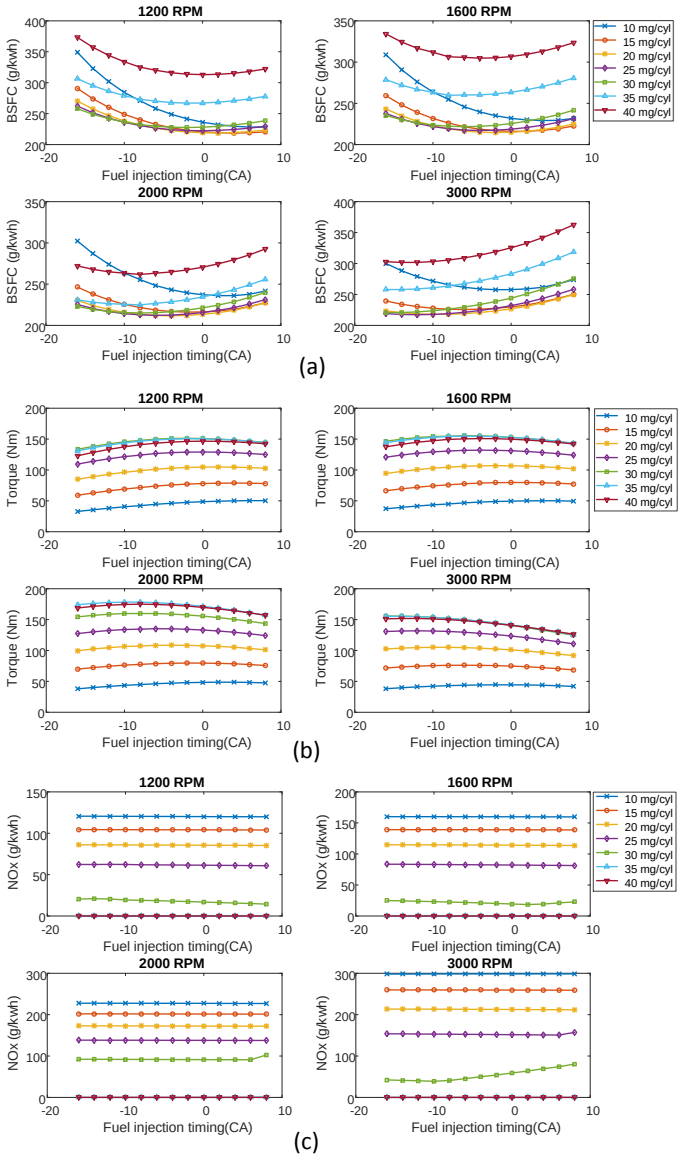

Figure 2.4: Diagram of BSFC (a), engine torque (b), and NOx emission g/kwh (c) with regard to engine speed, fuel injection mass, and fuel injection timing.

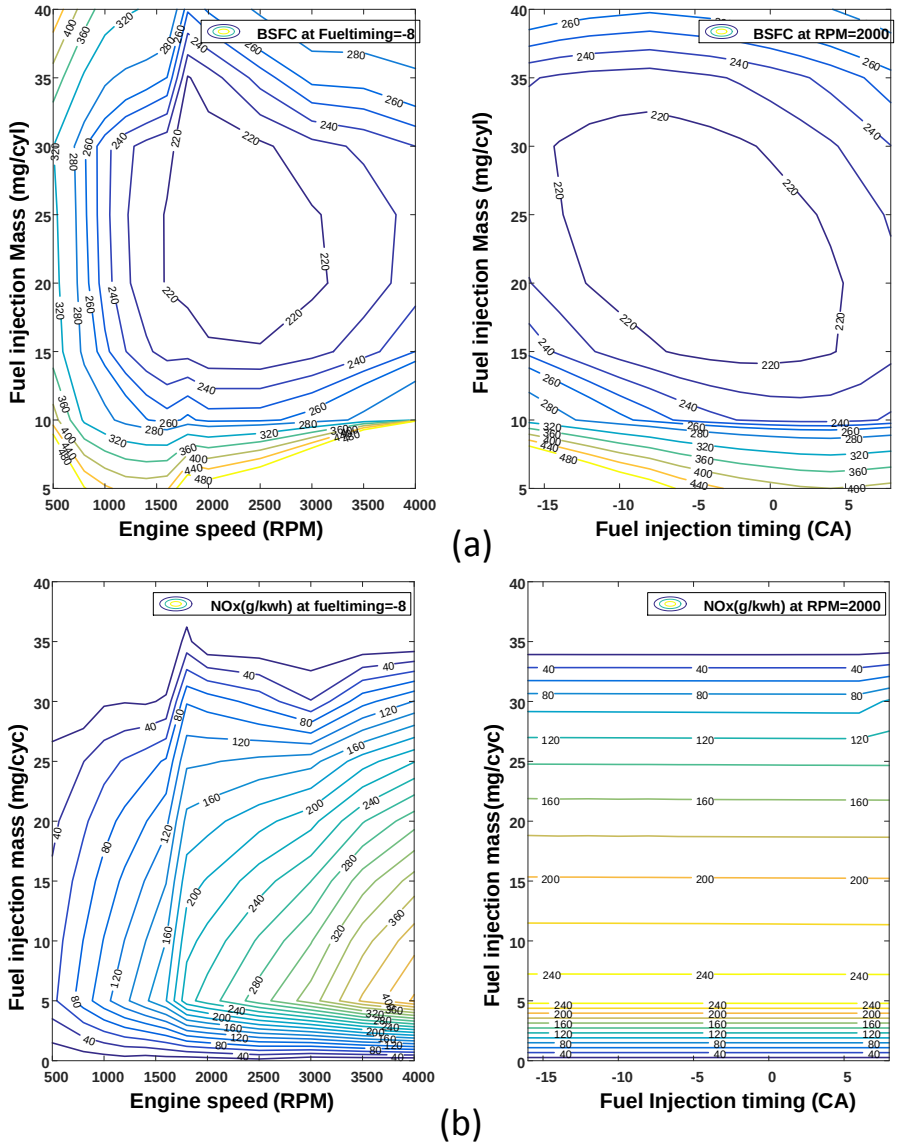

Figure 2.5: Contour maps with different x, y axis for BSFC, and NOx emission (the left figures of (a) and (b) use engine speed and fuel injection mass as x, y axis; the right figures of (a) and (b) use fuel injection timing and mass as x, y axis).

Figure 2.5 presents features of BSFC and NOx emission in the contour maps at constant fuel injection timings or engine speeds. For instance, the left figures in

Figure 5(a) and (b) are plotted by setting fuel timing as 28 CA; the right figures are plotted by setting engine speed at 2000 r/min.

The BSFC, engine torque, and NOx emission maps provide enough information for the design of an energy management strategy. Compared to the traditional engine model that only uses engine torque and speed as inputs, the proposed model offers another degree of freedom to control engine torque and fuel consumption. Although the model becomes more complicated, it gives more opportunities to save fuel.

2.3.3 Fuel consumption optimization

Combining Equations 2.3, 2.5, 2.6, 2.7 the state-space function is derived as

$$\dot{SOC} = f(SOC, \boldsymbol{u}) = -\frac{V_{oc} - \sqrt{V_{oc}^2 - 4R_b P_{mec,m}/\eta}}{2R_b Q_b} \tag{2.10}$$

Here, V_{oc} and R_b are SOC dependent; $P_{mec,m}$ relies on the vehicle operating condition and control vector $\boldsymbol{u} = [F_m, F_t, R_p]$, where F_m, F_t, and R_p are the fuel injection mass, fuel injection timing, and power split ratio, respectively. The value of η depends on operating condition of motor. When motor is providing energy, $\eta = \eta_m$, and when motor is regenerating energy, $\eta = 1/\eta_m$.

Following the procedure of PMP, a Hamiltonian function is defined as

$$H = \dot{m}_f(\boldsymbol{u}) + \lambda f(SOC, \boldsymbol{u}) \tag{2.11}$$

which is also the cost function. It instantaneously minimizes the total equivalent fuel cost comprised of that from both fuel path and electrical path. In Equation 2.11, $\dot{m}_f$

is the fuel flow rate given by

$$\dot{m}_f(\boldsymbol{u}) = BSFC(F_m, F_t, \omega_{eng}) \cdot R_p \cdot P_{tot,req} \tag{2.12}$$

and λ is a costate variable to be tuned.

Equation 2.12 describes fuel flow rate as a function of control variables and measurable variables. Engine speed ω_{eng} and total requested power $P_{tot,req}$ are measurable, and $P_{tot,req}$ comes from PID controller in the outer loop (see Figure 2.3). Thus, by considering ω_{eng} and $P_{tot,req}$ as known parameters, fuel flow rate becomes a function of control vector $\boldsymbol{u}$.

In PMP theory, the costate variable λ has an updating mechanism at each time step, as shown by

$$\dot{\lambda} = -\frac{\partial H}{\partial SOC} = -\lambda \frac{\partial f}{\partial SOC} \tag{2.13}$$

For a typical HEV, SOC is usually sustained in a relatively narrow range, for example, 0.4–0.6. Under this assumption, the function f is approximated to be irrelevant to SOC. Because little change of open circuit voltage and internal resistance occurs in the SOC range from 0.4 to 0.6, they can be seen as constants (see Figure 2.2). Thus, $f(SOC, \boldsymbol{u}) \approx f(\boldsymbol{u})$ and then $\dot{\lambda} \approx 0$. This means that variation of costate is negligible within the limited SOC range, and only its initial value λ_0 needs to be selected.

Once the initial value of costate is given, at every step Hamilton function is minimized to find optimal control variables, namely, fuel injection mass, fuel injection timing and power split ratio. These three variables drive the vehicle to a new operating point to get an updated Hamilton function to continue the iteration.

To be noted, at each step the minimization of cost function is a constrained

problem, meaning that the searching zones for all the variables involved should be confined to their limitations. To fulfill this, several constraint functions are defined. An important rule of driving cycle test is that drivers demand must be achieved. In this study, we use fuel injection variables to control engine output torque. As a consequence, an equality constraint is formed in Equation 2.14. Here, T_{eng} is the engine torque function which can be obtained from the map in Figure 2.4(b). As ω_{eng}, $P_{tot,req}$ are all known, the relationship among fuel mass, fuel timing, and split ratio is given by

$$P_{eng,req} = R_p P_{tot,req} = \omega_{eng} \cdot T_{eng}(F_m, F_t, \omega_{eng}) \tag{2.14}$$

According to the study by Grizzle [2], the main inequality constraints in dealing with HEV energy management problems are battery charge and discharge capability, motor power limits, SOC constraints, and the boundaries of engine control variables. So, the cost function is subject to the following inequalities

$$\begin{aligned} P_{mot,min} \leq (1 - R_p) P_{tot,req} \leq P_{mot,max} \\ F_{m,min} \leq F_m \leq F_{m,max} \\ F_{t,min} \leq F_t \leq F_{t,max} \\ SOC_{min} \leq SOC \leq SOC_{max} \end{aligned} \tag{2.15}$$

Here $F_{m,max}$, $F_{m,min}$ and $F_{t,max}$, $F_{t,min}$ are the upper and lower bounds of fuel injection mass and fuel injection timing. SOC range is from 0.3 to 0.7. Here, $P_{mot,min}$ and $P_{mot,max}$ can be derived from Equation 2.4 depending on motor speed. Besides, the electric power in discharging mode that can be provided by battery should be

restricted according to Equation 2.10, which also implies another upper bound of motor power defined as

$$P_{mec,m}/\eta \leq \frac{V_{oc}^2}{4R_b} \tag{2.16}$$

The two bounds of motor maximum power should be compared and the smaller value is applied.

2.3.4 Strategy considering NOx emission

NOx emission is employed in a modified Hamilton function given by

$$H = (1-\gamma)\dot{m}_f(\boldsymbol{u}) + \lambda f(SOC, \boldsymbol{u}) + \gamma NO_x(\boldsymbol{u}) \tag{2.17}$$

NOx function is obtained from calibrated map in Figure 2.4 with regard to control vector $\boldsymbol{u}$. Here γ is another factor that regulates the weight of NOx emission in the cost function. Other constraints and boundary conditions are the same as in fuel consumption problem. From Figure 2.5, we can see that the contours NOx emission and BSFC have opposite trends as x, y inputs are changing. Typically, it may require a tradeoff between fuel consumption and NOx emission. In this study, γ is manually selected without optimization aiming at comparing the results of NOx emission in different energy management strategies.

2.4 Simulation

2.4.1 Simulation results in fuel consumption problem

In the previous section, we discussed how to find optimal control solutions in the defined HEV energy management problem. This section will show the results of implementing two different strategies. One is involving all the control variables in vector $\boldsymbol{u}$ into the optimization problem, which is noted by "optimal fuel timing". In order to clarify the improvement by involving fuel injection control variables, another optimization-based strategy with fixed fuel injection timing is proposed as well, which is noted by "fixed fuel timing". In the second case, fuel injection timing F_t is set to a constant (-12 CA) in Equations 2.12 and 2.14, and only fuel injection mass and power split ratio can be manipulated. In other words, fuel injection timing is deprived of its influence on HEV powertrain system. Furthermore, gear shifting and engine ON/OFF control are all identical in both cases to avoid interferences from them. The values of costate λ in two cases are selected as 1200. The compared powertrain performances in these two cases will be shown and analyzed in the following figures. The first case is expected to save more energy than the second one because of its ability of optimizing fuel injection timing.

Both of two cases are simulated under the FTP75 driving cycle, as shown in Figure 2.6. We can see that vehicle speed tracking is perfectly achieved in both cases. Figure 2.7 illustrates engine torque and speed behaviors in the whole driving cycle. Identical results of engine speed in both cases indicate that the same gearshift and engine start–stop strategies are utilized. In addition, during vehicle deceleration, regenerative braking functions in two cases also share the same tactic, which is that

motor regenerates as much energy as possible and engine provides zero output torque. The power split controller is not activated during engine idle and vehicle deceleration, so the difference in the two cases of motor torque, engine torque, split ratio, SOC, etc., can be seen as direct outcomes from different energy management strategies.

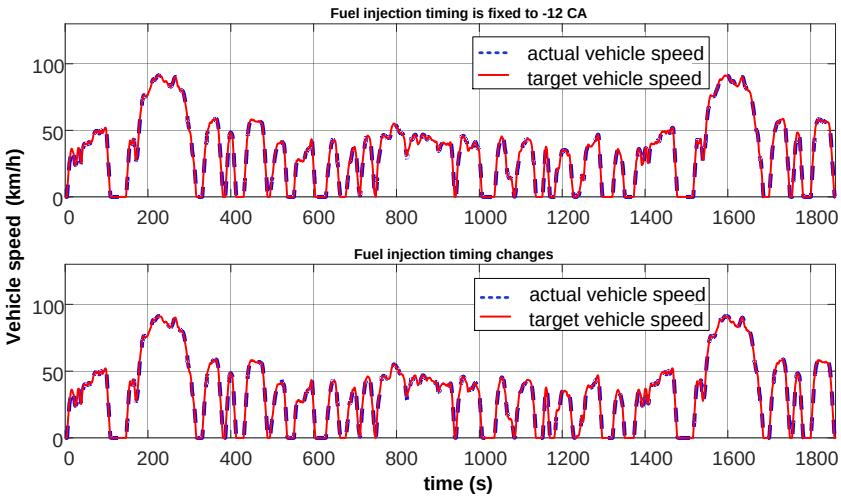

Figure 2.6: Comparison of vehicle speed tracking for variable fuel timing strategy and fixed fuel timing strategy

Figures 2.8 and 2.9 plot the fuel injection mass and timing behaviors in both overall cycle and zoom-in cycle (770–970 s). The differences between blue line and reddash line are caused by two control strategies. Obviously, these differences occur in the same time slots as in fuel injection mass and power split ratio curves in Figures 2.8 and 2.12. Optimal fuel timing strategy exploits fuel injection timing and adds another degree of freedom to the system. Therefore, the feasible range of BSFC can be expanded and smaller BSFC can be found. Consequently, engine operating points move to a more efficient region and overall efficiency for hybrid powertrain is increased.

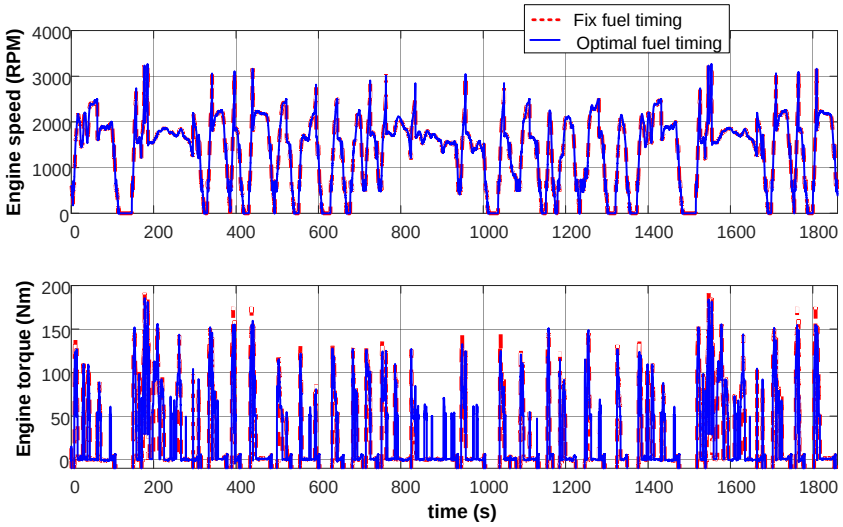

Figure 2.7: Comparison of engine speed and torque for variable fuel timing strategy and fixed fuel timing strategy

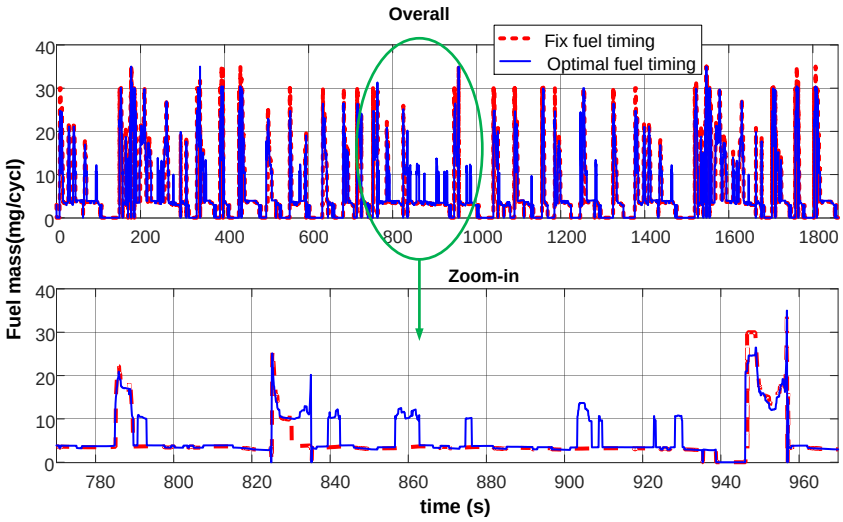

Figure 2.8: Comparison of fuel injection mass behavior for variable fuel timing strategy and fixed fuel timing strategy

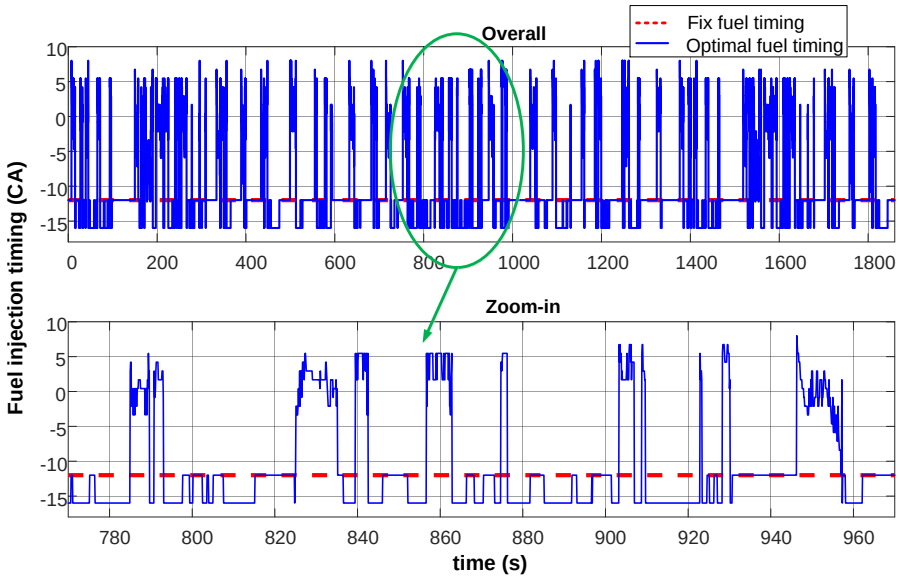

Figure 2.9: Comparison of fuel injection timing behavior for variable fuel timing strategy and fixed fuel timing strategy

Specifically, comparing two curves at 840 s, 860 s, and 905 s in Figures 2.8, 2.9, and 2.12 zoom-in figures, "optimal fuel timing" strategy tends to use more engine power instead of motor power than "fixed fuel timing" strategy. It is not difficult to conclude that engine efficiency increases to the point where "optimal fuel timing" strategy has to make the changes. Moreover, because engine efficiency also depends on engine operating condition, at some cycle points these changes are evident but others are not.

Fuel consumption and SOC results are shown in Figure 2.11. At the end of driving cycle, the fuel consumptions in "optimal fuel timing" strategy and "fix fuel timing strategy" are 653 g and 624 g, respectively, and the final SOCs in two cases are 0.59 and 0.53. It means "optimal fuel timing" case consumes more fuel energy instead of electrical energy than in "fix fuel timing" case, so its SOC ends up with a

higher level. Because the two energy management strategies use the same structure of cost function and identical constant costate, the integrals of cost function can be introduced to compare total equivalent fuel consumption instead of only actual fuel consumption. In order to calculate the total energy cost, the following equation is utilized by integrating Equation 2.18.

$$F_{total} = \sum \dot{m}_f(t)\Delta t + \lambda(SOC(t) - SOC(t_0)) \quad t \in [t_0, t_e] \tag{2.18}$$

Here, t_e and t_0 are the end time and initial time. As mentioned, equal value of λ in both cases is used to convert electrical energy to fuel energy.

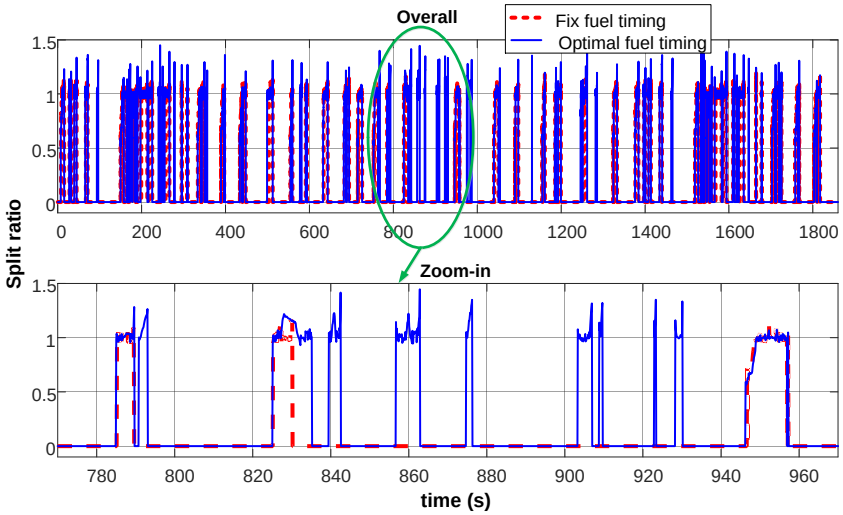

Figure 2.10: Comparison of split ratio behavior in variable fuel timing strategy and fixed fuel timing strategy

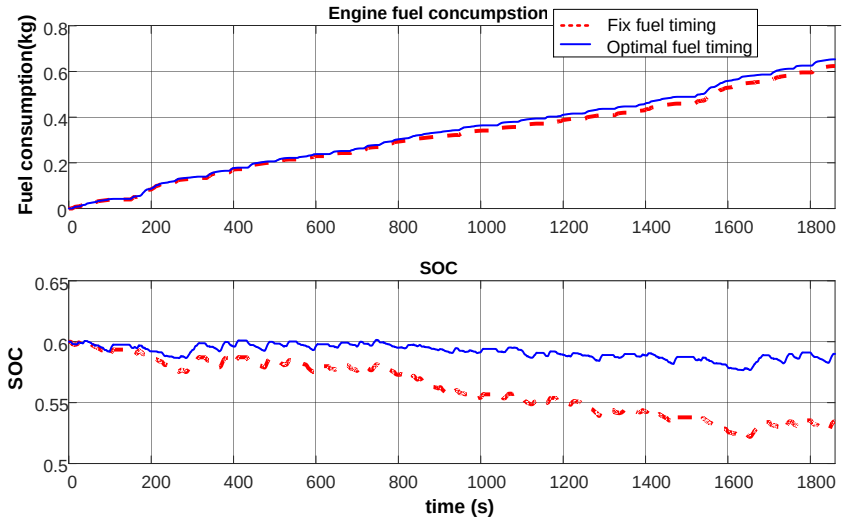

Figure 2.11: Comparison of engine fuel consumption and SOC in variable fuel timing strategy and fixed fuel timing strategy

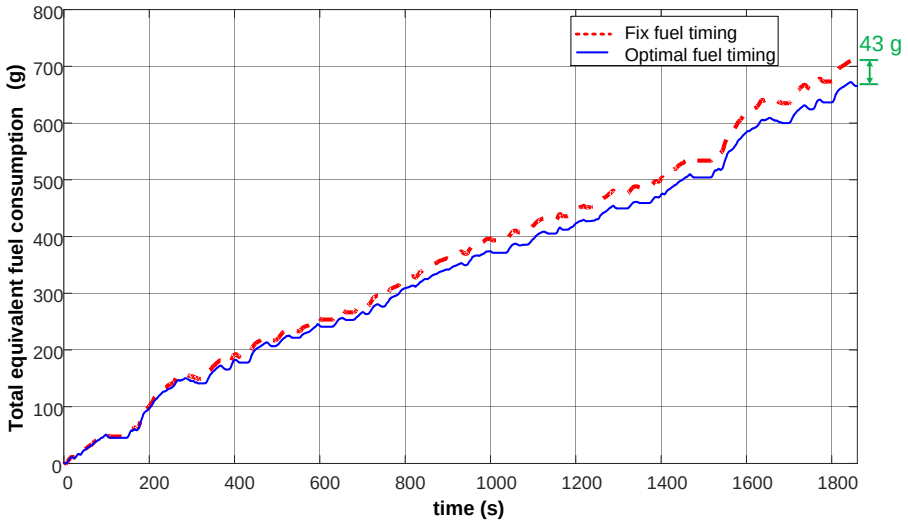

Figure 2.12: Total equivalent fuel consumption for variable optimal control and fixed timing optimal control

Figure 2.12 shows the calculated equivalent fuel consumption in the FTP75 cycle.

It turns out that "optimal fuel timing" case has 665 g equivalent fuel cost, which is 43 g less than 708 g in "fixed fuel timing" case.

2.4.2 Results considering NOx emission

This part shows performances of SOC, NOx on conditions of different γ in Equation 2.17. γ is chosen from [0, 0.01, 0.1]. Similarly, two control strategies are compared as follows.

Figure 13 shows the accumulated NOx emission mass by integrating instantaneous NOx mass flow rate in two control strategies. No matter how parameter γ changes, the behaviors of accumulated NOx are almost the same in "fixed fuel timing" and "optimal fuel timing" strategies. The final NOx productions in Table 2.2 indicate that using both strategies NOx emissions end up with less than 0.5% difference.

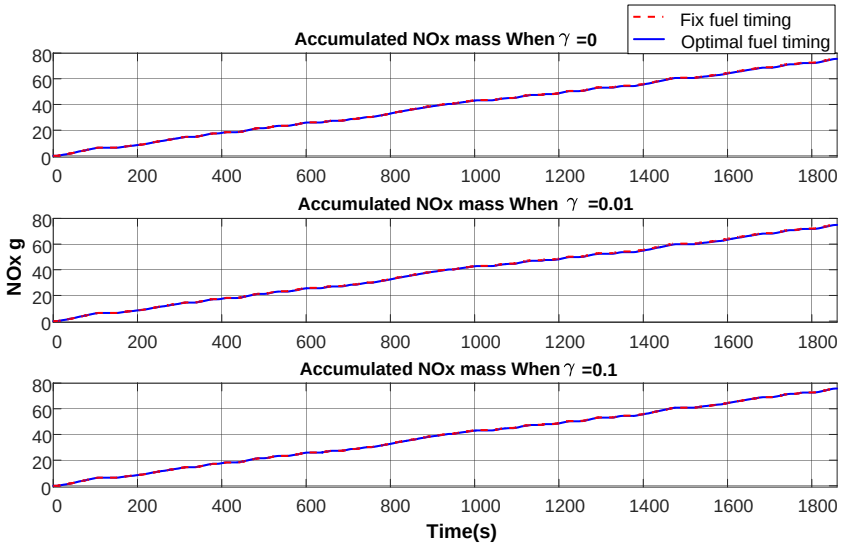

Figure 2.13: Integrated NOx mass versus time using strategies when γ=0, 0.01, 0.1

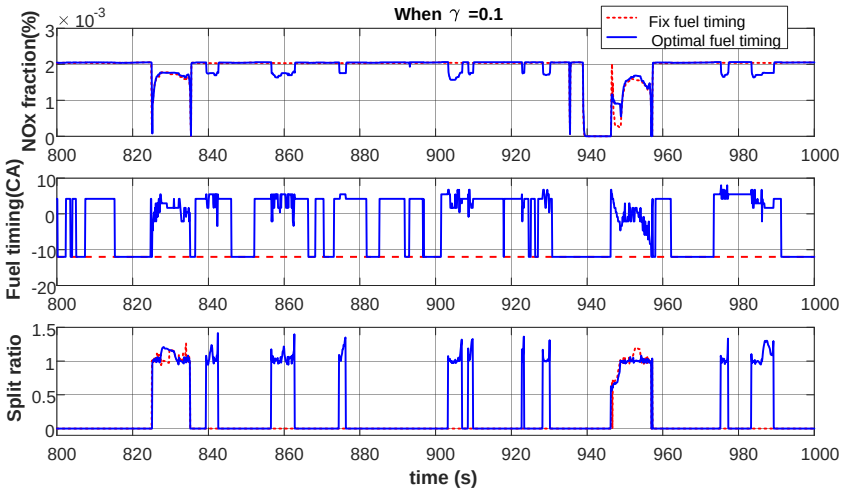

Figure 2.14: NOx fraction, NOx mass flow rate and split ratio compared in different fuel control strategies when γ=0.1

Table 2.2: NOx emission mass at the end of driving cycle

Control Strategy	γ values	Final NOx mass(g)
Optimal fuel timing	0	75.7
	0.01	75.5
	0.1	74.9
Fixed fuel timing	0	75.5
	0.01	75.7
	0.1	75.3

Figure 2.14 plots curves of NOx fraction (%), fuel injection timing, and power split ratio when costate γ is set to 0.1. From the curves of power split ratio, we can see decisions of power distribution made in both strategies. At 840 s, 860 s, and 905 s, the

difference of two power split ratios indicates that in "optimal fuel timing" case engine consumes more fuel (also see Figure 2.8) but decreases NOx fraction. This proves the consistence with the "trade-off" on BSFC and NOx emission maps in Figure 2.4.

At time 830 s and 950 s, both power split ratio curves are very close. Although fuel injection timings have obvious differences, NOx fraction hardly changes. Thus, fuel injection timing has quite little impact on NOx emission. This is also consistent with the conclusion discussed in Figure 2.5.

2.5 Conclusions

This paper proposes an energy management strategy for a parallel hybrid powertrain with a naturally aspirated diesel engine. Fuel injection mass and timing are considered as two control variables for the diesel engine due to their influence on BSFC and NOx emission. Therefore, characteristics of BSFC, NOx emission, and engine torque with regard to fuel injection mass and timing are calibrated through GT-SUITE models. To demonstrate the effects of fuel injection control on HEV powertrain system, two optimization-based algorithms, one with fixed fuel timing and another with optimal fuel timing, are developed. The idea of PMP is adopted to solve the optimal control problem of minimizing fuel consumption. In addition, NOx emission is also considered in the development of energy management strategy. The total fuel consumption is calculated by adding engine fuel consumption and equivalent fuel cost from the electrical path. Comparative simulation results in the FTP75 cycle show that the strategy with optimal fuel injection timing has 5% less total equivalent fuel consumption than that in fixed fuel timing strategy. The results considering NOx emission demonstrate that the variation of fuel injection timing has very limited

influence on NOx production in the proposed range of fuel injection timing.

Reference

[1] Gurkaynak Y, Khaligh A and Emadi A. State of the art power management algorithms for hybrid electric vehicles 2009; : 388–394.

[2] Grizzle JW et al. Power management strategy for a parallel hybrid electric truck. *IEEE transactions on control systems technology* 2003; 11(6): 839–849.

[3] Serrao L, Sciarretta A, Grondin O et al. Open issues in supervisory control of hybrid electric vehicles: A unified approach using optimal control methods. *Oil & Gas Science and Technology–Revue dIFP Energies nouvelles* 2013; 68(1): 23–33.

[4] Salmasi FR. Control strategies for hybrid electric vehicles: Evolution, classification, comparison, and future trends. *IEEE Transactions on vehicular technology* 2007; 56(5): 2393–2404.

[5] Emadi A, Rajashekara K, Williamson SS et al. Topological overview of hybrid electric and fuel cell vehicular power system architectures and configurations. *IEEE Transactions on Vehicular Technology* 2005; 54(3): 763–770.

[6] Chan CC, Bouscayrol A and Chen K. Electric, hybrid, and fuel-cell vehicles: Architectures and modeling. *IEEE transactions on vehicular technology* 2010; 59(2): 589–598.

[7] Van Berkel K, Hofman T, Vroemen B et al. Optimal control of a mechanical hybrid powertrain. *IEEE Transactions on Vehicular Technology* 2012; 61(2): 485–497.

[8] Yuan Z, Teng L, Fengchun S et al. Comparative study of dynamic programming and pontryagins minimum principle on energy management for a parallel hybrid electric vehicle. *Energies* 2013; 6(4): 2305–2318.

[9] Baumann BM, Washington G, Glenn BC et al. Mechatronic design and control of hybrid electric vehicles. *IEEE/ASME Transactions On Mechatronics* 2000; 5(1): 58–72.

[10] Bayindir KÇ, Gözüküçük MA and Teke A. A comprehensive overview of hybrid electric vehicle: Powertrain configurations, powertrain control techniques and electronic control units. *Energy Conversion and Management* 2011; 52(2): 1305–1313.

[11] Guardiola C, Pla B, Onori S et al. Insight into the hev/phev optimal control solution based on a new tuning method. *Control Engineering Practice* 2014; 29: 247–256.

[12] Sciarretta A and Guzzella L. Control of hybrid electric vehicles. *IEEE Control systems* 2007; 27(2): 60–70.

[13] Kermani S, Delprat S, Guerra TM et al. Predictive energy management for hybrid vehicle. *Control Engineering Practice* 2012; 20(4): 408–420.

[14] Sampathnarayanan B, Onori S and Yurkovich S. An optimal regulation strategy with disturbance rejection for energy management of hybrid electric vehicles. *Automatica* 2014; 50(1): 128–140.

[15] Nüesch T, Elbert P, Flankl M et al. Convex optimization for the energy management of hybrid electric vehicles considering engine start and gearshift costs. *Energies* 2014; 7(2): 834–856.

[16] Borhan H, Vahidi A, Phillips AM et al. Mpc-based energy management of a power-split hybrid electric vehicle. *IEEE Transactions on Control Systems Technology* 2012; 20(3): 593–603.

[17] Lin CC, Peng H and Grizzle J. A stochastic control strategy for hybrid electric vehicles. In *American Control Conference, 2004. Proceedings of the 2004*, volume 5. IEEE, pp. 4710–4715.

[18] Sciarretta A, Back M and Guzzella L. Optimal control of parallel hybrid electric vehicles. *IEEE Transactions on control systems technology* 2004; 12(3): 352–363.

[19] Delprat S, Lauber J, Guerra TM et al. Control of a parallel hybrid powertrain: optimal control. *IEEE transactions on Vehicular Technology* 2004; 53(3): 872–881.

[20] Agarwal AK, Srivastava DK, Dhar A et al. Effect of fuel injection timing and pressure on combustion, emissions and performance characteristics of a single cylinder diesel engine. *Fuel* 2013; 111: 374–383.

[21] Gumus M, Sayin C and Canakci M. Effect of fuel injection timing on the injection, combustion, and performance characteristics of a direct-injection (di) diesel engine fueled with canola oil methyl ester- diesel fuel blends. *Energy & fuels* 2010; 24(5): 3199–3213.

[22] Heywood JB et al. Internal combustion engine fundamentals 1988; .

[23] Sayin C and Canakci M. Effects of injection timing on the engine performance and exhaust emissions of a dual-fuel diesel engine. *Energy conversion and management* 2009; 50(1): 203–213.

[24] Sahoo B, Sahoo N and Saha U. Effect of engine parameters and type of gaseous fuel on the performance of dual-fuel gas diesel enginesa critical review. *Renewable and Sustainable Energy Reviews* 2009; 13(6-7): 1151–1184.

[25] Teiner P and Schneeweiss B. Evaluation of nox and fuel consumption reduction potential of parallel diesel-hybrid powertrains using engine-in-the-loop simulation. No. 2010-32-0128. Technical report, SAE Technical Paper, 2010.

[26] Grondin O, Thibault L and Quérel C. Transient torque control of a diesel hybrid powertrain for nox limitation. *IFAC Proceedings Volumes* 2012; 45(30): 286–295.

[27] Kolmanovsky I, Van Nieuwstadt M and Sun J. Optimization of complex powertrain systems for fuel economy and emissions. In *Control Applications, 1999. Proceedings of the 1999 IEEE International Conference on*, volume 1. IEEE, pp. 833–839.

[28] Kim N and Rousseau A. Sufficient conditions of optimal control based on pontryagins minimum principle for use in hybrid electric vehicles. *Proceedings of the*

Institution of Mechanical Engineers, Part D: Journal of Automobile Engineering 2012; 226(9): 1160–1170.

Symbol I

PID are defined in the Symbol II as coefficients that directly multiplies the speed error, and the integral, derivative of speed error. The calculated products should multiply vehicle mass before they are used in the simulation.

A_f	frontal area	1 m^2
f	the studied system state equation	
g	gravitational acceleration	9.8 m/s^2
$\dot{m}_f$	fuel flow rate	
r_w	tire rolling radius	0.3 m
$\boldsymbol{u}$	control input	
C_r	rolling resistance coefficient	0.015
C_d	air drag force coefficient	0.32
F_{drive}	driving force provided by powertrain	
F_{drag}	drag force	
F_m	fuel injection mass	
$F_{m,min}$	minimum fuel injection mass	0 mg/cycle
$F_{m,max}$	maximum fuel injection mass	40 mg/cycle
F_t	fuel injection timing	
$F_{t,min}$	minimum fuel injection timing	-16 crank angle
$F_{t,max}$	maximum fuel injection timing	8 crank angle
H	Hamiltonian equation	
I	the circuit current	
M_v	vehicle mass	1900 kg
$P_{mec,m}$	motor output power	

$P_{mot,req}$	motor power demand	
$P_{ele,m}$	motor electrical power	
$P_{mot,min}$	motor minimum power limit	-25 kw
$P_{mot,max}$	motor maximum power limit	25 kw
$P_{tot,req}$	total power demand	
$P_{eng,req}$	engine power demand	
Q_b	capacity of battery	20 A-h
R_{dis}	battery internal resistance when discharging	
R_{cha}	battery internal resistance when charging	
R_p	power split ratio	
SOC	battery state of charge	
SOC_{ini}	initial battery state of charge	0.6
SOC_{min}	minimum SOC limit	0.2
SOC_{max}	maximum SOC limit	0.8
T_{eng}	engine output torque	
$T_{mec,m}$	motor output torque	
$T_{mec,max}$	motor maximum torque limit	
$T_{mec,min}$	motor minimum torque limit	
V	vehicle speed	
V_{oc}	open circuit voltage	
V_b	battery output voltage	
γ	the weight of NOx emission in cost function	
η	motor efficiency	
η_m	motor efficiency when providing power	

λ	costate variable in cost function	1200 g/h
ρ	air density	1.225 kg/m^3
$\omega_{mec,m}$	motor speed rad/s	
PID	PID controller parameters in driver model	P=1,I=0.1,D=0

Chapter 3

MPC-based energy management strategy considering engine air path transients

This chapter includes the following **published** paper:

Huo, Yi, and Fengjun Yan. "A Predictive Energy Management Strategy for Hybrid Electric Powertrain with a Turbocharged Diesel Engine." Journal of Dynamic Systems, Measurement, and Control (2018). Doi: 10.1115/1.4039216.

Huo, Yi is with the Department of Mechanical Engineering, McMaster University, Hamilton, ON L8S 4L8, Canada.

Fengjun Yan is with the Department of Mechanical Engineering, McMaster University, Hamilton, ON L8S 4L8, Canada.

Co-authorship declaration: The idea of involving air path dynamic model in HEV energy management strategy is primarily devised by me. Inspired by Prof. Yan,

I proposed a model predictive control mechanism to solve this problem. Prof. Yan helped me clarify the contribution of this paper and correct some mistakes made by me at the beginning. He also helped me with the revisions of the paper.

Abstract

This paper proposes an energy management strategy for a Hybrid Electric Vehicle with a turbocharged diesel engine. By introducing turbocharger to the HEV powertrain, air path dynamics of engine becomes extremely complex and critical to engine torque response during transient processes. Traditional strategy that adopts steady–state–map based engine model may not work properly in this situation as a result of its incapability of accurately capturing torque response. Thus, in this paper a physical-law based air path model is utilized to simulate turbo "lag" phenomenon and predict air charge in cylinder. Meanwhile, engine torque boundaries are obtained on the basis of predicted air charge. A receding horizon structure is then implemented in optimal supervisory controller to generate torque split strategy for the HEV. Simulations are conducted for three cases: the first one is rule–based torque–split energy management strategy without optimization; the second one is online optimal control strategy using map–based engine model; the third one is online optimal control strategy combining air path loop model. The comparison of the results shows that the proposed third method has the best fuel economy of all and demonstrates considerable improvements of fuel saving on the other two methods.

Keywords: Air path dynamics, Turbocharger, HEV, Model predictive control, Transient process

3.1 Introduction

Hybrid Electric Vehicles(HEVs) exhibit a great capability of improving fuel economy compared with conventional vehicles by introducing an on–board electrical energy storage device to the powertrain system. The presence of the additional energy source gives another degree of freedom in delivering the requested power that is used for driving the vehicle. The coordinative control of both internal combustion engine(ICE) and electric motor(EM) gives potentials to increasing the overall efficiency of the system. Among different HEV powertrain topologies, parallel is a simple configuration that can be easily realized with minor modification on traditional vehicles [1] [2]. Several major automakers, such as Honda, GM and VW all have parallel Hybrid Electric Vehicles in the market. The energy management strategy for a parallel configuration is also named as torque split strategy because engine and motor speeds are coupled most of time and their torques can be distributed freely [3]. Many papers have proposed different methods of optimally realizing torque split, which can be categorized into three classes: dynamic programming (DP), Pontryagin minimization principle (PMP) and equivalent consumption management strategy (ECMS) [4] [5] [6] [7]. DP is promised to be a globally optimal solution to general problems. However, the huge computational load and the request for a complete prior information of driving cycle make its real–time implementation highly improbable; PMP is usually considered as a necessary condition of global optimization which can be derived from DP, paper [8] shows properly tuned PMP can obtain very similar results to DP. ECMS is a simplified way to realize PMP if the equivalent factor is appropriately chosen [9]. Although ECMS can be applied as close–loop controller in order to reduce the effect of model uncertainties, the instantaneous optimization in

ECMS still lacks abilities of predicting system behaviors. From this point of view, some researchers propose strategies based on model predictive control (MPC) and apply dynamic optimization over a finite moving horizon [10] [11] [12], which shows good fuel economy performance under standard driving cycles.

So far as known, the efficiency of an ICE in ground vehicle application is averagely around 20% and drifts within a large range depending on operating points. However, the electrical path including battery, motor and converter, has much higher and steadier efficiency performance than the fuel energy source. This implies that the efficiency improvements on engine may have more notable effects on vehicle system.

There are varieties of cutting–edge technology applied on modern ICEs to reduce fuel consumption and emissions, such as variable valve timing, exhaust gas recirculation, turbocharger, direct injection, etc. To be noted, in recent years turbocharger becomes more and more prevalent in the automotive industry to serve the purpose of downsizing ICEs and improving fuel efficiency. In general, a turbocharged engine makes use of exhaust gas energy and boosts the air charge to increase output torque and power. As a result, engine operating efficiency is increased and its displacement is allowed to be shrunk due to the existence of turbocharger. Obviously, this advantage aligns with the needs of engine in the HEV applications since a smaller engine can save space and reduce weight without losing power.

However, turbocharger technology also brings challenges to supervisory controller design attributed to its transient characteristic. In fact, engine torque may not respond fast enough to drivers requirement due to the sluggish effect of a turbocharger. In paper [13] and [14] engine torque behavior in 0–100% load transient process is investigated. The results show that in the worst case it lasts nearly 8 second for

the torque to reach steady state due to the slow increase of cylinder air charge. In order to visually explain the issue, a simulation test in similar operating conditions is conducted in GT–Power. Fig. 3.1 illustrates a process during 50% to 100% load step change at 1500 engine speed by shifting fuel injection per cycle from 40mg to 80mg. The output torque trajectory can be divided into two sequential portions. The first one represents the duration of fast response during which almost an instant torque change occurs, because the torque rise in this duration mainly depends on the fuel injection rise and fuel injection dynamics is very fast. The second portion is the slow response, where the torque continues increasing for about 5 seconds until it is stable. The air charge in this duration limits the fuel injection mass and the output torque. Therefore, the slower torque response is a reflection of the air charge dynamics. Meanwhile, an evident BSFC(Brake Specific Fuel Consumption) fluctuation in this process is also shown and it has an effect on the final fuel consumption.

In most of aforementioned energy management strategies, BSFC maps are normally involved to calculate fuel consumption. Control signals in those strategies are derived under the assumption that the engine can instantly provide the same torque as that in steady state by giving the same demand. The inaccuracy of the steady–state model in transient processes may lead to mismatch between the expected fuel consumption given by the controller and the actual one. In other words, the potential of improving fuel economy is concealed by an inadequate accuracy of model. Motivated by the problem discussed above, an effective transient model of a turbocharged engine is employed and MPC based supervisory controller is developed in this paper. The contribution primarily lies on systematically incorporating engine transient torque model including air path dynamics with an online optimization–based energy

management mechanism.

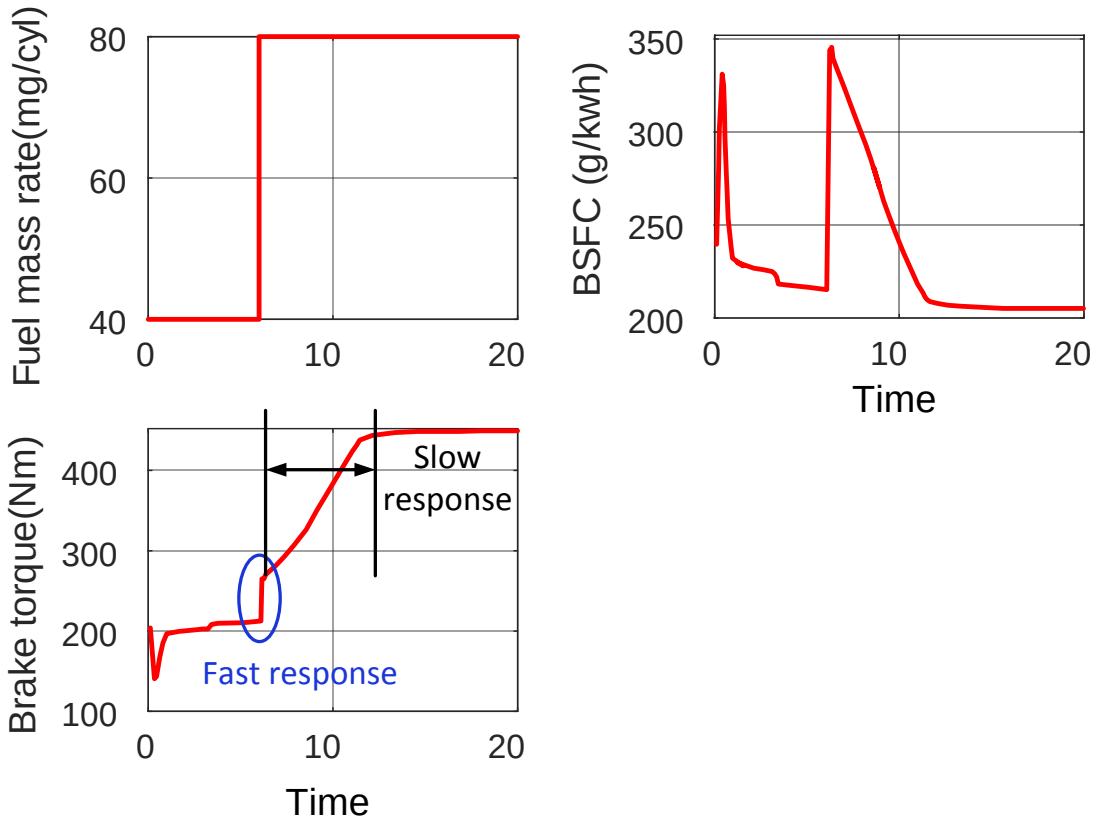

Figure 3.1: Torque and fuel consumption behavior of a turbocharged engine responding to full load input at constant engine speed

In the following sections, details of the proposed approaches are presented. Section II describes the models of major components in hybrid electric vehicle. Section III demonstrates the procedure of energy management algorithm design, mainly focusing on implementation of model predictive control. Section IV shows simulation results of three developed algorithms. A comprehensive analysis is discussed based on differences among the comparative results. Finally, in Section V the paper is summarized

and conclusions are drawn briefly.

3.2 HEV powertrain model

Fig. 3.2 shows the studied hybrid powertrain setup. In this paper a typical parallel hybrid powertrain topology is introduced. A diesel engine is connected to one end of the clutch and an electric motor is connected to the other end. The powers from the engine and motor can be decoupled or coupled by the clutch. The output shaft of motor is connected to the transmission and can drive the vehicle independently. The diesel engine has a turbocharger controlled by a wastegate. In the following subsections, the models of major powertrain components are described.

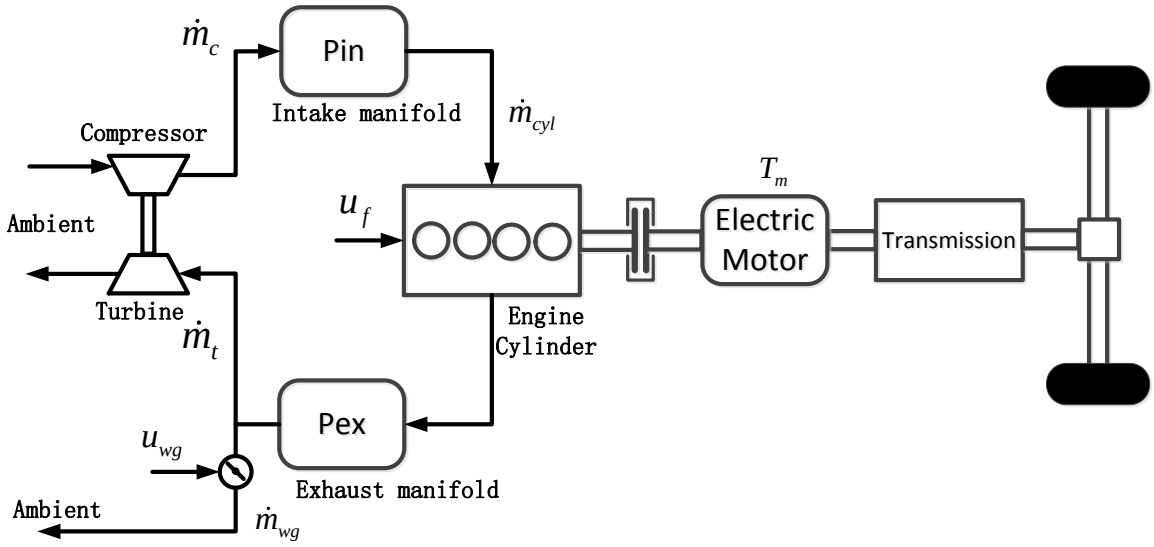

Figure 3.2: A P2 hybrid powertrain architecture with a turbocharged diesel engine

3.2.1 Vehicle model

A longitudinal dynamic model for vehicle is considered and described in Equ.(3.1)–(3.4) [7]. F_d is the traction force on vehicle. The resistance force includes road friction, air drag force and the force due to road slope. g is gravitational constant. u is road friction coefficient. C_{drag} is drag coefficient, ρ_{air} is air density, A_{front} is the effective area of air drag force. R_{tire} is the equivalent tire radius when vehicle is moving. m_{veh} is vehicle mass. m_{tire} is the equivalent mass of rotational components, which are mainly considered as four tires. m_{tire} is calculated by Equ.(3.3).

$$(m_{veh} + m_{tire})\frac{dV}{dt} = F_d - (m_{veh}gu + \frac{1}{2}C_{drag}\rho_{air}V^2A_{front} + m_{veh}g\sin\theta) \tag{3.1}$$

$$F_d = \frac{T_{wheel}}{R_{tire}} \tag{3.2}$$

$$m_{tire} = 4\frac{J_{wheel}}{{R_{tire}}^2} \tag{3.3}$$

$$T_{req} = \frac{T_{wheel}}{i_g i_f}, \quad \omega_{req} = \omega_{wheel} i_g i_f \tag{3.4}$$

Transmission, differential and other drive shafts are simplified as gear ratios and their inertias are all lumped into vehicle inertia. If vehicle speed is predefined, the wheel torque and speed can be calculated and scaled to transmission input shaft by Equ.(3.4). T_{req} and ω_{req} are the requested torque and speed of transmission input shaft that are needed in supervisory controller. i_g is transmission gear ratio and i_f is final drive ratio. Table 3.1 shows the specification of major components in the studied

HEV powertrain.

Table 3.1: Major parameters of the hybrid vehicle powertrain

Engine	1.4 L Turbocharged 200Nm 1800-4000RPM
Electrical Motor	Maxpower: 50kw MaxTorque: 400Nm
Battery	Lithium–ion Battery 6.5 Ah
Transmission	4–speed GearRatio: 2.125,1.25,1,0.72
Final Drive Ratio	3.2
Vehicle	Curb weight 1900kg

3.2.2 Electric motor model

Electric motor uses an efficiency map to describe the relationship among motor torque, motor speed and consumed electrical power . The effects of inertia elements are ignored so that motor torque is assumed to instantly respond to the demand. Equ.(3.5) demonstrates the electric motor model [4].

$$\begin{aligned} P_{ele} &= \frac{P_m}{\eta_m(T_m, \omega_m)} && , T_m > 0 \\ &= P_m \cdot \eta_m(T_m, \omega_m) && , T_m < 0 \end{aligned} \tag{3.5}$$

$$T_{m,\min}(\omega_m) \leq T_m \leq T_{m,\max}(\omega_m) \tag{3.6}$$

P_m is output mechanical power of motor. P_{ele} is input electrical power. η is motor efficiency map with respect to motor torque and speed. Motor torque also has upper and lower bound $T_{m,min}(\omega_m)$ and $T_{m,max}(\omega_m)$, which are functions of motor speed.

3.2.3 Battery model

Battery is simplified to be a resistance circuit illustrated in Fig. 3.3. The circuit current can be derived from circuit principles shown in Equ.(3.8). V_{oc} is open circuit voltage. R_{in} is the resistance of battery. Thus, the dynamics of battery state of charge (SOC) is modeled as shown in Equ.(3.9). Q_{batt} is battery capacity. Open circuit voltage and internal resistance are basically functions of SOC. In this paper, these parameters are obtained from Toyota Prius Battery pack [15].

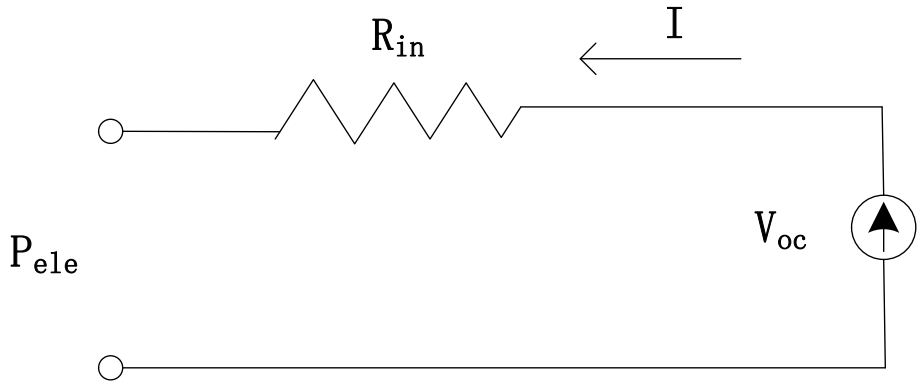

Figure 3.3: A simple equivalent circuit of a battery

The electric power in discharging mode that can be provided by battery should

be limited by Equ.(3.7), which also implies a potential upper bound of motor torque. The minimum value should be selected as the upper bound of motor torque between maximum torques from Equ. (3.6) and (3.7). This paper also assumes that no restriction on battery power is considered when battery is charging.

$$P_{ele} = \frac{T_m \omega_m}{\eta_m^{sign(T_m)}} \leq \frac{V_{oc}^2}{4R_{in}} \tag{3.7}$$

$$I = \frac{V_{oc} - \sqrt{V_{oc}^2 - 4R_{in}P_{ele}}}{2R_{in}} \tag{3.8}$$

$$S\dot{O}C = -\frac{I}{Q_{batt}} \tag{3.9}$$

3.2.4 Engine model

This paper aims to deal with energy management problems regarding engine torque response in transient processes so that an efficiency or BSFC map based engine model is no longer suitable. More detailed information should be included: torque generation related to both fuel injection and air charge; air path loop dynamics associated with turbocharger mechanism, such as intake and exhaust manifold pressures and turbine speed. Some papers have proposed Mean Value Models (MVMs) for this purpose that shows the effectiveness of capturing turbocharger characteristics [16] [17]. Considering the trade-off between model accuracy and complexity, MVMs are adopted and several small simplifications are made. The detailed modeling procedure is discussed in the remaining part of this section.

Basically, the turbocharger dynamics contains three states, intake manifold pressure, exhaust manifold pressure and turbine speed. In paper [18] engine speed is also treated as a state, which is, however, not necessary in this study. Normally, in a parallel HEV, engine output shaft is rigidly connected to the drive line and engine speed is determined by vehicle speed profile and gear ratio. The control inputs of the engine are fuel injection mass and waste gate diameter. The three states and two controls are combined in Equ.(3.10) to form a nonlinear system.

$$\begin{aligned} \frac{dP_{in}}{dt} &= \frac{R_a T_{in}}{V_{in}}(\dot{m}_c - \dot{m}_{cyl}) \\ \frac{dP_{ex}}{dt} &= \frac{R_e T_{ex}}{V_{ex}}(\dot{m}_{cyl} + \dot{m}_f - \dot{m}_t - \dot{m}_{wg}) \\ \frac{d\omega_t}{dt} &= \frac{(W_t - W_c)}{J_t \omega_t} \end{aligned} \tag{3.10}$$

Here, P_{in} , P_{ex} , ω_t are intake manifold pressure, exhaust manifold pressure and turbine speed (rad/s); R_a and R_e are gas constants of ambient air and exhaust gas; V_{in} and V_{ex} are volumes of intake and exhaust manifold; T_{in} , T_{ex} are the temperature in intake and exhaust manifold. $\dot{m}_c$ and $\dot{m}_t$ are the mass flow rate through compressor and turbine. $\dot{m}_{cyl}$, $\dot{m}_f$ are the air and fuel mass flow rate into cylinder. $\dot{m}_{wg}$ is air mass flow rate through waste gate which can be controlled by waste gate valve. W_c and W_t are compressor power and turbine power, which are calculated in Equ. 3.11. Here, c_{pa} and c_{pe} are specific heat capacity at constant pressure of air and exhaust gas; γ_a and γ_e are specific heat capacity ratio of air and exhaust gas; η_c and η_t are

compressor and turbine efficiency.

$$\begin{aligned} W_c &= \frac{\dot{m}_c c_{pa} T_{amb}((P_{in}/P_{amb})^{\frac{\gamma_a - 1}{\gamma_a}} - 1)}{\eta_c} \\ W_t &= \dot{m}_t c_{pe} T_{ex} \eta_t (1 - (P_{amb}/P_{ex})^{\frac{\gamma_e - 1}{\gamma_e}}) \end{aligned} \tag{3.11}$$

Several reasonable assumptions regarding air path loop model should be notified before further discussion.

Assumption:

1. Intake manifold pressure and temperature equal to outlet pressure and temperature of compressor; meanwhile, exhaust manifold pressure and temperature equal to inlet pressure and temperature of turbine
2. Inlet pressure and temperature of compressor equal to ambient pressure and temperature; this rule also applies on outlet pressure and temperature of turbine.
3. Volumetric efficiency in Equ. (3.13) is considered as a constant.
4. Engine torque has fast response as long as fuel injection mass does not exceed its maximum value defined by stoichiometric air fuel ratio [19]. See in Equ. (3.16).

Fuel rate in cylinder is defined in Equ. (3.12)

$$\dot{m}_f = \frac{4 u_f N_e 10^{-6}}{120} \tag{3.12}$$

Air flow rate in cylinder is calculated by Equ. (3.13)

$$\dot{m}_{cyl} = \frac{N_e V_d P_{in} \eta_{vol}}{120 T_{amb} R_a} \tag{3.13}$$

Where N_e is the engine rotational speed, V_d is the displacement of one working cycle, η_{vol} is relative volumetric efficiency.

Wastegate flow rate is considered as a typical orifice model in Equ.(3.14).

$$\dot{m}_{wg} = \frac{P_{ex}}{\sqrt{R_{ex} T_{ex}}} u_{wg} A_{wg} a_{wg} \sqrt{1 - (\frac{P_{amb}}{P_{ex}})^{b_{wg}}} \tag{3.14}$$

Where A_{wg} is the maximum effective area of waste gate orifice. u_{wg} is the waste gate control signal which regulates the effective area. a_{wg} and b_{wg} are the tuning coefficients of orifice model.

Exhaust temperature T_{ex} is simplified as a polynomial function with respect to fuel injection mass and engine speed, which is calibrated by steady–state simulation data from GT–Power.

The mass flow through compressor and turbine, the pressure ratios between the outlet and inlet of compressor and turbine, and turbine shaft speed are major characters in compressor and turbine maps. Some researchers use functions to fit compressor and turbine maps in MVMs to remove discontinuities and implement the functions in optimal control tool box [18]. Here, in this paper we did it in the another way. Original data from those maps are directly used to avoid losing accuracy due to function fitting. The curves and points within the region of the map are all linearly interpolated from the data set points. The original characteristic maps of compressor and turbine are shown in Fig. 3.4 and 3.5.

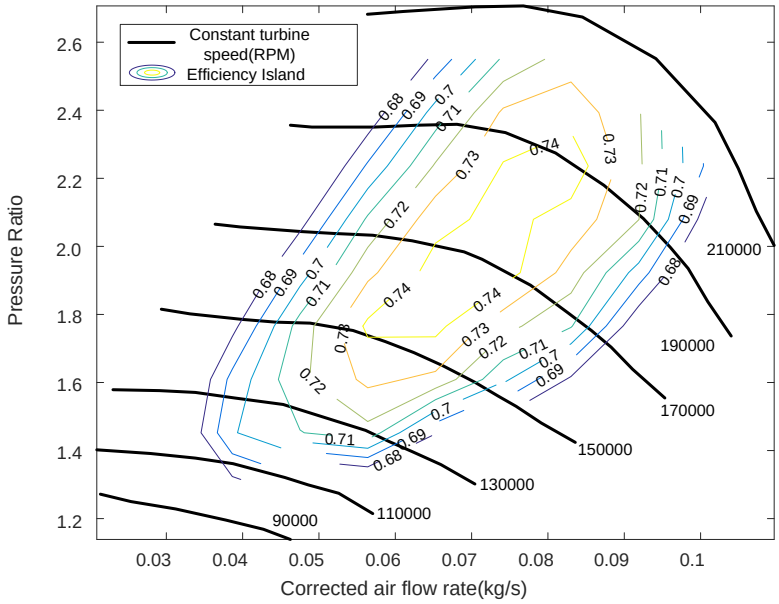

Figure 3.4: Compressor flow and efficiency map

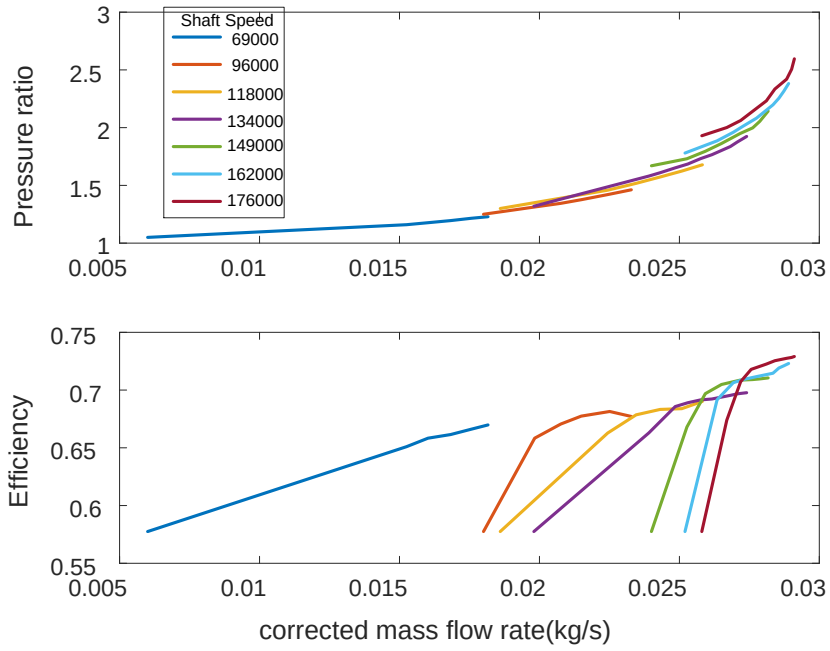

Figure 3.5: Turbine flow and efficiency map

In turbine and compressor maps, mass flow rates are all corrected by inlet pressures and temperatures in Equ.(3.15). In this equation, $\dot{m}_{c,correct}$ and $\dot{m}_{t,correct}$ are corrected mass flows of compressor an turbine. $\dot{m}_{c,act}$ and $\dot{m}_{t,act}$ are actual mass flows; $P_{c,ref}$ and $P_{t,ref}$ are the reference pressures at which the compressor and turbine map are measured; $P_{c,inlet}$ and $P_{t,inlet}$ are the actual inlet pressures of compressor and turbine for correcting mass flows. Therefore, actual mass flow rates of turbine and compressor have to be calculated reversely before inputting to other equations.

$$\begin{aligned} \dot{m}_{c,correct} &= \dot{m}_{c,act}\frac{P_{c,ref}}{P_{c,inlet}}\sqrt{\frac{Tc,inlet}{T_{c,ref}}} \\ \dot{m}_{t,correct} &= \dot{m}_{t,act}\frac{P_{t,ref}}{P_{t,inlet}}\sqrt{\frac{T_{c,inlet}}{T_{t,ref}}} \end{aligned} \tag{3.15}$$

Base on Assumption 4, engine torque is modeled as a stationary map with respect to fuel injection mass and engine speed but fuel injection is saturated by cylinder air charge. Thus, the relationship between engine torque and cylinder air flow is clarified in Equ.(3.17) and (3.18). To be clear, the BSFC map in steady state corresponding with the maximum torque curve is given in Fig. 3.6 to show the engine performance. The maximum torque starting from 1800 RPM is restricted to 200Nm by controlling wastegate flow and intake manifold pressure. For this purpose, the wastegate diameter u_{wg} is limited by an upper bound according to different engine speeds, which is described in Table 3.2.

$$\dot{m}_{f,\max} = \frac{1}{AFR^*}\dot{m}_{cyl} \tag{3.16}$$

$$T_e = f(u_f), u_f \leq u_{f,\max} \tag{3.17}$$

$$u_{f,\max} = \frac{120\dot{m}_{f,\max}}{4N_e 10^{-6}} \tag{3.18}$$

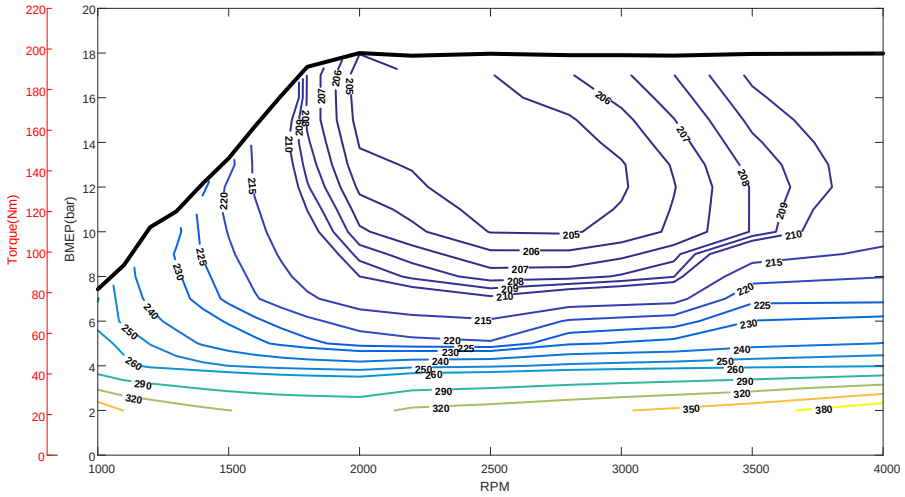

Figure 3.6: BSFC map in steady state with respect to engine speed and load

Table 3.2: Calibrated maximum wastegate diameters with respect to engine speed

Engine RPM	Wastegate Diameter (mm)
1000	0
1400	0
1800	0
2000	5.1887
2200	7.2782
2500	9.3180
2800	11.1503
3000	12.1713
3200	12.9709
3500	13.9679
4000	14.9245

3.3 Model predictive control based supervisory controller design

The objective of HEV energy management is to minimize the fuel consumption during a driving mission with all constraints satisfied. Meanwhile, energy management strategy should be incorporated with a feedback control scheme to compensate the model disturbance and inaccuracy. In this paper, Model predictive control based architecture is utilized and shown in Fig. 3.7. The MPC based supervisory controller (MPCSC) predicts future trajectories of system states based on measurements at first

step and control sequences in each prediction horizon. The best control sequence can be found by minimizing the cost function, which is also the goal of HEV energy management, subject to all the constraints. Afterwards, the MPCSC implements the first step of the optimal control sequence and makes the prediction horizon move one step forward. This process is repeated until the end of driving mission.

To be noted, MPCSC is only activated when engine and motor torque are coupled and positive vehicle power is required. In other words, engine and motor are controlled independently when clutch is disengaged. For example, at the stages of vehicle start and engine idles, the motor provides all the requested power for driving vehicle; during gear shifting, clutch is off, and engine torque is reduced to a constant and the motor gives zero torque.

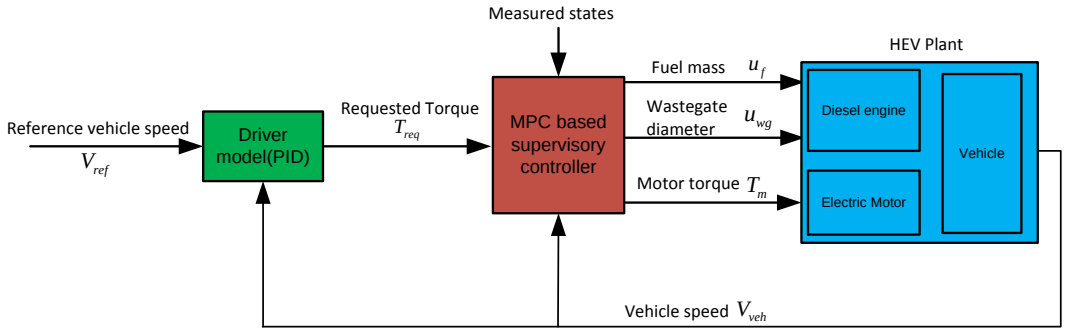

Figure 3.7: Control architecture of the proposed HEV powertrain

3.3.1 Problem Formation

When engine and motor are coupled, the studied system are formulated with four states $\boldsymbol{x}$, intake pressure, exhaust pressure, turbine speed and SOC; three controls $\boldsymbol{u}$, fuel injection mass, waste gate diameter and motor torque; and three exogenous

inputs $\boldsymbol{v}$ engine speed, requested torque and gear ratio. The gear shift strategy is predefined according to engine speed so that gear ratio is also an known parameter. The system dynamic equation is written in state-space form $\dot{\boldsymbol{x}} = F(\boldsymbol{x}, \boldsymbol{u}, \boldsymbol{v})$.

The cost function in kth prediction horizon is defined as total equivalent consumption in Equ. 3.19. It consists of engine fuel consumption as the first term of right hand side, and equivalent fuel due to battery energy cost as the second term. Coefficient μ is the equivalent ratio between fuel energy and electrical energy.

$$J(k) = \sum_{i=0}^{P} \dot{m}_f(t_k + i)\Delta t + \mu(SOC(t_k + P) - SOC(t_k)) \tag{3.19}$$

The constrain functions includes:

1. System dynamic equations in (3.9)(3.10)
2. Path constraints

$$T_e(u_f, \omega_e) + T_m = T_{req} \tag{3.20}$$

$$u_f \leq u_{f,\max}(P_{in}) \tag{3.21}$$

3. Boundaries of state and control variables

$$SOC_{\min} \leq SOC \leq SOC_{\max} \tag{3.22}$$

$$P_{in,\min} \leq P_{in} \leq P_{in,\max} \tag{3.23}$$

$$P_{ex,\min} \leq P_{ex} \leq P_{ex,\max} \tag{3.24}$$

$$N_{t,\min} \leq N_t \leq N_{t,\max} \tag{3.25}$$

$$u_{f,\min} \leq u_f \leq u_{f,\max} \tag{3.26}$$

$$u_{wg,\min} \leq u_{wg} \leq u_{wg,\max} \tag{3.27}$$

$$T_{m,\min} \leq T_m \leq T_{m,\max} \tag{3.28}$$

3.3.2 MPC algorithm implementation

To implement MPC algorithm the future vehicle speed reference is required. In this paper, we assume that this information can be obtained from a given driving cycle. Besides, the requested torque that makes vehicle track the reference speed can be predicted from vehicle model. Specifically, in the first step of each prediction horizon, total requested torque inherits the output from driver model (a PID controller). Then the actual vehicle speed is assumed to catch up reference speed within the first step. Starting from the second step, the requested torque is predicted by the Equ.(3.29)

which is derived from Equ.(3.1)-(3.4).

$$T_{req} = \frac{R_{tire}}{i_g i_f}[(m_{veh} + m_{tire})\frac{dV_{ref}}{dt} + (m_{veh}gu + \frac{1}{2}C_{drag}\rho_{air}V_{ref}^2 A_{front} + m_{veh}g\sin\theta)] \tag{3.29}$$

Fig. 3.8 shows the steps of solving dynamic optimization problem in one prediction horizon. The iteration number i counts from 0 to P indicating the prediction steps. At each step control variables are meshed within their permissible boundaries that satisfies all constraints based on the states at first step. The system dynamics are calculated exhaustively in the prediction horizon under a certain resolution to generate multiple possible state trajectories. Finally, the values of cost function are compared to find the optimal solution to the current problem. The proposed method is processed numerically all the way without having to ensure the differentiability of mathematical expressions in analytical models. This update-predict-implement scheme repeats and continues until completing the driving cycle. In order to maintain the final SOC in a reasonable range, or usually called charge sustaining, the simulation needs to be conducted multiple times by tuning the equivalent ratio μ.

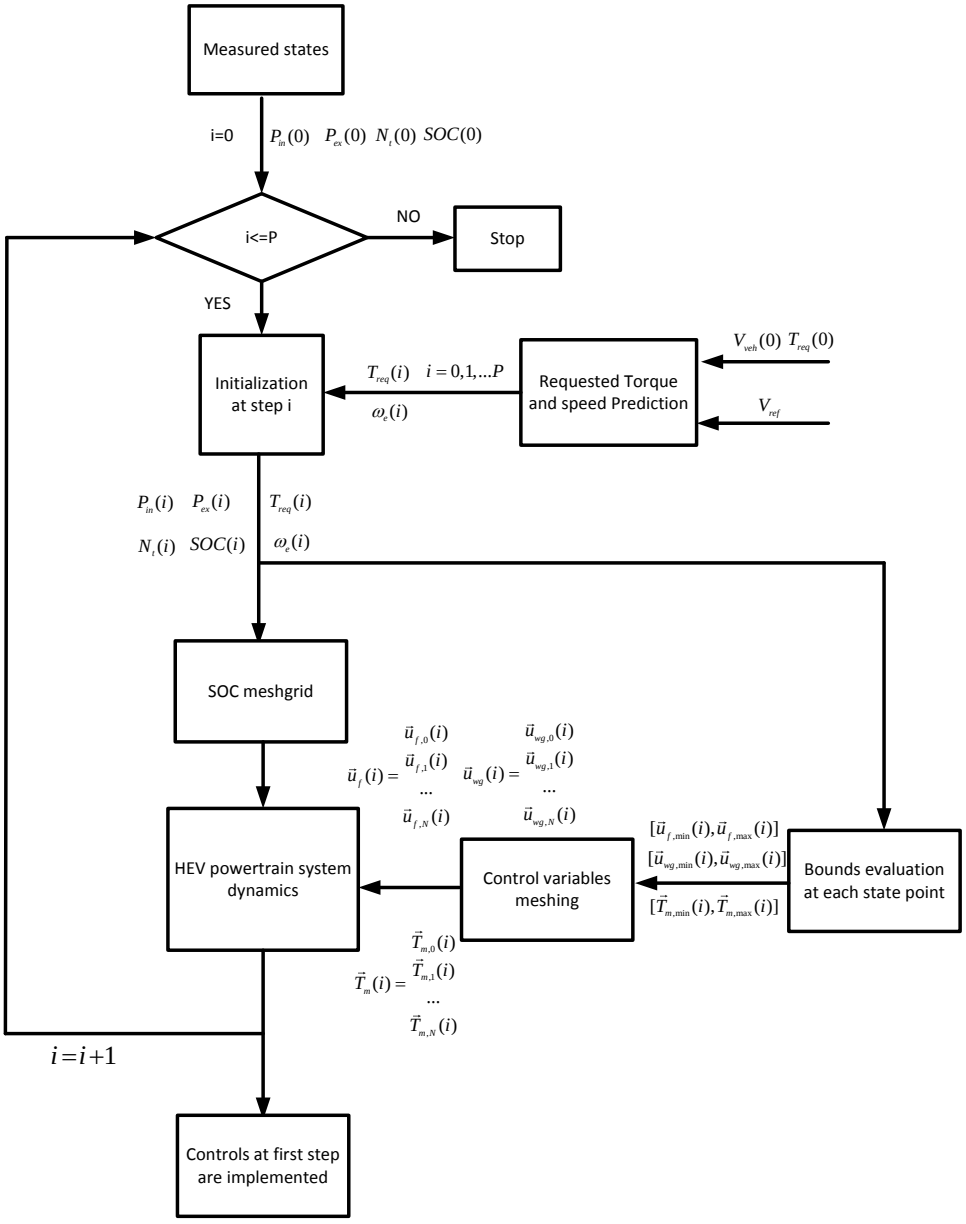

Figure 3.8: The flow chart of MPCSC implementation in a prediction horizon

3.4 Simulation results and discussion

To demonstrate the effectiveness of the proposed controller, three strategies are developed in the same HEV powertrain model and compared. They are MPC-based supervisory control with engine air path dynamic model, optimal supervisory control with a map-based engine model and rule-based supervisory control [20] [21]. Three methods share the same engine start-stop and gear shift strategies in UDDS cycle. For convenience, all three controllers are noted as MPCSC, MBSC and RBSC respectively in further discussions.

In Fig. 3.9, the actual and reference vehicle speed curves are compared in all three strategies demonstrating that the tracking demand are well satisfied. Fig. 3.10 shows the engine On/Off and gear shift status are also identical in three different methods.

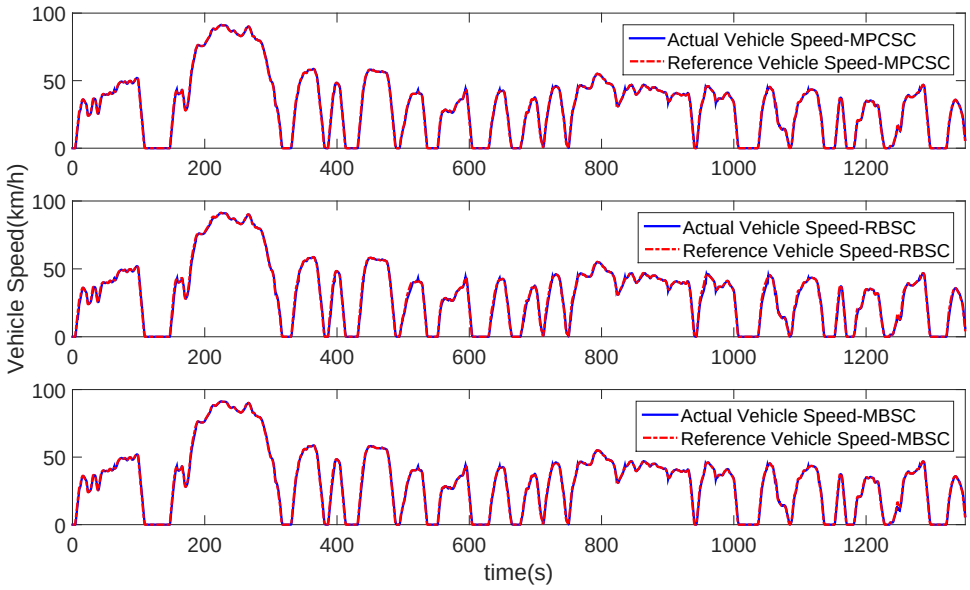

Figure 3.9: Vehicle speed tracking performance of three strategies

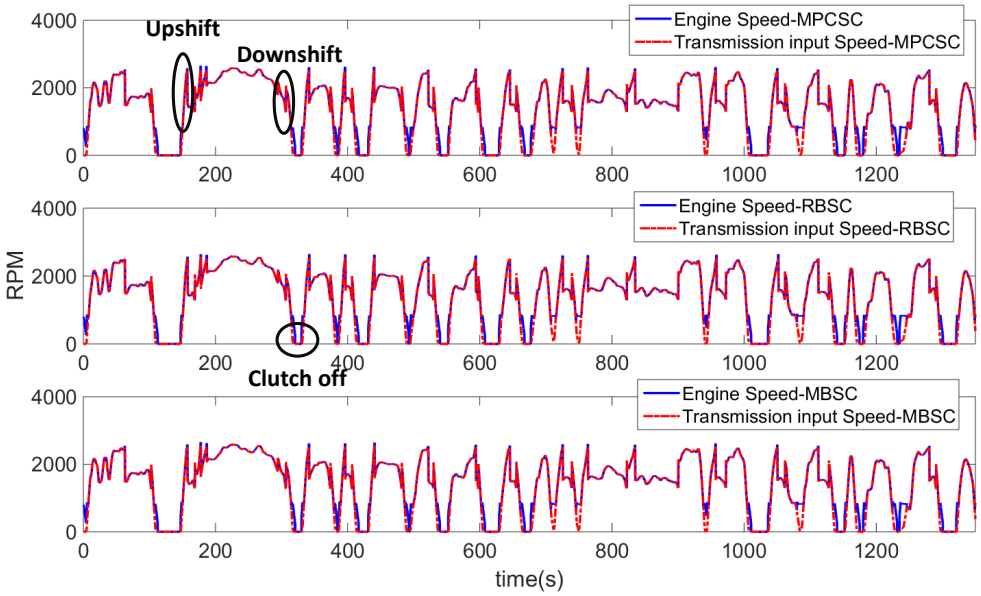

Figure 3.10: Comparison of engine speed and transmission input speed for three strategies

Fig. 3.11 plots demand engine torque generated from three controllers and the corresponding actual torque calculated from plant model. MPCSC has the best engine torque estimation among three as a result of the predictive engine model with air path dynamics. In some time slots such as 100s∼200s and 400s∼450s, MBSC has relatively large error between demanded torque and actual torque. However, in most of time MBSC has quite similar torque curves as in MPCSC where the error between desired and actual torque is little. That means the advantage of MPCSC may not always take effect but depends on the engine torque demand. For example, during cruising the total power demand to maintain the vehicle speed is small as seen in Fig. 3.13 from 0s to 100s, whereas during rapid acceleration process(150s∼200s) the total power demand is much larger. The quantity of total power demand also influences the

torque split strategies in MPCSC and MBSC and therefore engine torque demand. Actually, the predictive engine model mentioned in section III mainly estimates the upper bound of engine torque. When the demanded engine torque does not exceed this bound, the actual torque can reach to the demand by giving correct fuel injection signals. Otherwise, the additional injection that aims to generate more torque turns out to be a waste of fuel. It can be obviously seen in Fig. 3.12 the black line is higher than blue line during 150s∼200s. Moreover, RBSC is the worst case at this point because its intuitive solution of torque split makes engine torque demand go beyond its limit more frequently.

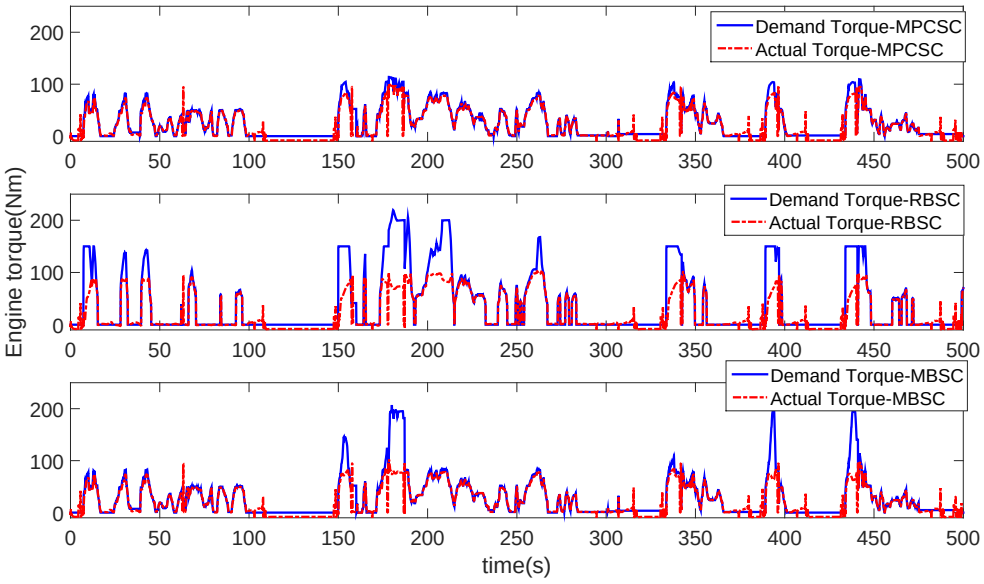

Figure 3.11: Engine demand torque and actual torque comparison in three strategies

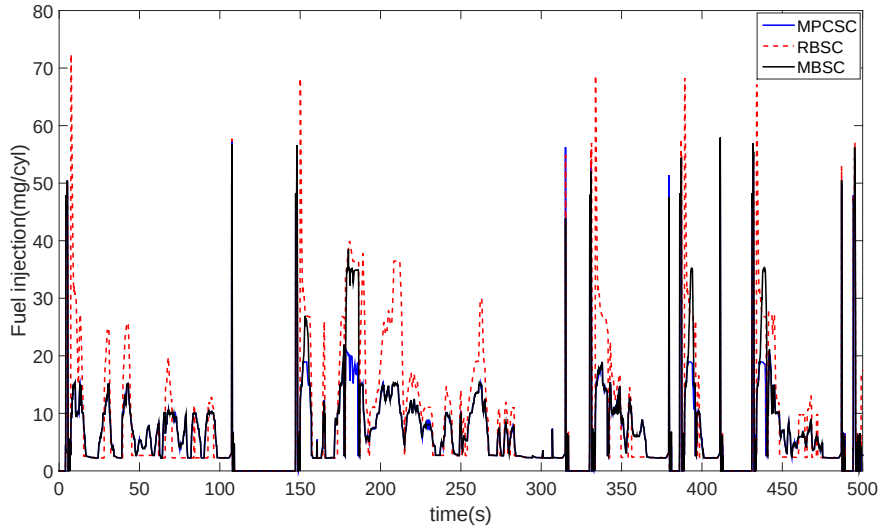

Figure 3.12: Comparison of fuel injection mass per cycle for three strategies

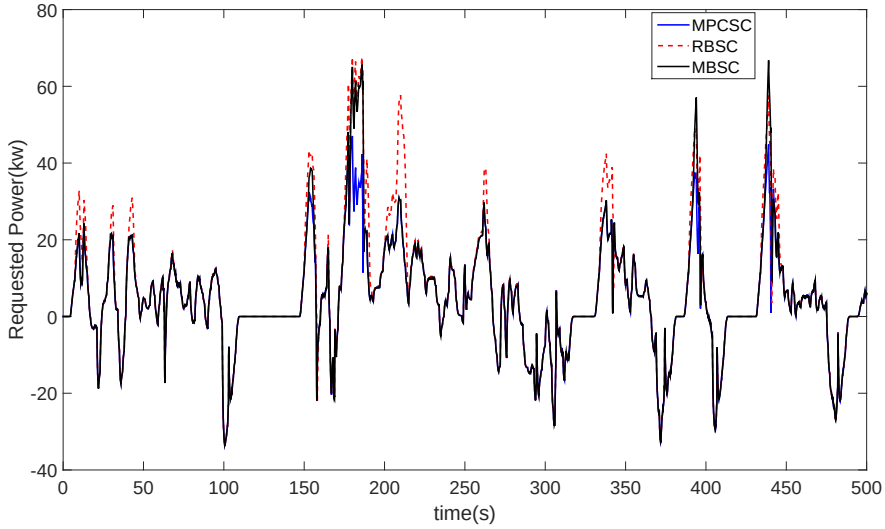

Figure 3.13: Comparison of total requested power from driver demand for the three strategies

Fig. 3.13 shows that in 150s∼200s total requested power in MPCSC is lower

than MBSC which is another advantage of MPCSC. As mentioned above, MPCSC is able to avoid overestimating engine maximum permissible torque and deriving an unreachable torque command so that the total power requirement in MPCSC can be fulfilled by actual engine torque and motor torque. Thus, total power requirement from driver model (PID controller) does not necessarily increase to compensate the gap between desired and actual vehicle acceleration performance. In contrast, total power requirement inflates in MBSC and RBSC due to the inaccuracy of the engine model. Besides, the amount of power increase depends on the error of engine torque prediction. In Fig. 3.14 the actual motor torques for three strategies are shown. During 150s∼200s MPCSC tries to regulate motor torque cooperatively to help satisfy the total power requirement.

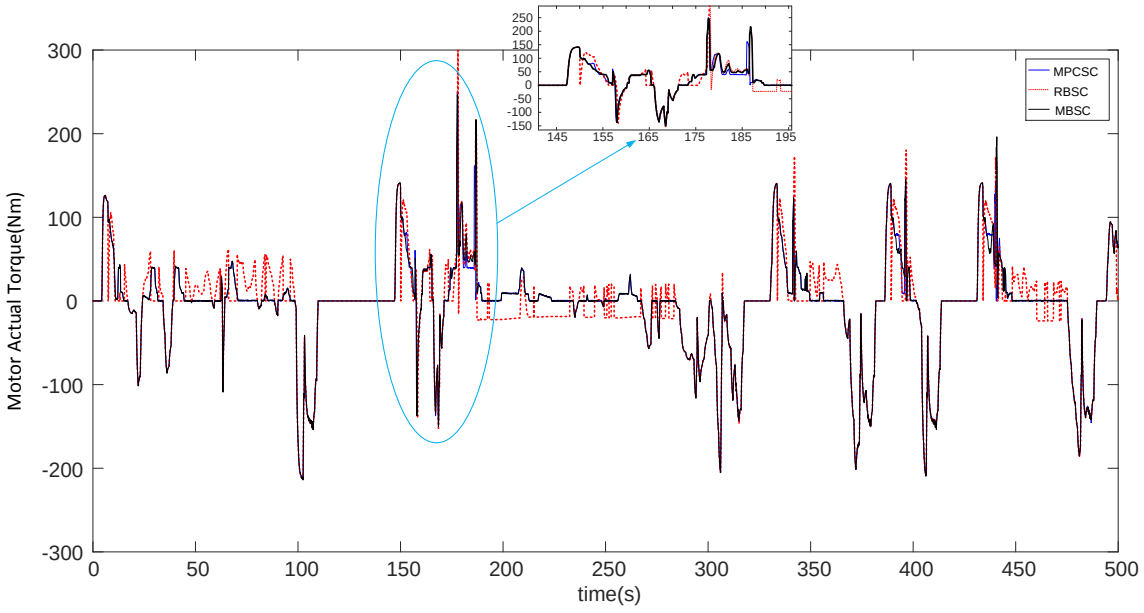

Figure 3.14: Comparison of electric motor torque for the three strategies

Fig. 3.15 and Fig. 3.16 plot the SOC trajectories and accumulate fuel consumptions in the whole cycle. In order to compare fuel consumptions of three methods, the SOCs at the beginning of driving cycle are all set to 0.6 and are tuned to be sufficiently close at the end (2% difference). Fig. 3.16 indicates that fuel consumption of MPCSC is the lowest one even it has more charge in the battery than the other two. This fuel economy improvement reveals the benefits from a transient engine model used in prediction and proper optimal torque split strategy incorporating with this model. Fuel consumption difference between MPCSC and MBSC verifies the strong potential of transient engine model, especially in rapid acceleration where total power requirement is high. It is also not exaggerate to expect that the benefits will be more significant if more rapid speed changing occurs in driving cycle.

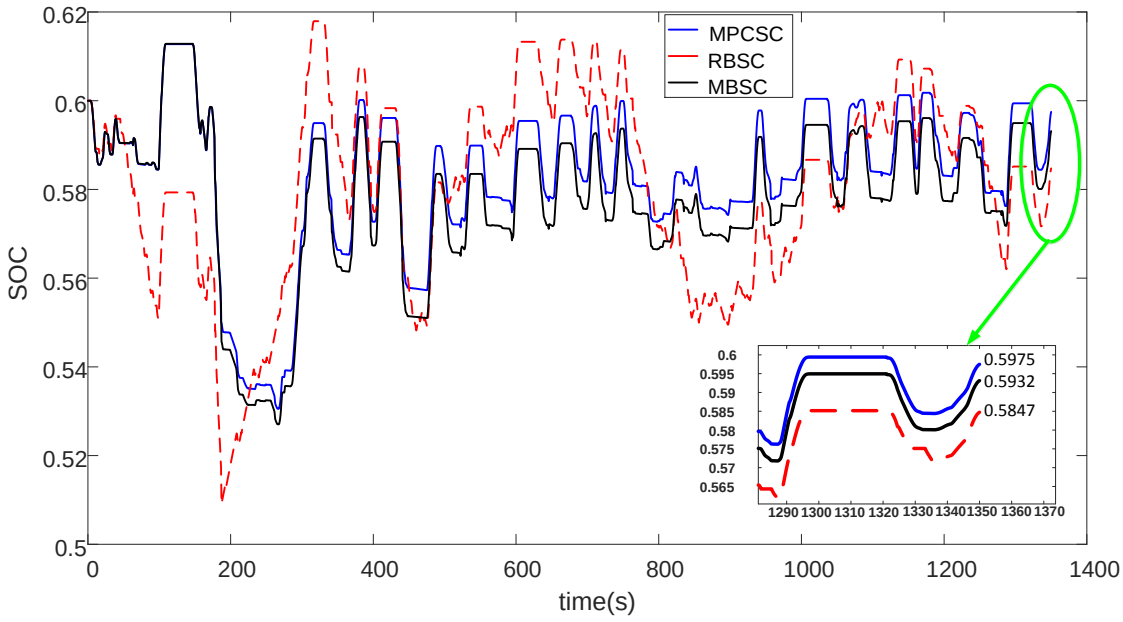

Figure 3.15: Comparison of SOC trajectory for three strategies

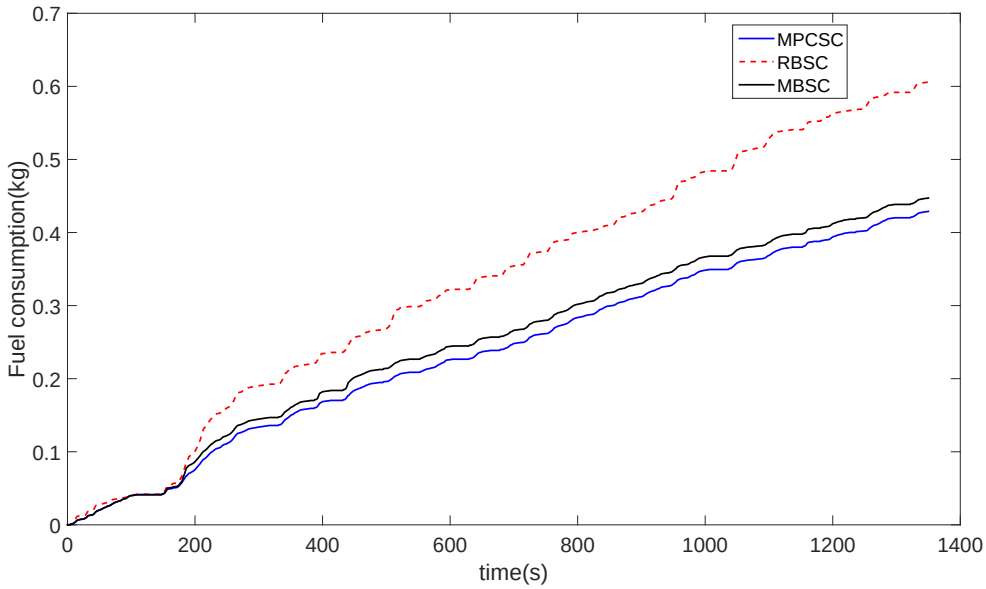

Figure 3.16: Comparison of total fuel consumption for three strategies

3.5 Conclusions

A hybrid powertrain system with a turbocharged diesel engine is studied in this paper. A fairly calibrated engine transient model is built in order to simulate air path dynamics and engine torque response during the altering of operating condition. Then model predictive control based strategy considering the transient model is developed for solving energy management problem and reducing fuel consumption. Three different strategies, namely rule-based strategy without explicit optimization, instantaneous optimal control using map-based engine model and MPC based optimal strategy considering transient engine model, are compared by implementing them in UDDS cycle with the same engine on/off and gear shift strategies. Results shows the third method has the best fuel economy without compromising vehicle performance.

A considerable fuel (about 6%) of this strategy is saved by comparing it to the second one. Even almost 30% fuel consumption is reduced from the first method. Clearly, the properly designed optimal control strategy and transient engine model contributes to this improvement.

Reference

[1] Ali Emadi, Kaushik Rajashekara, Sheldon S Williamson, and Srdjan M Lukic. Topological overview of hybrid electric and fuel cell vehicular power system architectures and configurations. *IEEE Transactions on Vehicular Technology*, 54(3):763–770, 2005.

[2] Yinye Yang, Kamran Arshad-Ali, Joel Roeleveld, and Ali Emadi. State-of-the-art electrified powertrains-hybrid, plug-in, and electric vehicles. *International Journal of Powertrains*, 5(1):1–29, 2016.

[3] Pierluigi Pisu and Giorgio Rizzoni. A comparative study of supervisory control strategies for hybrid electric vehicles. *IEEE Transactions on Control Systems Technology*, 15(3):506–518, 2007.

[4] Jinming Liu and Huei Peng. Modeling and control of a power-split hybrid vehicle. *IEEE transactions on control systems technology*, 16(6):1242–1251, 2008.

[5] Namwook Kim and Aymeric Rousseau. Sufficient conditions of optimal control based on pontryagins minimum principle for use in hybrid electric vehicles. *Proceedings of the Institution of Mechanical Engineers, Part D: Journal of Automobile Engineering*, 226(9):1160–1170, 2012.

[6] Cristian Musardo, Giorgio Rizzoni, Yann Guezennec, and Benedetto Staccia. A-ecms: An adaptive algorithm for hybrid electric vehicle energy management. *European Journal of Control*, 11(4-5):509–524, 2005.

[7] Gino Paganelli, Sebastien Delprat, Thierry-Marie Guerra, Janette Rimaux, and Jean-Jacques Santin. Equivalent consumption minimization strategy for parallel hybrid powertrains. In *Vehicular Technology Conference, 2002. VTC Spring 2002. IEEE 55th*, volume 4, pages 2076–2081. IEEE, 2002.

[8] Lorenzo Serrao, Simona Onori, and Giorgio Rizzoni. A comparative analysis of energy management strategies for hybrid electric vehicles. *Journal of Dynamic Systems, Measurement, and Control*, 133(3):031012, 2011.

[9] Zou Yuan, Liu Teng, Sun Fengchun, and Huei Peng. Comparative study of dynamic programming and pontryagins minimum principle on energy management for a parallel hybrid electric vehicle. *Energies*, 6(4):2305–2318, 2013.

[10] Hoseinali Borhan, Ardalan Vahidi, Anthony M Phillips, Ming L Kuang, Ilya V Kolmanovsky, and Stefano Di Cairano. Mpc-based energy management of a power-split hybrid electric vehicle. *IEEE Transactions on Control Systems Technology*, 20(3):593–603, 2012.

[11] Saida Kermani, Sebastien Delprat, Thierry-Marie Guerra, Rochdi Trigui, and Bruno Jeanneret. Predictive energy management for hybrid vehicle. *Control Engineering Practice*, 20(4):408–420, 2012.

[12] Chao Sun, Xiaosong Hu, Scott J Moura, and Fengchun Sun. Velocity predictors for predictive energy management in hybrid electric vehicles. *IEEE Transactions on Control Systems Technology*, 23(3):1197–1204, 2015.

[13] Dennis N Assanis, Zoran S Filipi, Scott B Fiveland, and Michalis Syrimis. A predictive ignition delay correlation under steady-state and transient operation of a direct injection diesel engine. *Journal of Engineering for Gas Turbines and Power*, 125(2):450–457, 2003.

[14] Nils Lindenkamp, Claude-Pascal Stöber-Schmidt, and Peter Eilts. Strategies for reducing no x-and particulate matter emissions in diesel hybrid electric vehicles. Technical report, SAE Technical Paper, 2009.

[15] Namwook Kim, Sukwon Cha, and Huei Peng. Optimal control of hybrid electric vehicles based on pontryagin's minimum principle. *IEEE Transactions on Control Systems Technology*, 19(5):1279–1287, 2011.

[16] Lars Eriksson. Modeling and control of turbocharged si and di engines. *Oil & Gas Science and Technology-Revue de l'IFP*, 62(4):523–538, 2007.

[17] R Sharma, D Nesic, and C Manzie. Control oriented modeling of turbocharged (tc) spark ignition (si) engine. Technical Report 2009-01-0684, SAE Technical Paper, 2009.

[18] Martin Sivertsson and Lars Eriksson. Optimal transient control trajectories in diesel–electric systemspart i: Modeling, problem formulation, and engine properties. *Journal of Engineering for Gas Turbines and Power*, 137(2):021601, 2015.

[19] Alois Danninger, Markus Bachinger, Michael Stolz, and Martin Horn. Online calculation of diesel engine torque dynamics. In *Control Applications (CCA), 2014 IEEE Conference on*, pages 669–674. IEEE, 2014.

[20] Bernd M Baumann, Gregory Washington, Bradley C Glenn, and Giorgio Rizzoni. Mechatronic design and control of hybrid electric vehicles. *IEEE/ASME Transactions On Mechatronics*, 5(1):58–72, 2000.

[21] Chan-Chiao Lin, Huei Peng, Jessy W Grizzle, and Jun-Mo Kang. Power management strategy for a parallel hybrid electric truck. *IEEE transactions on control systems technology*, 11(6):839–849, 2003.

Symbol II

PID are defined in the Symbol I as coefficients that directly multiplies the speed error, and the integral, derivative of speed error. The calculated products should multiply vehicle mass before they are used in the simulation.

a_{wg}	coefficients of wastegate model	0.6857
b_{wg}	coefficients of wastegate model	3.5811
c_{pa}	specific heat capacity of air,constant pressure	1007 J/(kg-K)
c_{pe}	specific heat capacity of exhaust gas,constant pressure	1250 J/(kg-K)
g	gravitational acceleration	9.8 m/s^2
i_g	transmission gear ratio	
i_f	final drive ratio	3.2
$\dot{m}_f$	fuel flow rate	
m_{veh}	vehicle mass	1900 kg
$\dot{m}_{c,correct}$	corrected mass flows of compressor	
$\dot{m}_{t,correct}$	corrected mass flows of turbine	
$\dot{m}_c$	mass flow rate through compressor in map	
$\dot{m}_t$	mass flow rate through turbine in map	
$\dot{m}_{c,act}$	actual mass flows of compressor	
$\dot{m}_{t,act}$	actual mass flow of turbine	
$\dot{m}_{cyl}$	cylinder air flow rate	
$\dot{m}_{wg}$	air mass flow rate through wastegate	
u	road friction coefficient	0.015
u_f	fuel injection mass	
$u_{f,\min}$	minimum fuel injection mass	0 mg/cycle

$u_{f,\max}$	maximum fuel injection mass	60 mg/cycle
u_{wg}	wastegate diameter	
$u_{wg,\min}$	minimum wastegate diameter	0 mm
$u_{wg,\max}$	maximum wastegate diameter	
A_{wg}	maximum effective area of wastegate orifice	706.85 mm^2
A_{front}	effective area of air drag force	2 m^2
AFR^*	stoichiometric air fuel ratio	15
C_{drag}	drag coefficient	0.32
F_d	traction force	
J_{wheel}	single wheel inertia	1.25 kg-m^2
J_t	turbocharger inertia	7e-5 kg-m^2
N_e	engine speed RPM	
N_t	turbine speed RPM	
P_m	output mechanical power of motor	
P_{ele}	input electrical power of motor	
P_{in}	intake manifold pressure	
P_{ex}	exhaust manifold pressure	
$P_{c,ref}$	reference pressure for compressor	96 kpa
$P_{t,ref}$	reference pressure for turbine	101 kpa
$P_{c,inlet}$	actual inlet pressure of compressor	
$P_{t,inlet}$	actual inlet pressure of turbine	
Q_{batt}	capacity of battery	6.5 A-h
R_{tire}	tire radius	0.3 m
R_a	gas constants of ambient air	287 J/kg-K

R_e	gas constants of exhaust gas	287 J/kg-K
SOC	battery state of charge	
SOC_{ini}	initial battery state of charge	0.6
T_{in}	intake manifold temperature	
T_{ex}	exhaust manifold temperature	
$T_{c,ref}$	reference temperature for compressor	302 K
$T_{t,ref}$	reference temperature for turbine	873 K
T_{req}	total requested torque	
T_e	engine output torque	
T_m	motor output torque	
$T_{m,max}$	motor maximum torque limit	
$T_{m,min}$	motor minimum torque limit	
V	vehicle speed	
V_{oc}	open circuit voltage	
V_d	displacement of one working cycle	0.0014 m^3
V_{in}	volume of intake manifold	0.005 m^3
V_{ex}	volume of exhaust manifold	0.0008 m^3
W_t	the gas power to drive turbine	
W_c	the consumed power on compressor	
η	motor efficiency	
η_c	compressor efficiency	
η_t	turbine efficiency	
η_{vol}	relative volumetric efficiency	0.98
γ_a	specific heat capacity ratio of air	1.4

γ_e	specific heat capacity ratio of exhaust gas	1.289
μ	penalty of SOC change in cost function	2806 g/h
ρ_{air}	air density	1.225 kg/m^3
ω_t	turbine speed rad/s	
ω_{req}	requested speed rad/s	
PID	PID controller parameters in driver model	P=1,I=0.1,D=0

Chapter 4

ACLMPC-based HEV energy management

This chapter includes the following **submitted** paper:

Yi Huo, Fengjun Yan, Chuan Hu, Yanjun Huang, "An Adaptive Learning Model Predictive Control based Energy Management Design for Hybrid Powertrain with a Turbocharged Diesel Engine." submitted to Energy, Elsevier in April 2018.

Huo, Yi and Fengjun Yan are with the Department of Mechanical Engineering, McMaster University, Hamilton, ON L8S 4L8, Canada.

Chuan Hu is with the Department of Systems Design Engineering, University of Waterloo, 200 University Ave W, Waterloo, ON N2L 3G1, Canada.

Yanjun Huang is with Department of Mechanical and Mechatronics, University of Waterloo, 200 University Ave W, Waterloo, ON N2L 3G1, Canada.

Co-authorship declaration: The idea of regulating control horizon in MPC was first prompted in a discussion between me and Prof. Yan. Then, I gradually

came up with the idea of using another cost function to evaluate the performance of MPC. I had completed the strategy design and simulation by myself. Prof. Yan gave me valuable comments on effectively demonstrating the idea in the paper. Dr. Hu and Dr. Huang helped me revised the paper and gave suggestions about submitting the paper.

Abstract

As an essential problem for a hybrid electric vehicle (HEV), the powertrain energy management has been studied extensively to reduce HEV fuel consumption. Model predictive control (MPC) has been proved to be a promising solution for this problem by formulating its performance index as the powertrain energy cost. The control horizon selection in MPC is crucial for its performance. Most of previous research work that adopts MPC in HEV energy management problems, obtains the control action by solving an optimal control problem in multi–step prediction horizon and applying the first element of the derived control sequence. In fact, the large implemented control step may lead to poorer control performance, because of the error accumulation. However, it can also reduce the total computational load of MPC since the number of prediction stage is decreased. To balance the needs of two issues, this paper proposed a novel learning mechanism to adaptively select control horizon according to its previous performance. The proposed mechanism was utilized for a turbocharged–engine–incorporated HEV powertrain, considering engine transients. With an automatic control–step regulator, the proposed method demonstrated a similar performance with the best constant control step, and meanwhile largely reduced the computational load. To test the robustness of the proposed method, a mean–squared deviation was introduced to show the control performance changes associated

with driving–cycle variants. The effectiveness of the proposed control strategy was verified through simulations in a GT–SUITE/Simulink platform.

Kewwords: Hybrid electric vehicle, energy management, model predictive control, control step learning, turbocharger, optimal control

4.1 Introduction

Hybrid electric vehicles (HEVs) comprise two energy sources in their powertrain systems, which are internal combustion engine (ICEs) and electric motors (EMs). Comparing to conventional vehicles where engines are the only power source, HEVs provide a new degree of freedom for delivering requested power, that is, the total power for driving the vehicle can be realized by either one of the power sources or their combination [1] [2]. Therefore, the problem of properly distributing the power demands for ICE and EMs is significant in HEV powertrain control. It is referred as energy management strategy (EMS) or supervisory control (SC), which has been studied extensively over the past two decades [3–9].

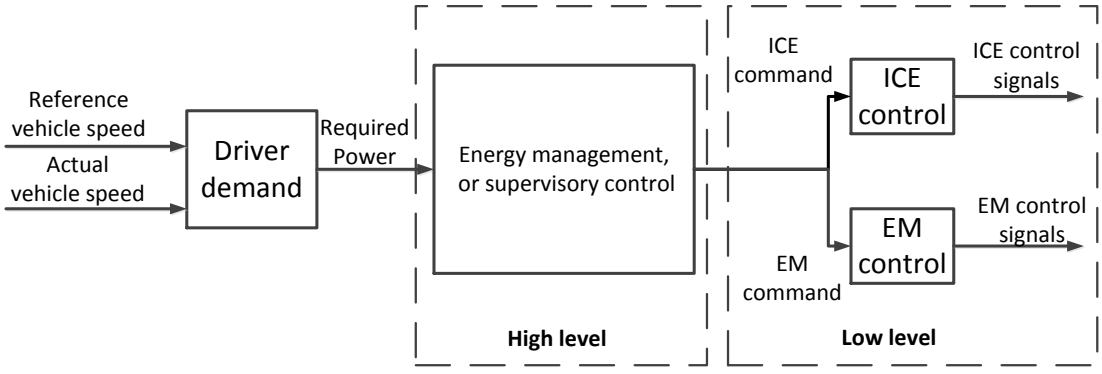

Figure 4.1: A HEV powertrain control structure.

Fig. 4.1 depicts a classic two-level control scheme for HEVs. The low-level controller aims to fulfill drivers demand for speed tracking. The torque or speed commands of ICE and EM generated from the high-level controller are fed into the low level as references. The low-level control law is designed to make the actual torque or speed converge to their references [11]. To solve this problem, some work [12–15] involves various techniques of disturbance rejection in consideration of stability and robustness. The high-level controller deals with the energy management problem. It receives information from ICE and EM characteristics, driving cycle and actual vehicle speed, and derives setpoints for ICE and EMs in a way that the fuel consumption in the whole driving cycle is minimized and the vehicle speed profile is fairly tracked concurrently. Some solutions for energy management problems are mainly based on optimal control theories and can be classified into dynamic programing (DP), equivalent consumption management strategy (ECMS) and Pontryagin minimization principle (PMP) [16–19].

Model predictive control (MPC) has established itself as a promising solution for multi-input-multi-output (MIMO) system control problems. Its application in HEV energy management problems can be found in [10, 21–23]. In conventional HEV EMSs, ICE is normally modeled by an efficiency map with regard to the torque and speed. It implies that the transient characteristics of the engine are not involved in the high-level controller and the generated optimal setpoints is based on quasi–steady–state assumption. Then, the transient behavior at the current time can influence the decision of EMS in the future because the engine operating point might not be realized on time as expected. Our previous work [20] has addressed this issue for a HEV powertrain with a turbocharged diesel engine. A detailed engine model including

the air path dynamics was incorporated into an online HEV energy management strategy, and a model predictive control (MPC) structure was adopted to solve it. Some comparative results have shown that the proposed method considerably reduces fuel consumption.

In MPC implementations, some parameters, such as the prediction and control horizons, weights on outputs and inputs, etc., need to be properly determined to obtain the desired control performance. A few heuristic off–line tuning methods have been provided for dynamic matrix control (DMC) based on the approximation or simulation of the system delay time, either by giving explicit formulas for various parameters [24,25] or their bounds [26]. A comprehensive review about MPC controller tuning strategies can be found in [27]. Some more recent work proposed automatic tuning strategies, in which parameters are updated along with the optimization algorithm instead of human experience [28–31]. For example, paper [29] combined a genetic algorithm with fuzzy decision–making to automate the process of trail–and–error, and determine the parameters that best matched the desired results. In [30], Ashraf et al. proposed an on–line parameter tuning method for linear MPC, by obtaining analytical expressions for the sensitivity of the closed–loop MPC response with respect to input and output weight. Those strategies facilitate the use of MPC controller by avoiding tedious procedures of manually regulating coefficients. Though some heuristic or optimization approaches have been presented to select the step of prediction and control horizon [27], the on–line self–tuning algorithm of those is not a widely reported topic in the literature.

The prediction and control step are directly related to the stability and robustness of MPC. Moreover, they can also significantly influence the computational load of

implementing MPC, especially for the nonlinear, MIMO problems which are normally solved by complex mathematical programming approaches [34]. For one thing, a larger prediction step leads to better system stability but increases the time of each prediction and the whole process. For another, implementing more control steps can decrease the occurrence of prediction to complete the process and the total computing time, however, at a risk of compromising the stability. Therefore, for a finite receding process as in MPC, if the predictive model is accurate enough in some portion of the process, the control step can be set large, but no larger than the prediction step, to reduce the total computing time; meanwhile, if the model error and disturbance is large in some portion, the control step should be reduced to avoid stability problems.

Motivated by aforementioned discussions, this paper proposes an adaptive control–step learning MPC (ACLMPC) to make a trade–off between the concerns of the MPC stability and computational load. The prediction step is still determined in an intuitive manner according to the simulation results. The major contribution lies on the adaptive selection of the control step by considering both the control performance and computational cost. The principle of ACLMPC is that, a "Confidence" function was employed to evaluate the dependability of predicted control inputs based on previous control performance before entering into the next prediction stage. Then, another cost function minimized a cost combining weighted computing time and "Confidence" to find the best control step for future actions. The proposed controller was applied to solve the energy management problem in a HEV powertrain with a turbocharged diesel engine.

This paper is organized as follows: Section II briefly introduces models of the

studied HEV powertrain; Section III formulates the nonlinear model predictive control problem without considering the control step regulation; Section IV presents the details of ACLMPC method; Section V shows GT–Suite–Simulink co–simulation results for ACLMPC and discusses its major advantages; Section VI demonstrates the adaptability of the proposed method to the variation of driving cycle; Section VII draws conclusions.

4.2 HEV modeling

Fig. 4.2 shows a parallel hybrid powertrain topology with an electric motor being placed between a clutch and a transmission. A turbocharged diesel engine is involved as another power source. The turbocharger is waste–gate controlled.

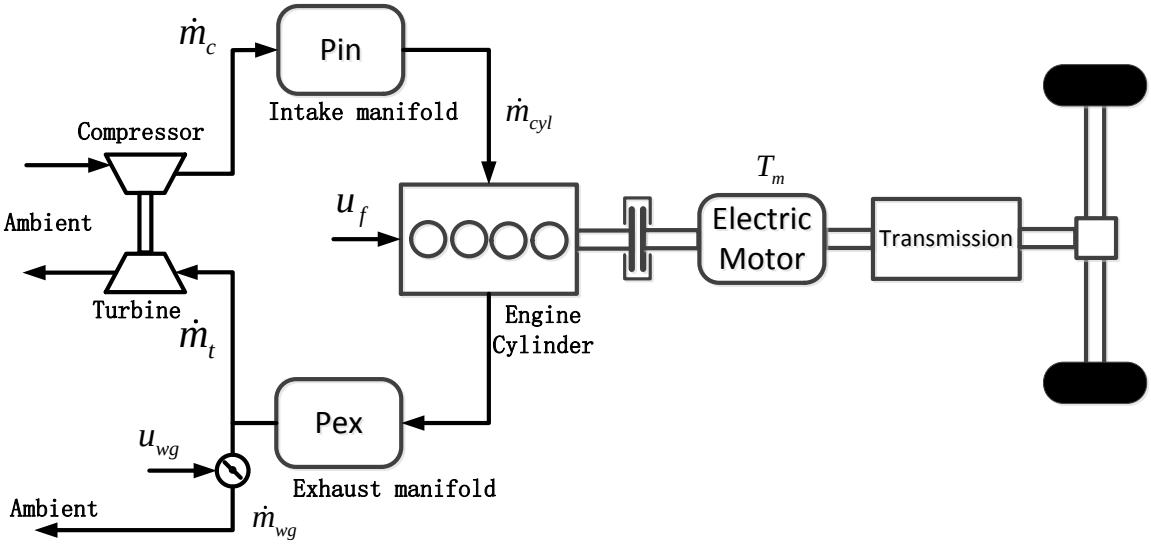

Figure 4.2: The studied parallel HEV powertrain structure.

4.2.1 Vehicle model

This paper adopts a longitudinal dynamic model for the vehicle described by Newtons second law in equation 4.1. F_d is the traction force. The drag force includes friction resistance, air drag force and grade resistance. g is gravitational constant. r_f is road friction coefficient. C_{drag} is air drag coefficient. ρ_{air} is air density, A_{front} is the effective area of air drag force. R_{tire} is the dynamic tire radius when the vehicle is moving. $m_{veh}$is the vehicle mass. m_{tire} is the equivalent mass of rotational components.

$$(m_{veh} + m_{tire})\frac{dV}{dt} = F_d - (m_{veh}gr_f + \frac{1}{2}C_{drag}\rho_{air}V^2A_{front} + m_{veh}g\sin\theta) \tag{4.1}$$

The inertias of Transmission, Differential and other drive shafts are lumped into vehicle inertia. Thus, the torque on wheels is the product of transmission input torque, gear ratio and final drive ratio.

4.2.2 Electric motor model

This paper adopts an efficiency-map-based model for electric motor. The motor output torque is assumed to be capable of instantly responding to its demand. Equation 4.2 describes the EM model [32]. P_m, T_m, ω_m are motor output power, torque and speed. P_{ele} is the consumed electric power. η_m is motor efficiency. T_m has upper and lower bounds related to motor speed.

$$P_{ele} = \frac{P_m}{\eta_m^{sign(T_m)}} = \frac{T_m\omega_m}{\eta_m^{sign(T_m)}} \tag{4.2}$$

4.2.3 Battery model

An equivalent resistance circuit is utilized in this paper to model the battery. The circuit current I is calculated from equation 4.3. V_{oc} is open circuit voltage. R_{in} is internal resistance. Thus, the battery SOC is modeled as in equation 4.4, where Q_{batt} is the battery capacity. The parameters of battery model are adopted from 2004 Toyota Prius battery pack [16].

$$I = \frac{V_{oc} - \sqrt{V_{oc}^2 - 4R_{in}P_{ele}}}{2R_{in}} \tag{4.3}$$

$$\dot{SOC} = -\frac{I}{Q_{batt}} \tag{4.4}$$

4.2.4 Engine model

The engine model includes air path dynamics associated with the turbocharger. Three state variables, intake manifold pressure P_{in}, exhaust manifold pressure P_{ex} and turbine shaft speed ω_t, are presented in equation 4.5. Here, R_a and R_e are gas constants of ambient air and exhaust gas; V_{in} and V_{ex} are volumes of intake and exhaust manifold; K_{in}, K_{ex} are temperatures in intake and exhaust manifold. $\dot{m}_c$ and $\dot{m}_t$ are mass flow rates through the compressor and turbine. $\dot{m}_{cyl}$ and $\dot{m}_f$ are air and fuel mass flow rate into the cylinder. $\dot{m}_{wg}$ is air mass flow rate through waste gate. W_t and W_c are the input powers of turbocharger shaft from the turbine and compressor, J_t is the shaft inertia. The details of the model, including the calculations of above mass flows and engine torque can be found in Mean Value Models (MVMs) proposed by [33]. Besides, the maximum torque at speed 1800$\sim$4000RPM is restricted

to 200Nm by controlling wastegate diameter at full load and the induced intake manifold pressure at full load. The corresponding maximum wastegate diameters at each engine speed setpoint are listed in Table 4.1. The major parameters of the vehicle are listed in Table 4.2.

$$\begin{aligned} \frac{dP_{in}}{dt} &= \frac{R_a K_{in}}{V_{in}}(\dot{m}_c - \dot{m}_{cyl}) \\ \frac{dP_{ex}}{dt} &= \frac{R_e K_{ex}}{V_{ex}}(\dot{m}_{cyl} + \dot{m}_f - \dot{m}_t - \dot{m}_{wg}) \\ \frac{d\omega_t}{dt} &= \frac{(W_t - W_c)}{J_t \omega_t} \end{aligned} \tag{4.5}$$

Table 4.1: Maximum wastegate diameters at each engine speed setpoint

Engine RPM	Wastegate Diameter (mm)
1000	0
1400	0
1800	0
2000	5.1887
2200	7.2782
2500	9.3180
2800	11.1503
3000	12.1713
3200	12.9709
3500	13.9679
4000	14.9245

Table 4.2: Major model parameters of the studied HEV

	Parameters	Values
Vehicle	Vehicle mass (kg)	1900
	Frontal area (m2)	2
	Air drag coefficient	0.32
	Tire dynamic radius (m)	0.3
	Road friction coefficient	0.015
Engine	Displacement (L)	1.4
	Maximum torque (N-m)	200@1800-4000RPM
Electric motor	Motor maximum torque (N-m)	400
	Motor maximum power (Kw)	50
Battery	Capacity (A-h)	6.5
Transmission	Gear ratio	2.125/1.25/1/0.72
	Final drive ratio	3.2

4.3 Problem formation

The aim of the energy management strategy is to optimize the fuel consumption in a given driving cycle, and meanwhile to satisfy other requirements, including tracking reference vehicle speed profile, SOC charge sustaining, physical constraints of power components, system dynamics constraints, etc.. Due to the existence of a clutch and a fixed–gear transmission, engine power and motor power are supposed to be decoupled by disengaging clutch in the stages of vehicle start–up and gear shifting.

To simplify the problem, EMS is not activated in these situations and the control in the couple–decouple transition periods is not in the scope of this paper.

System dynamics

Combining battery SOC dynamics and engine air path dynamics, a four-state-three-input nonlinear system is formed in equation 4.6. Here, $[P_{in}, P_{ex}, \omega_t, SOC]$ is the state vector representing intake manifold pressure, exhaust manifold pressure, turbine speed and SOC respectively. $[u_f, u_{wg}, T_m]$ is the input vector representing fuel injection mass, wastegate diameter and motor torque. $[N_e, T_{req}]$ is the exogenous parameter vector representing engine speed and total requested torque. f_1, f_2, f_3 are functions of air path dynamics equivalent to equation 4.5. f_4 is the SOC dynamics equivalent to equation 4.4.

$$\begin{cases} \dot{x}_1 = f_1\left(P_{in}, \omega_t, N_e, T_{req}\right) \\ \dot{x}_2 = f_2\left(P_{in}, P_{ex}, \omega_t, u_f, u_{wg}, N_e, T_{req}\right) \\ \dot{x}_3 = f_3\left(P_{in}, P_{ex}, \omega_t, N_e, T_{req}\right) \\ \dot{x}_4 = f_4\left(SOC, T_m\right) \end{cases} \tag{4.6}$$

Path constraints

The path constraints are equality and inequality mixed functions of state and control variables, which are applied on part of optimization horizon [34]. There are two path constraints involved in this study. Equation 4.7 describes that the sum torque of engine and motor should meet the torque requested from the driver in order to satisfy the requirement of vehicle speed tracking. Equation 4.8 illustrates the relationship between fuel injection mass and intake manifold pressure as a consequence of air–fuel–ratio(AFR) control. The calculation of $u_{f,max}$ is presented in equation 4.9.

$$T_e(u_f, \omega_e) + T_m = T_{req} \tag{4.7}$$

$$u_f \leq u_{f,\max}(P_{in}) \tag{4.8}$$

V_d is engine displacement, η_{vol} is the relative volumetric efficiency, and T_{amb} is the ambient temperature. AFR^* is the lower bound of air–fuel ratio, which is set to 15 in this paper.

$$u_{f,\max} = \frac{1}{4 \times 10^{-6}} \frac{V_d P_{in} \eta_{vol}}{AFR^* T_{amb} R_a} \tag{4.9}$$

Physical constraints

The state and control variables all have their physical limits, which are described in equation 4.10. $\boldsymbol{X} = [P_{in}, P_{ex}, \omega_t, SOC]$, $\boldsymbol{U} = [u_f, u_{wg}, T_m]$. These bounds are set to reasonable constants.

$$\begin{aligned} \boldsymbol{X}_{\min} \leq \boldsymbol{X} \leq \boldsymbol{X}_{\max} \\ \boldsymbol{U}_{\min} \leq \boldsymbol{U} \leq \boldsymbol{U}_{\max} \end{aligned} \tag{4.10}$$

MPC-based EMS formation

When the clutch is engaged and the acceleration demand occurs, the MPC-based EMS is active. The energy consumption in a prediction horizon is minimized by equation 4.11. It consists of both total costs from fuel and electrical path. Coefficient μ is the weighting factor between them. P is the length of prediction horizon. The minimization is constrained by system dynamic, path constraints and physical constraints.

$$J(k) = \sum_{i=0}^{P} \dot{m}_f(t_k + i)\Delta t + \mu(SOC(t_k + P) - SOC(t_k)) \tag{4.11}$$

The exogenous input T_{req} is predicted by equation 4.12 inside the MPC based supervisory controller, except for the first step of prediction where T_{req} is provided by the PID controller. Engine speed and all states are assumed to be measurable. V_{ref} is the reference vehicle speed. i_g and i_f are the gear ratio and final drive ratio.

$$T_{req} = \frac{R_{tire}}{i_g i_f}(m_{veh} + m_{tire})\frac{dV_{ref}}{dt} + (m_{veh} g r_f + \frac{1}{2} C_{drag} \rho_{air} V_{ref}^2 A_{front} + m_{veh} g \sin\theta) \tag{4.12}$$

$$TEC = Fuelcons(T) + \lambda(SOC(T) - SOC(0)) \tag{4.13}$$

Since a constrained, highly nonlinear optimal control problem should be solved in the supervisory controller, dynamic programming is found to be the most reliable solution based on our research. A forward DP algorithm is implemented and demonstrated in Appendix B. Some preliminary results have been presented in our previous work [20] to prove the effectiveness of fuel saving for the MPC based EMS. Its primary advantage is the ability of predicting the cylinder air charge and engine torque in transients.

In addition, a total equivalent consumption (TEC) is defined in equation 4.13 to compare different results in Section V. t_f indicates the end time of driving mission. λ is the conversion factor which has the same value and unit as μ in equation 4.11.

4.4 Adaptive control–step learning MPC

In MPC algorithms, a few steps of inputs are implemented after calculating the best control sequence in a prediction horizon. Then, the process moves forward by

the executed control inputs and repeats the prediction until the process is completed. For example, in Fig. 4.3, the prediction steps of Case 1 and 2 are all set to 3 and their control steps are 3 and 2 respectively. Assuming the length of the process is 6 steps, Case 2 needs to conduct 3 times of prediction, but Case 1 only needs twice. In other words, Case 1 consumes one third less computational resource than Case 2. Following this idea, the computational cost $cost_{cal}$ can be parameterized as in equation 4.14. N_a is the approximate total length of the process and S_c is the control step.

$$cost_{cal} = \frac{N_a}{S_c} \tag{4.14}$$

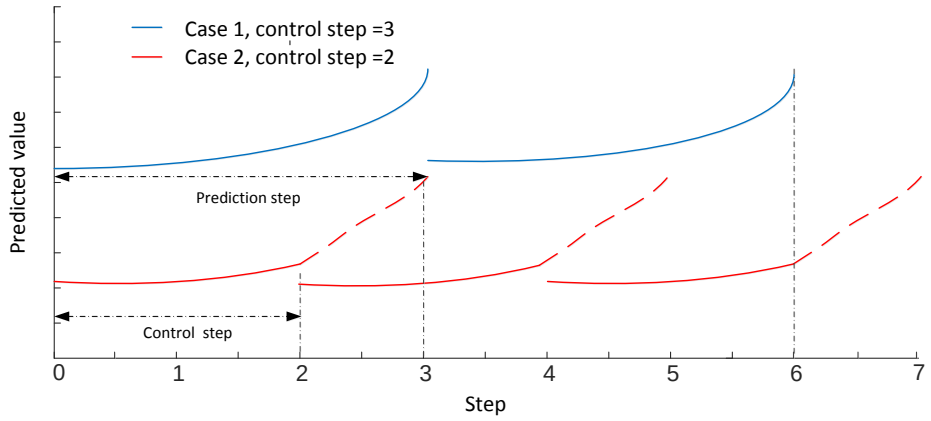

Figure 4.3: A diagram showing the effects of different control steps in the same length of process

Another consideration in determining control step is originated from the evaluation of confidence to the MPC controller. Since applying more control steps generated from the prediction introduces more uncertainties, it may cause bigger mismatch between the actual and requested torque, and hence poorer speed tracking performance.

In order to quantize this "confidence", the actual vehicle speed in the next control horizon should be estimated according to the information from the last control horizon. The relationship between acceleration and requested torque are investigated here. First, a generalized acceleration is defined in equation 4.15. $\boldsymbol{V_{act,old}}$ represents the actual vehicle speed vector in the last control horizon and its dimension is $S_c + 1$. $\boldsymbol{K_{old}}$ is the acceleration vector from the last control horizon.

$$\boldsymbol{K_{old}}(j) = \frac{\boldsymbol{V_{act,old}}(j+1) - \boldsymbol{V_{act,old}}(j)}{j+1-j}, j = 1, ..., S_c \tag{4.15}$$

$$\begin{aligned} C_{mean} &= \sum_{i=1}^{S_c} \mathbf{C}(i)/S_c \\ \boldsymbol{C}(i) &= \left| \frac{\mathbf{K_{old}}(j)}{\boldsymbol{T_{req,old}}(j)} \right| \end{aligned} \tag{4.16}$$

In equation 4.16, the vector of requested torque in the last horizon is stored in $\boldsymbol{T_{req,old}}$. Every element of vector C is the absolute value of corresponding ratio between $\boldsymbol{K_{old}(j)}$ and $\boldsymbol{T_{req,old}(j)}$. Then, the mean value of $\boldsymbol{C}$ is calculated as C_{mean}. C_{mean} is presumed to be constant in the two consecutive control horizons. Therefore, in the next control horizon it can be used to predict the actual acceleration and speed vectors, namely, $\boldsymbol{K_{new}}$ and $\boldsymbol{V_{act,new}}$, based on the given new requested torque vector $\boldsymbol{T_{req,new}}$. The calculations are shown in equations 4.17 and 4.18.

$$\boldsymbol{K_{new}}(i) = \boldsymbol{T_{req,new}}(j) \cdot C_{mean} \tag{4.17}$$

$$\boldsymbol{V_{act,new}}(j+1) = \boldsymbol{V_{act,new}}(j) + \boldsymbol{K_{new}}(j) \tag{4.18}$$

The "Confidence" related to speed tracking performance is measured by Root-Mean-Squared Error (RMSE) between actual speed $\boldsymbol{V_{act,new}}$ and reference speed $\boldsymbol{V_{ref,new}}$ shown in equation 4.19. High RMSE infers less confidence on the control inputs.

$$cost_{conf} = \sqrt{\frac{(\boldsymbol{V^T_{act,new}} - \boldsymbol{V^T_{ref,new}})(\boldsymbol{V_{act,new}} - \boldsymbol{V_{ref,new}})}{\dim(\boldsymbol{V_{act,new}})}} \tag{4.19}$$

To be noted, $cost_{conf}$ is fundamentally a function of control step. The total cost $cost_{sc}$, which is associated with the control step selection, is defined as the sum of weighted $cost_{cal}$ and $cost_{conf}$. Considering N_a is also a constant, equation 4.20 is formed. Here, N_a is lumped into the weight γ on $cost_{conf}$. Since $cost_{cal}$ yields a dimensionless variable whose range is from 0 to 1, we can first normalize $cost_{conf}$ by dividing it with a measured $cost_{conf}$ in a period of driving-cycle simulation. Then, the two terms in equation 4.20 are quantified by the same magnitude, and it provides convenience for choosing γ. According to Fig. 4.4, γ is finally set to 0.1 considering both vehicle speed MSE and TEC.

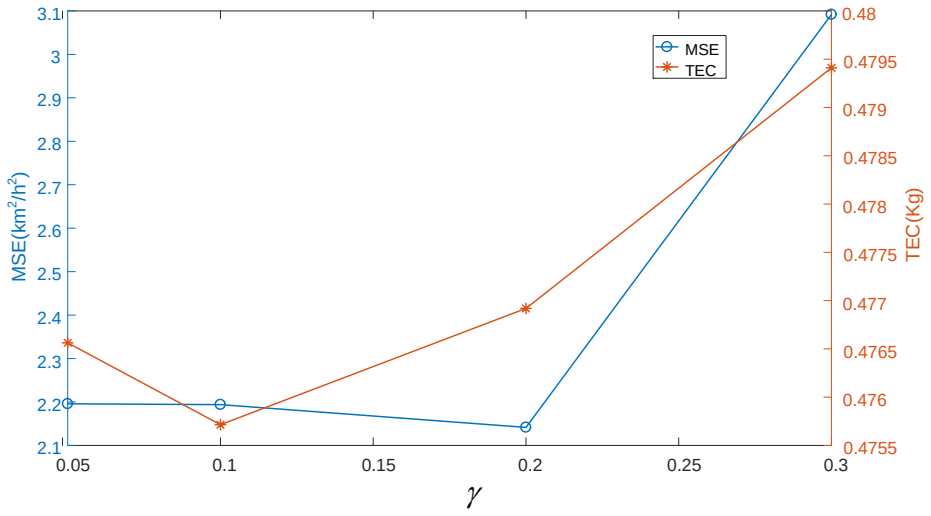

Figure 4.4: The effect of weighting factor γ on speed MSE and TEC in ACLMPC

$$cost_{sc}(S_c) = \frac{1}{S_c} + \gamma \cdot cost_{conf}(S_c) \tag{4.20}$$

The proposed ACLMPC structure is illustrated in Fig. 4.5. Z^{-C} represents the time delay of one control horizon. Comparing to the regular MPC controller, ACLMPC adds an adaptive control–step regulator that estimates the best control step at the beginning of each prediction horizon.

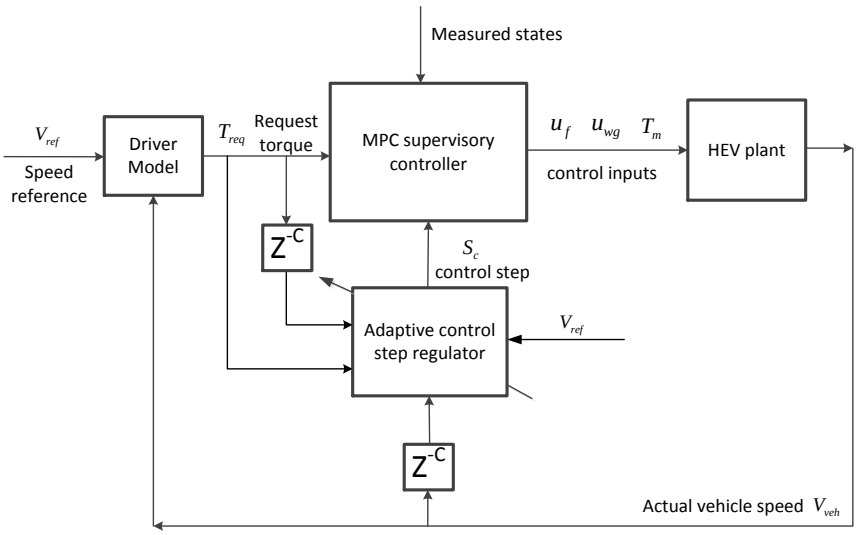

Figure 4.5: The scheme of ACLMPC

4.5 Results discussion for ACLMPC

First, the control performances of applying different prediction steps on the same system and problem are compared in Table 4.3. One step represents one second in the real world. The chosen prediction steps are integers ranging from 1 to 7, and the control steps are all set to 1. The performance comparison of vehicle speed

tracking, fuel consumption and SOC consumption is shown to empirically obtain the best prediction step.

The values of fuel consumption and SOC at the end of driving cycle are listed in column 3 and 4 of Table 4.3. We can see that the case whose prediction step is 3 has the lowest TEC. Another indicator of control performance is vehicle speed tracking. The mean squared errors (MSEs) between the reference and actual speed are calculated. Their values are close since the Proportional–Integral–Derivative (PID) parameters in driver model are identical for all seven cases. The same PID controller can constantly regulate speed and maintain the similar error in each case, however, the fuel and SOC consumption vary due to different prediction step. Considering those performance indicators as a whole, this paper chooses 3 prediction step as an "optimum".

Table 4.3: MSEs of speed tracking, fuel consumption, SOC and TECs at the end of driving cycle for different prediction steps

Prediction step	MSE(km2/h2)	Fuel consumption(kg)	SOC	TEC(kg)
1	2.0747	0.4735	0.5986	0.4738
2	2.0739	0.4708	0.5881	0.4737
3	2.0763	0.4735	0.5997	0.4736
4	2.0735	0.4736	0.5998	0.4737
5	2.0728	0.4721	0.5924	0.4739
6	2.0710	0.4730	0.5849	0.4766
7	2.0751	0.4732	0.5978	0.4737

The main advantage of ACLMPC is its ability of balancing the requirements of

control accuracy and computational efficiency. In order to demonstrate the merits of this method, three other cases with different constant control steps are also simulated and compared with the proposed one. Other control parameters, such as PID in driver model, factor μ in equation 4.11, etc, are identical in the four cases. The prediction steps of them are set to 3 and control steps are 1, 2, 3 and adaptive. Similarly, the trajectories of SOC, fuel consumption and speed tracking performance etc. are considered as major performance indices and compared. In the legend of figures in this section, "StepCtl" represents "control step" and "StepCtl Adaptive" is the proposed ACLMPC.

Fig. 4.6 shows the SOC trajectories. Among the three cases with constant control steps, the one with 3 control step is the worst case. It drains much more battery energy than the other two and cannot maintain charge balance. "StepCtl=2" comes at the second place and "StepCtl=1" is the best. Likewise, the fuel consumption trajectories in Fig. 4.7 show the similar order from smallest to largest fuel consumption. In Fig. 4.8, the sub–plot "Difference" of TECs gives a clearer picture of the amount of total energy cost. This "Difference" is calculated by subtracting the TEC of "StepCtl=1" from TECs of all cases. If the result is positive, it means that the TEC of this case is more than "StepCtl=1". Subsequently, the order of TECs, which is "StepCtl=1"<"StepCtl=2"<"StepCtl=3", validates our ideas that larger control step could introduce more inferior fuel performance.

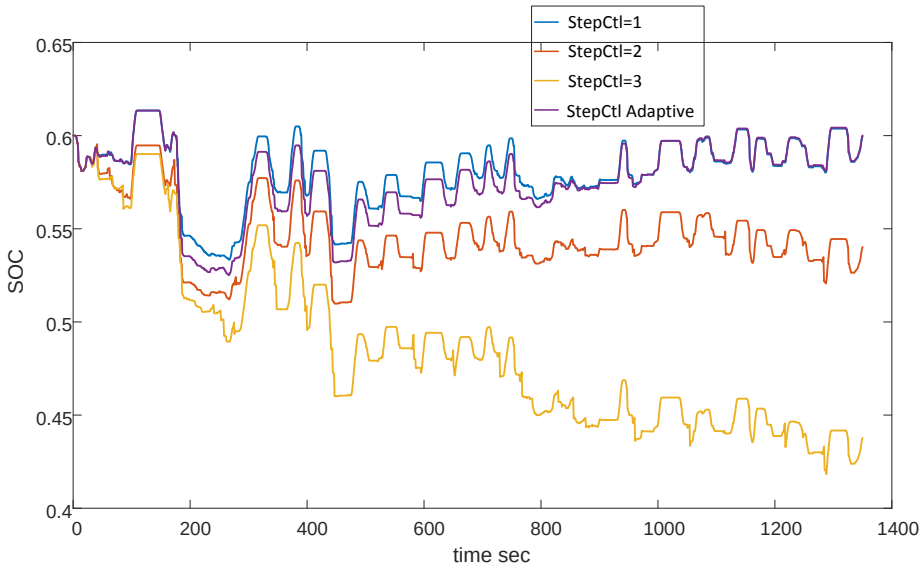

Figure 4.6: Comparison of SOC trajectories for control step=1, 2, 3, Adaptive

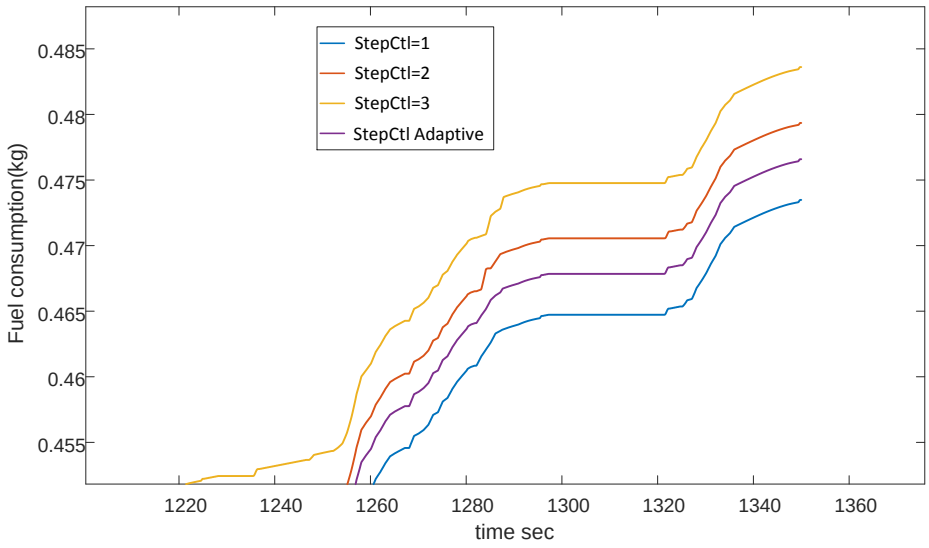

Figure 4.7: Comparison of fuel consumption at the end of driving cycle trajectories for control step=1, 2, 3, Adaptive

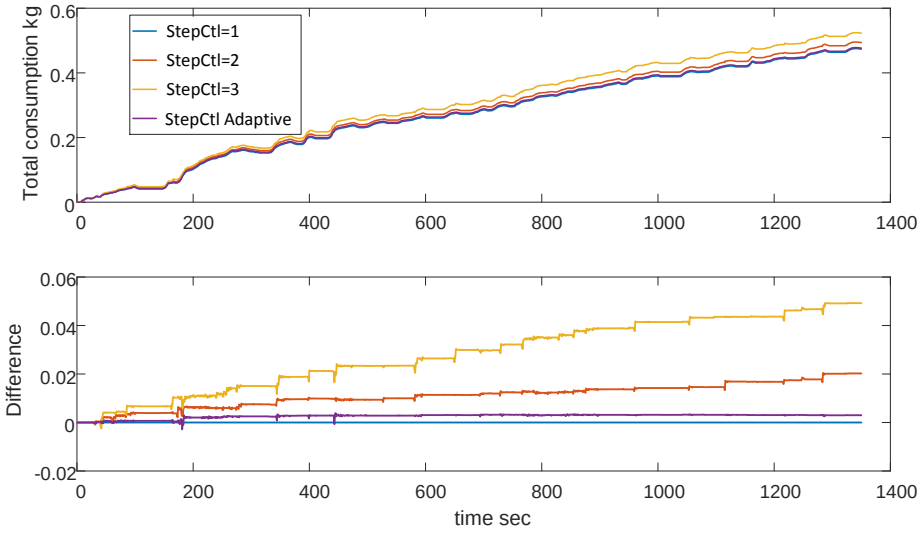

Figure 4.8: Total Equivalent Consumptions (TECs) for control step=1, 2, 3, Adaptive

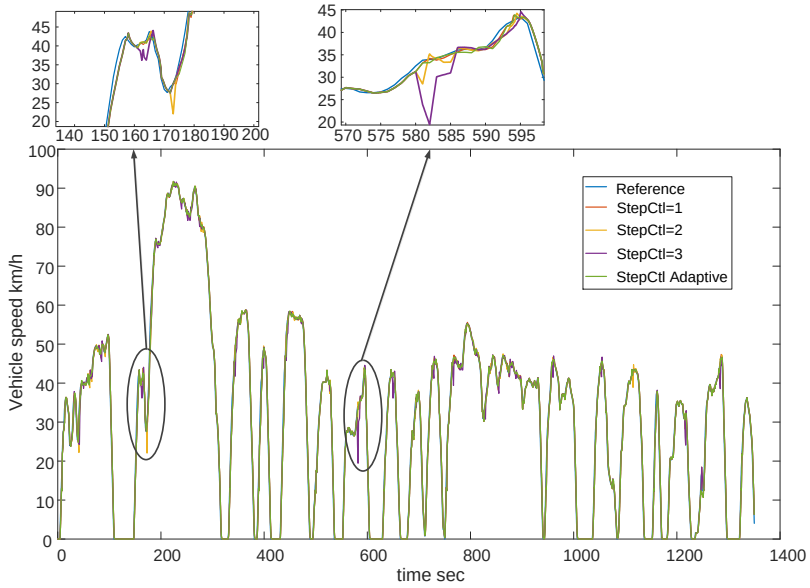

Figure 4.9: Reference vehicle speed and actual vehicle speed for control step=1, 2, 3, Adaptive

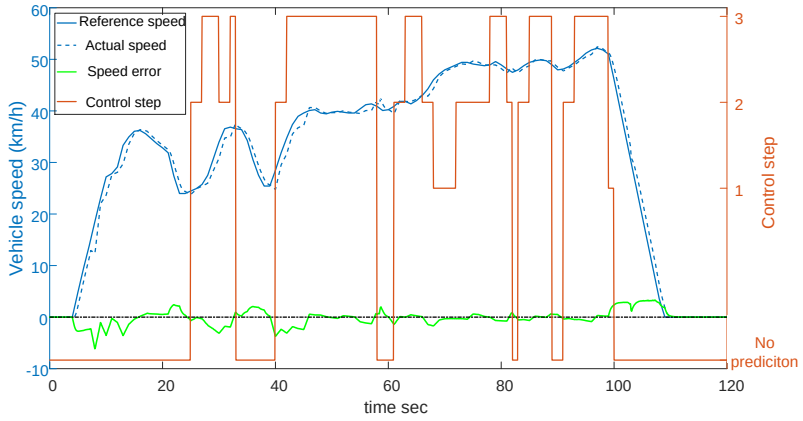

Figure 4.10: Reference vehicle speed and actual vehicle speed for control step=1, 2, 3, Adaptive. "Speed error" is the difference between vehicle reference and actual speed

For the fourth case, ACLMPC illustrates a close SOC and fuel consumption trajectory compared to "StepCtl=1". Its TEC is considerably better than "StepCtl=2" and "StepCtl=3", although not as good as "StepCtl=1". Besides, the speed tracking performance in Fig. 4.9 shows that both "StepCtl=2" and "StepCtl=3" fails to follow the reference vehicle speed in some portions of the driving cycle, i.e. during 150s∼180s and 570s∼590s. However, "StepCtl=Adaptive" demonstrates its decency over the entire driving cycle. In case "StepCtl=Adaptive", when the discrepancy between the actual and reference speed is relatively small, the control step is set large as shown in Fig. 4.10. Larger control step induces bigger accumulation of model error and speed mismatch. Thus, the ACLMPC starts to reduce the control step and maintain the speed tracking performance.

Meanwhile, larger mismatch also leads to higher total requested torque as shown in Fig. 4.11, since the feedback control tends to compensate the mismatch by increasing torque demand. Therefore, more energy should be consumed no matter how EMS

distributes power demands of engine and motor. Sometimes the requested torque rises incredibly and goes beyond the physical limit, such as 700Nm in 580∼585s for "StepCtl=3". Our proposed ACLMPC tactically avoids this kind of large mismatches by properly regulating control step, and finally contributes to energy saving. The detailed statistics of performance indices can be found in Table 4.4.

Table 4.4: Comparison of speed tracking MSEs, fuel consumptions, SOCs and TECs at the end of driving cycle for "StepCtl 1", "StepCtl 2", "StepCtl 3", "StepCtl Adaptive"

Cases	MSE(km2/h2)	Fuel consumption(kg)	SOC	TEC(kg)
StepCtl 1	2.1064	0.4688	0.5997	0.4736
StepCtl 2	2.3316	0.4752	0.5402	0.4938
StepCtl 3	3.0459	0.4730	0.4377	0.5228
StepCtl Adaptive	2.1940	0.4750	0.5964	0.4757

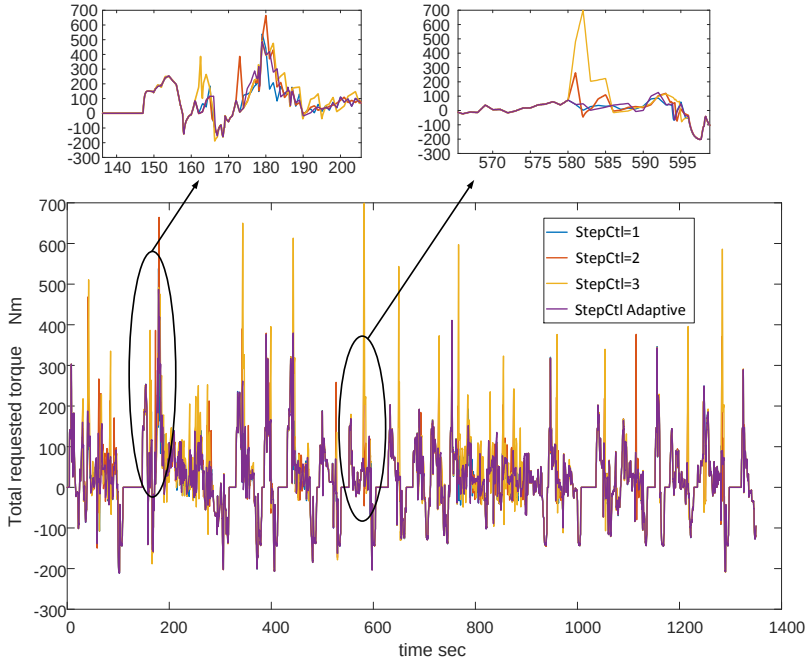

Figure 4.11: Total requested torque to drive vehicle for control step=1, 2, 3, Adaptive

Evaluating the computing time of all energy management strategies is not easy, because the measured time of simulation includes both the computing time of control law and plant model. Here, we develop a reasonable, discrete method to analyze the computational effort. Fig. 4.12 shows the sequences of applied control steps for the four cases. Note that MPC supervisory controller is not always active due to the parts of deceleration, low vehicle speed and gear shift in the driving cycle. The control steps in those parts are arbitrarily set to "-1" to indicate that no prediction process occurs. In fact, in those parts the duplicate, simple, computationally efficient strategy is adopted to distribute requested torque in all four cases. We can see the different switching points between the simple strategy and MPC strategy as a result of different control–step selections. In addition, the computing time of the simple

strategy in those parts is around 0.01 seconds for one control action on our computer which has an Intel(R) Core(TM) i7–3770 CPU. The computing time for one 3–step prediction in MPC based EMSs is 3.7 seconds according to the average test results. The computing time of driving the plant model is nearly 2 seconds for 1 second in real time. Thus, the time of the "fast", simple strategy can be ignored when evaluating the total time. Only the time of prediction in MPC algorithm counts.

Based on this idea, the numbers of incident of effective control steps (1, 2, or 3) are obtained in Table 4.5. Each time of implementing those control steps associates with a calculation of 3–step prediction. Therefore, the total time of implementing control strategy can be approximated by the product of the number of predictions and the computing time per prediction. From the 5th column of Table 4.5, we can see that the case "StepCtl=1", unsurprisingly, has the highest computational effort. The burden of ACLMPC resembles the one with 2 control step and is almost only 1/2 of the one with 1 control step. The estimated time of implementing MPC is listed in the 6th column of Table 4.5.

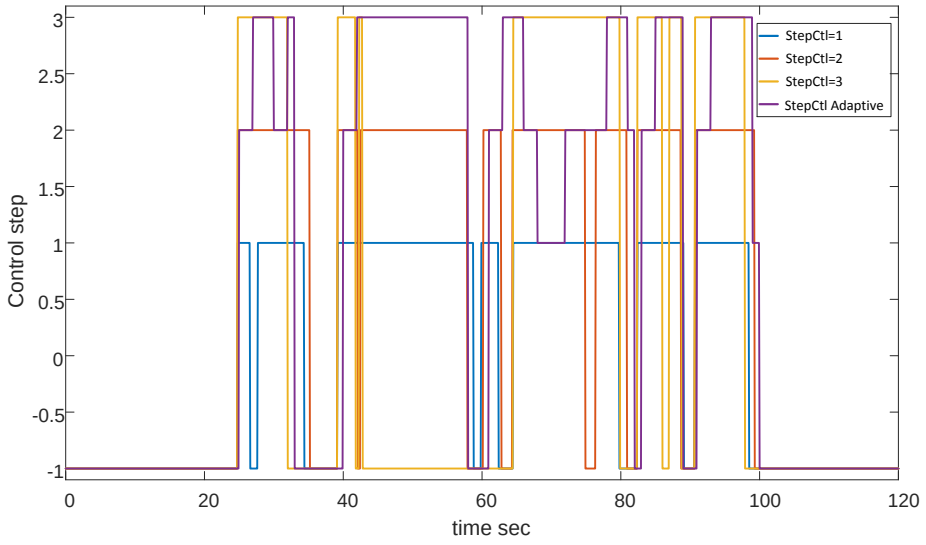

Figure 4.12: Comparison of the control step selections for control step=1, 2, 3, Adaptive

Table 4.5: Number of occurrence of different control steps existing in the four cases StepCtl=1, 2, 3, Adaptive and their total number of prediction

Cases	Number of 1 step	Number of 2 step	Number of 3 step	Number of predictions	Estimated computing time of MPC(min)
StepCtl 1	384	0	0	384	23.68
StepCtl 2	0	197	0	197	12.15
StepCtl 3	0	0	117	117	7.22
StepCtl Adaptive	65	74	69	208	12.83

4.6 Adaptability test

Last section demonstrates the advantages of the proposed ACLMPC in both control performance and computational effort. This section aims to test its adaptability. The adaptability defined in this paper is the strategy's ability of not being affected by the change of driving cycle. Three sets of vehicle speed profile are formulated to serve this purpose. They are the original UDDS cycle, 105% and 95% speed of the original UDDS cycle. Those speed profiles replace the one that is used for requested torque prediction in equation 4.12, and all other control parameters related to energy management remain the same. The reference speed for driver model is still the original UDDS. In other words, the variation of driving cycle only affects the exogenous variables in the energy management strategies. Because in this paper MPC strategies integrate output feedback mechanism to be able to observe the requested torque at each start of prediction, it is naturally inherited with some extent of adaptability. By adding the new control–step regulator in ACLMPC, the adaptability can be improved while maintaining relatively low computational burden.

Similarly, the aforementioned three sets of driving cycle are applied on "StepCtl 1", "StepCtl 2", "StepCtl 3" and "StepCtl Adaptive" cases, in which the prediction steps are all 3. For each case, the MSEs of speed tracking and TECs are obtained in Table 4.6. In order to show the difference of their adaptabilities, the mean-squared deviation of performance indices in the perturbed UDDS cycles from those in the original UDDS, are calculated. As shown in equation 4.21, MSDV2O represents the mean squared deviation, Ind_i is any index for the perturbed driving cycle, and Ind_o is any index for the original driving cycle. n is the number of total perturbed driving cycles. MSDV2O implies the sensitivity of this method to the uncertainty of driving

cycle. Larger MSDV2Os denotes higher sensitivity and hence lower adaptability.

$$MSDV2O = \frac{1}{n}\sum_{i=1}^{n}(Ind_i - Ind_o) \tag{4.21}$$

Table 4.7 lists the calculated MSDV2Os for MSE of speed tracking and TEC in the four cases. It is clearly observed that "StepCtl 1" has the lowest MSDV2O by comparing both indices, which suggests its best adaptability to the variation of driving cycle. It also shows that larger MSDV2O can be caused by elongating the control horizon, meaning less robustness. The ACLMPC yields its MSDV2Os between "StepCtl 1" and "StepCtl 2" and demonstrates a fairly competent adaptability.

4.7 Conclusion

In this paper, a novel MPC-based structure incorporating with an adaptive control–step regulator has been adopted to solve an energy management problem for turbocharged-diesel-engine HEV powertrain. The unitized engine model involves air path dynamics of a turbocharger that can predict engine transient torque. Dynamic programing is used to solve the induced optimal control problem in the prediction horizon. The comparison of seven cases with different prediction steps is conducted to determine that 3–step prediction has the best speed tracking and fuel performance. Then, the proposed ACLMPC is designed and integrated into MPC structure. By comparing it to the performances of constant control–step strategies, ACLMPC reveals a resemblance of fuel and SOC performances to the strategy with fixed 1 control step (the best one), and meanwhile nearly halves its computational effort. The adaptability test also shows an excellent adaptability of ACLMPC to the variation of driving cycle.

Table 4.6: MSE of speed tracking, TEC for four cases "StepCtl 1", "StepCtl 2", "StepCtl 3", "StepCtl Adaptive"

Case	Speed no change		Speed +5%		Speed -%5	
	MSE	TEC	MSE	TEC	MSE	TEC
StepCtl 1	2.1063	0.4736	2.1043	0.4724	2.1043	0.4724
StepCtl 2	2.3316	0.4938	2.3559	0.5012	2.2688	0.4938
StepCtl 3	3.0459	0.5228	2.9351	0.5187	3.0124	0.5159
StepCtl Adaptive	2.1958	0.4757	2.1697	0.4778	2.1596	0.4767

Table 4.7: Comparison of MSDV2O for four cases "StepCtl 1", "StepCtl 2", "StepCtl 3", "StepCtl Adaptive"

Case	MSDV2O	
	MSE	TEC
StepCtl 1	2.64E-06	9.13E-7
StepCtl 2	1.51E-3	1.85E-5
StepCtl 3	4.46E-3	2.10E-5
StepCtl Adaptive	6.64E-4	1.83E-6

Reference

[1] Ali Emadi, Kaushik Rajashekara, Sheldon S Williamson, and Srdjan M Lukic. Topological overview of hybrid electric and fuel cell vehicular power system architectures and configurations. *IEEE Transactions on Vehicular Technology*, 54(3):763–770, 2005.

[2] CC Chan. An overview of electric vehicle technology. *Proceedings of the IEEE*, 81(9):1202–1213, 1993.

[3] Yalian Yang, Xiaosong Hu, Huanxin Pei, and Zhiyuan Peng. Comparison of power-split and parallel hybrid powertrain architectures with a single electric machine: dynamic programming approach. *Applied Energy*, 168:683–690, 2016.

[4] Zheng Chen, Bing Xia, Chenwen You, and Chunting Chris Mi. A novel energy management method for series plug-in hybrid electric vehicles. *Applied Energy*, 145:172–179, 2015.

[5] Syuan-Yi Chen, Yi-Hsuan Hung, Chien-Hsun Wu, and Siang-Ting Huang. Optimal energy management of a hybrid electric powertrain system using improved particle swarm optimization. *Applied energy*, 160:132–145, 2015.

[6] Chan-Chiao Lin, Huei Peng, Jessy W Grizzle, and Jun-Mo Kang. Power management strategy for a parallel hybrid electric truck. *IEEE transactions on control systems technology*, 11(6):839–849, 2003.

[7] Sebastien Delprat, Jimmy Lauber, Thierry-Marie Guerra, and Janette Rimaux. Control of a parallel hybrid powertrain: optimal control. *IEEE transactions on Vehicular Technology*, 53(3):872–881, 2004.

[8] Antonio Sciarretta and Lino Guzzella. Control of hybrid electric vehicles. *IEEE Control systems*, 27(2):60–70, 2007.

[9] Lorenzo Serrao, Simona Onori, and Giorgio Rizzoni. A comparative analysis of energy management strategies for hybrid electric vehicles. *Journal of Dynamic Systems, Measurement, and Control*, 133(3):031012, 2011.

[10] Fengjun Yan, Junmin Wang, and Kaisheng Huang. Hybrid electric vehicle model predictive control torque-split strategy incorporating engine transient characteristics. *IEEE transactions on vehicular technology*, 61(6):2458–2467, 2012.

[11] Farzad Rajaei Salmasi. Control strategies for hybrid electric vehicles: Evolution, classification, comparison, and future trends. *IEEE Transactions on vehicular technology*, 56(5):2393–2404, 2007.

[12] Stefano Di Cairano, Diana Yanakiev, Alberto Bemporad, Ilya V Kolmanovsky, and Davor Hrovat. An mpc design flow for automotive control and applications to idle speed regulation. In *Decision and Control, 2008. CDC 2008. 47th IEEE Conference on*, pages 5686–5691. IEEE, 2008.

[13] Chuan Hu, Rongrong Wang, Fengjun Yan, Yanjun Huang, Hong Wang, and Chongfeng Wei. Differential steering based yaw stabilization using ismc for independently actuated electric vehicles. *IEEE Transactions on Intelligent Transportation Systems*, 19(2):627–638, 2018.

[14] Rongrong Wang, Hui Zhang, and Junmin Wang. Linear parameter-varying controller design for four-wheel independently actuated electric ground vehicles with active steering systems. *IEEE Transactions on Control Systems Technology*, 22(4):1281–1296, 2014.

[15] Rongrong Wang and Junmin Wang. Actuator-redundancy-based fault diagnosis for four-wheel independently actuated electric vehicles. *IEEE Transactions on Intelligent Transportation Systems*, 15(1):239–249, 2014.

[16] Rui Wang and Srdjan M Lukic. Dynamic programming technique in hybrid electric vehicle optimization. In *Electric Vehicle Conference (IEVC), 2012 IEEE International*, pages 1–8. IEEE, 2012.

[17] Cristian Musardo, Giorgio Rizzoni, Yann Guezennec, and Benedetto Staccia. A-ecms: An adaptive algorithm for hybrid electric vehicle energy management. *European Journal of Control*, 11(4-5):509–524, 2005.

[18] Namwook Kim, Sukwon Cha, and Huei Peng. Optimal control of hybrid electric vehicles based on pontryagin's minimum principle. *IEEE Transactions on Control Systems Technology*, 19(5):1279–1287, 2011.

[19] Roberto Mura, Vadim Utkin, and Simona Onori. Energy management design in hybrid electric vehicles: a novel optimality and stability framework. *IEEE Transactions on Control Systems Technology*, 23(4):1307–1322, 2015.

[20] Yi Huo and Fengjun Yan. A predictive energy management strategy for hybrid electric powertrain with a turbocharged diesel engine. *Journal of Dynamic Systems, Measurement, and Control*, 2018.

[21] Michiel Koot, John TBA Kessels, Bram De Jager, WPMH Heemels, PPJ Van den Bosch, and Maarten Steinbuch. Energy management strategies for vehicular electric power systems. *IEEE transactions on vehicular technology*, 54(3):771–782, 2005.

[22] Hoseinali Borhan, Ardalan Vahidi, Anthony M Phillips, Ming L Kuang, Ilya V Kolmanovsky, and Stefano Di Cairano. Mpc-based energy management of a power-split hybrid electric vehicle. *IEEE Transactions on Control Systems Technology*, 20(3):593–603, 2012.

[23] Saida Kermani, Sebastien Delprat, Thierry-Marie Guerra, Rochdi Trigui, and Bruno Jeanneret. Predictive energy management for hybrid vehicle. *Control Engineering Practice*, 20(4):408–420, 2012.

[24] Rahul Shridhar and Douglas J Cooper. A tuning strategy for unconstrained multivariable model predictive control. *Industrial & engineering chemistry research*, 37(10):4003–4016, 1998.

[25] Ralph F Hinde Jr and Douglas J Cooper. A pattern-based approach to excitation diagnostics for adaptive process control. *Chemical engineering science*, 49(9):1403–1415, 1994.

[26] Jorge Otávio Trierweiler and Luciano André Farina. Rpn tuning strategy for model predictive control. *Journal of Process Control*, 13(7):591–598, 2003.

[27] Jorge L Garriga and Masoud Soroush. Model predictive control tuning methods: A review. *Industrial & Engineering Chemistry Research*, 49(8):3505–3515, 2010.

[28] Juan M Grosso, Carlos Ocampo-Martínez, and Vicenç Puig. Learning-based tuning of supervisory model predictive control for drinking water networks. *Engineering Applications of Artificial Intelligence*, 26(7):1741–1750, 2013.

[29] JH Van der Lee, WY Svrcek, and BR Young. A tuning algorithm for model predictive controllers based on genetic algorithms and fuzzy decision making. *ISA transactions*, 47(1):53–59, 2008.

[30] Ashraf Al-Ghazzawi, Emad Ali, Adnan Nouh, and Evanghelos Zafiriou. On-line tuning strategy for model predictive controllers. *Journal of Process Control*, 11(3):265–284, 2001.

[31] Miroslav Baric, Mato Baotic, and Manfred Morari. On-line tuning of controllers for systems with constraints. In *Decision and Control, 2005 and 2005 European Control Conference. CDC-ECC'05. 44th IEEE Conference on*, pages 8288–8293. IEEE, 2005.

[32] Jinming Liu and Huei Peng. Modeling and control of a power-split hybrid vehicle. *IEEE transactions on control systems technology*, 16(6):1242–1251, 2008.

[33] Lars Eriksson. Modeling and control of turbocharged si and di engines. *Oil & Gas Science and Technology-Revue de l'IFP*, 62(4):523–538, 2007.

[34] Benoit Chachuat. Nonlinear and dynamic optimization: From theory to practice. Technical report, 2007.

Symbol III

PID are defined in the Symbol III as coefficients that directly multiplies the speed error, and the integral, derivative of speed error. The calculated products should multiply vehicle mass before they are used in the simulation. More model-related parameters are referred to Symbol II.

g	gravitational acceleration	9.8 m/s^2
i_g	transmission gear ratio	
i_f	final drive ratio	3.2
$\dot{m}_f$	fuel flow rate	
m_{veh}	vehicle mass	1900 kg
$\dot{m}_c$	mass flow rate through compressor in map	
$\dot{m}_t$	mass flow rate through turbine in map	
$\dot{m}_{cyl}$	cylinder air flow rate	
$\dot{m}_{wg}$	air mass flow rate through wastegate	
n	total number of original and perturbed driving cycles	
r_f	road friction coefficient	0.015
u_f	fuel injection mass	
$u_{f,\min}$	minimum fuel injection mass	0 mg/cycle
$u_{f,\max}$	maximum fuel injection mass	60 mg/cycle
u_{wg}	wastegate diameter	
$u_{wg,\min}$	minimum wastegate diameter	0 mm
$u_{wg,\max}$	maximum wastegate diameter	
A_{front}	effective area of air drag force	2 m^2
AFR^*	stoichiometric air fuel ratio	15

C_{drag}	drag coefficient	0.32
C_{mean}	mean value of absolute ratios between acceleration and torque vector	
$Cost_{cal}$	the cost related to computational load	
$Cost_{conf}$	the cost related to speed tracking performance	
F_d	traction force	
Ind_i	indices from perturbed driving cycles	
Ind_o	index from original driving cycle	
J_t	turbocharger inertia	7e-5 kg-m^2
K_{in}	intake manifold temperature	
K_{ex}	exhaust manifold temperature	
$MSDV2O$	mean squared deviation of index from original to perturbed driving cycle	
N_a	approximate total length of the process	
N_e	engine speed RPM	
N_t	turbine speed RPM	
P	the length of prediction horizon	3 step(1 step for 1 second)
P_m	output mechanical power of motor	
P_{ele}	input electrical power of motor	
P_{in}	intake manifold pressure	
P_{ex}	exhaust manifold pressure	
Q_{batt}	capacity of battery	6.5 A-h
R_{in}	battery internal resistance	

S_c	control step	
SOC	battery state of charge	
T_{req}	total requested torque	
T_e	engine output torque	
T_m	motor output torque	
V	vehicle speed	
V_{oc}	open circuit voltage	
V_{in}	volume of intake manifold	0.005 m^3
V_{ex}	volume of exhaust manifold	0.0008 m^3
V_{ref}	vehicle reference speed	
W_t	the gas power to drive turbine	
W_c	the consumed power on compressor	
γ	weight on the cost related to speed tracking performance	0.1
η_m	motor efficiency	
λ	conversion factor of SOC	3003 g/h
μ	penalty of SOC change in cost function	
ρ_{air}	air density	1.225 kg/m^3
ω_t	turbine speed rad/s	
PID	PID controller parameters in driver model	P=1,I=0.1,D=0

Chapter 5

Linearization methods in MPC-based energy management strategy

This chapter is part of the thesis that involves neither published nor submitted papers.

Since the computational effort is a big restriction to implement nonlinear MPC algorithms in real-time control, this chapter proposes linearization to convert the nonlinear problem in Chapter 3 into a linear programming (LP) problem.

5.1 Analytical model of HEV powetrain

The HEV models used in this chapter are basically the same as in Chapter 3. In order to conduct linearization, all the models need to be built as analytical expressions. Vehicle and battery model are already obtained in the right form as discussed

in previous chapters. However, the engine and electric motor model does not because part of these models are map-based. Thus, fitting methods should be adopted to obtain equation-based models.

5.1.1 Vehicle model

Referred to Section 3.2.1. The parameters of vehicle model are also the same.

5.1.2 Battery model

Referred to Section 3.2.3. The parameters of battery model are also the same.

5.1.3 Analytical models for engine

The turbine and compressor maps in the studied engine model describe the characteristics of turbocharger by turbine speed, mass flows and pressure ratios, and efficiencies of them. It is usually difficult to thoroughly reflect these characteristics with simple fitting equations, such as polynomial equations. Paper [1] suggests a lumped model using dimensionless variables to represent turbine and compressor maps. It shows fairly robust fitting performance for various turbochargers and the parameters used in the fitting equations are easy to adjust.

Compressor map fitting

Firstly, this section introduces two dimensionless variables Ψ_c and Φ_c to characterize the compressor map, which are named as pressure ratio related and mass flow related coefficients respectively. They are defined in Equ. 5.1 and 5.2. C_{pa} is the specific heat capacity of air at constant pressure, R_c is the radius of compressor. Π_c

is defined in Equ. 5.3 as the pressure ratio between the outlet and inlet of compressor. ω_t is the rotational speed of turbine shaft. γ_a is the specific heat ratio for air. R_a is the gas constant of air. T_{amb} and P_{amb} are ambient temperature and pressure.

$$\Psi_c = \frac{2C_{pa}T_{amb}(\Pi_c^{1-1/\gamma_a} - 1)}{R_c^2\omega_t^2} \tag{5.1}$$

$$\Phi_c = \frac{\dot{m}_c R_a T_{amb}/p_{amb}}{\pi R_c^3 \omega_t} \tag{5.2}$$

$$\Pi_c = \frac{P_{in}}{P_{amb}} \tag{5.3}$$

$$\left(\frac{\Phi_c}{kc_1}\right)^2 + \left(\frac{\Psi_c}{kc_2}\right)^2 = 1 \tag{5.4}$$

The relationship of two dimensionless variables are defined in Equ. 5.4. kc_1 and kc_2 are tuning coefficients of the "ellipse" model. The data sets of mass flow, pressure ratio and turbine speed in the original compressor map are used to find the two dimensionless variables, kc_1 and kc_2, by applying Nonlinear Regression approaches [2, 3] on the fitting problem. Fig. 5.1 shows the comparative results of Ψ_c, Φ_c curves between fitted model and raw data. The dimensionless variables associated with the raw data are plotted at each constant turbine shaft speed.

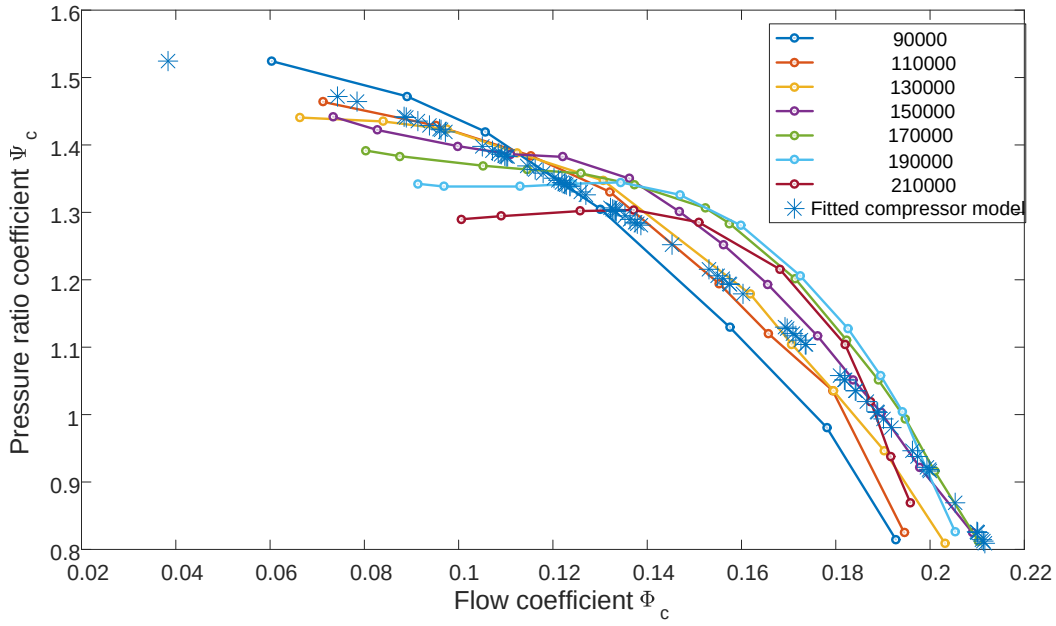

Figure 5.1: Comparison of Ψ_c VS Φ_c curves at different turbine speeds and the fitted ellipse model for compressor map

Compared to the original compressor map in Fig. 3.4, one obvious advantage of this model is that the influence of turbine speed is largely attenuated and multiple constant speed lines nearly converge to one line in Ψ_c-Φ_c domain.

Compressor efficiency can also be modeled as ellipses in Equ. 5.5. Q is a 2-by-2 positive semidefinite matrix, whose elements are obtained as $Q_{11} = 82.3203$, $Q_{12} = -3.0897$, $Q_{21} = -3.0897$, $Q_{22} = 0.1563$. $\eta_{c,max}$ is the maximum compressor efficiency according to the raw data. The fitting error is shown in Fig. 5.2, which is defined as the relative error by $\frac{Fitted\ value - Real\ value}{Real\ value}$.

$$\eta_c = \eta_{c,max} - X^T Q X \tag{5.5}$$

$$X = \begin{pmatrix} \dot{m}_c - \dot{m}_{c,max} \\ \Pi_c - \Pi_{c,max} \end{pmatrix} \tag{5.6}$$

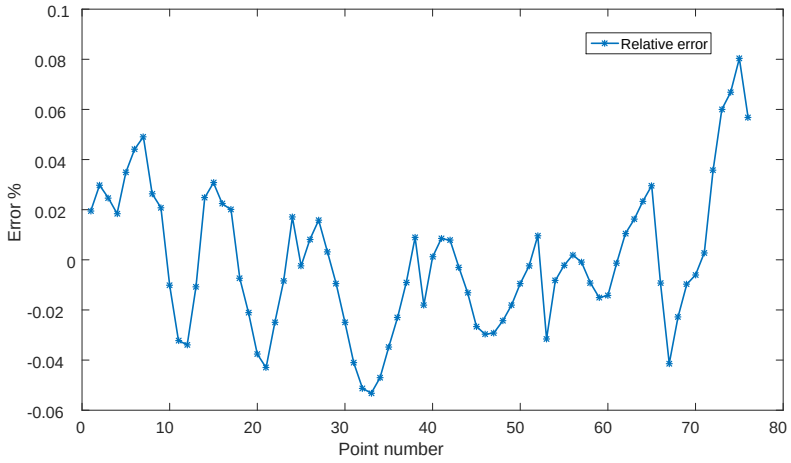

Figure 5.2: Relative error between raw data and fitted data for compressor efficiency using ellipse model

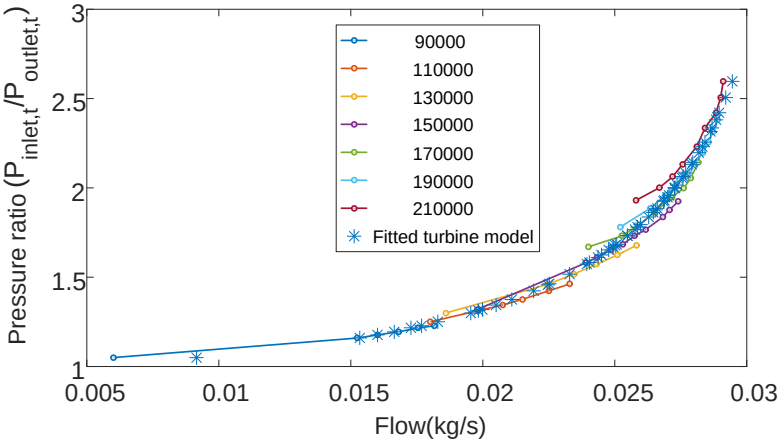

Figure 5.3: Comparison of mass flow VS pressure ratios curves at different turbine speeds and fitted model for turbine map

Turbine map fitting

The analytical model of turbine is, however, simpler. Because the constant speed lines in turbine map are close enough, it is straightforward to implement curve fitting in mass flow and pressure ratio domain. Generally, the model for this purpose is defined in Equ. 5.7. kt_1 and kt_2 are parameters to be fitted. Fig. 5.3 shows the results of fitting performance.

$$\dot{m}_t = kt_1\sqrt{1-(\frac{P_{amb}}{P_{ex}})^{kt_2}} \tag{5.7}$$

Turbine efficiency depends on the blade speed ratio (BSR) according to Equ. 5.8. BSR is defined as turbine blade tip speed divided by gas speed at the given turbine pressure ratio Π_t. BSR is described by Equ. 5.9. R_t is the radius of turbine blade. c_{pe} is specific heat capacity of exhaust gas at constant pressure. $c_{t,eff}$ is the coefficient according to mechanical losses. After careful curve fitting, $c_{t,eff}$ is obtained as 0.0019 and BSR_{opt} is 2.6785. The fitting error is shown in Fig. 5.4.

$$\eta_t = \eta_{t,max} - c_{t,eff}(BSR - BSR_{opt})^2 \tag{5.8}$$

$$BSR = \frac{R_t\omega_t}{\sqrt{2c_{pe}T_{ex}(1-\Pi_t^{1-1/\gamma_e})}} \tag{5.9}$$

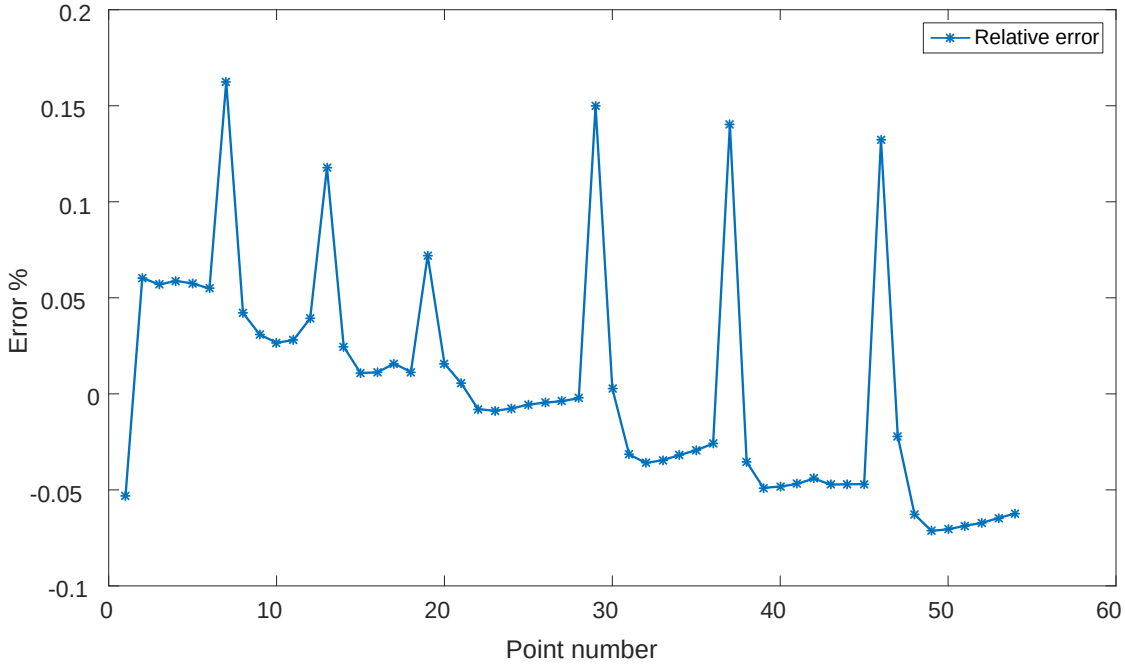

Figure 5.4: Relative error between raw data and fitted data for turbine efficiency using ellipse model

Engine torque map fitting

The original engine torque map is a 2-D map with regard to fuel injection mass and engine speed. At a constant engine speed, there is a linear relationship between fuel injection and engine torque , and it is described in Equ. 5.10. i is the index of each speed point on the map included in the set [1000,1100,1200,1300,1400,1500,1600,1700,1800, 2000,2200, 2500,2800,3000,3200, 3500]. For the speeds between two consecutive set-points, linear interpolation is utilized to calculate corespondent coefficients, which is shown in Equ. 5.11. k_{uf} and b_{uf} are calculated slope and bias for the given engine speed N_e. $k_{uf,i}$ and $b_{uf,i}$, $k_{uf,i+1}$ and $b_{uf,i+1}$ are those for the two speed set points N_i,

N_{i+1}, which N_e is in between.

$$T_{e,i} = k_{uf,i}u_f + b_{uf,i} \qquad i = 1, 2, ..., 16 \tag{5.10}$$

$$\begin{aligned} k_{uf} =& \frac{k_{uf,i} - k_{uf,i+1}}{N_i - N_{i+1}}(N_e - N_{i+1}) + k_{uf,i+1} \\ b_{uf} =& \frac{b_{uf,i} - b_{uf,i+1}}{N_i - N_{i+1}}(N_e - N_{i+1}) + b_{uf,i+1} \end{aligned} \tag{5.11}$$

$$T_e = k_{uf}(N_e)u_f + b_{uf}(N_e) \tag{5.12}$$

Then, with new coefficients the modeled torque is evaluated by Equ. 5.12 in which k_{uf} and b_{uf} are related to engine speed. Note that fuel injection mass u_f should also be limited by Equ. 3.18 as explained in Chapter 3.

5.1.4 Electric motor efficiency map fitting

The only "non-equation" part in electric motor model is its efficiency map. Thus, motor efficiency is fitted by a polynomial function with regard to speed and torque. The function is formulated as $y = a_1N_m + a_2T_m + a_3$ and the parameters $a_1 = 5.56e-06$, $a_2 = 1.87e-04$, $a_3 = 0.87$. The fitting performance is demonstrated in Fig. 5.5. Relative error is also defined as $\frac{Fitted\ value - Real\ value}{Real\ value}$.

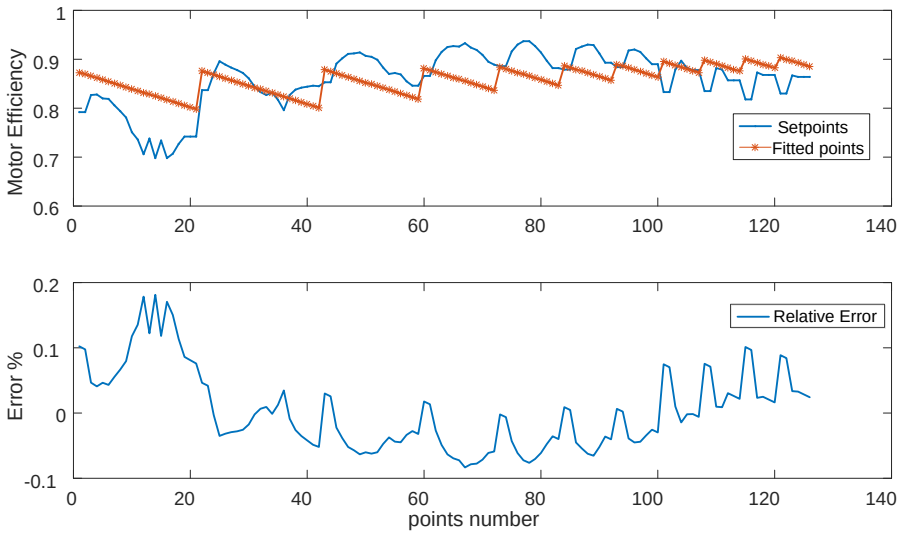

Figure 5.5: Comparison of fitted points and raw data points for motor efficiency

5.2 Linear MPC problem formation

5.2.1 Linearization and discretization

The problem stated in Section 3.3 from Equ. 3.19 to 3.28 is a constrained nonlinear programming problem. All the state and constraint equations should be linearized in order to simplify the problem. The four states are divided into two groups representing the states of system 1 and system 2. They are marked as $\boldsymbol{x_1} := [P_{in}, P_{ex}, N_t]$ and $\boldsymbol{x_2} := SOC$. The corresponding control variables for the two groups are $\boldsymbol{u_1} := [u_f, u_{wg}]$ and $\boldsymbol{u_2} := T_m$ respectively. The state equations are only denoted by symbols $\mathbf{f_1}$ and $\mathbf{f_2}$ for convenience, which are shown in Equ. 5.13.

$$\begin{cases} \dot{\boldsymbol{x}}_1 = \mathbf{f_1}(\boldsymbol{x_1}, \boldsymbol{u_1}) \\ \dot{\boldsymbol{x}}_2 = \mathbf{f_2}(\boldsymbol{x_2}, \boldsymbol{u_2}) \end{cases} \tag{5.13}$$

$$\begin{cases} \dot{\boldsymbol{x}}_{\mathbf{1}} = A_1 \boldsymbol{x}_{\mathbf{1}} + B_1 \boldsymbol{u}_{\mathbf{1}} + \boldsymbol{F}_{\mathbf{1}} \\ \dot{\boldsymbol{x}}_{\mathbf{2}} = A_2 \boldsymbol{x}_{\mathbf{2}} + B_2 \boldsymbol{u}_{\mathbf{2}} + \boldsymbol{F}_{\mathbf{2}} \end{cases} \tag{5.14}$$

$$\begin{aligned} A_1 &= \left(\frac{\partial \mathbf{f_1}}{\partial \boldsymbol{x}_{\mathbf{1}}}\right)_{x_{10},u_{10}}, \quad A_2 = \left(\frac{\partial \mathbf{f_2}}{\partial \boldsymbol{x}_{\mathbf{2}}}\right)_{x_{20},u_{20}} \\ B_1 &= \left(\frac{\partial \mathbf{f_1}}{\partial \boldsymbol{u}_{\mathbf{1}}}\right)_{x_{10},u_{10}}, \quad B_2 = \left(\frac{\partial \mathbf{f_2}}{\partial \boldsymbol{u}_{\mathbf{2}}}\right)_{x_{20},u_{20}} \\ \boldsymbol{F}_{\mathbf{1}} &= \mathbf{f_1}(\boldsymbol{x}_{\mathbf{10}}, \boldsymbol{u}_{\mathbf{10}}) - A_1 \boldsymbol{x}_{\mathbf{10}} - B_{10} \boldsymbol{u}_{\mathbf{10}}, \quad \boldsymbol{F}_{\mathbf{2}} = \mathbf{f_2}(\boldsymbol{x}_{\mathbf{20}}, \boldsymbol{u}_{\mathbf{20}}) - A_2 \boldsymbol{x}_{\mathbf{20}} - B_{20} \boldsymbol{u}_{\mathbf{20}} \end{aligned} \tag{5.15}$$

Equ. 5.14 and 5.15 shows the linearized state equations. x_{10}, u_{10} and x_{20}, u_{20} are the points where Taylor expansion is conducted for the two systems.

Then, the system states are discretized in time. Due to different frequencies of system 1 and system 2, the discretization uses different time intervals, which are $\Delta_1 = 0.001s$ and $\Delta_2 = 1s$. The state equations after discretization are shown in Equ. 5.16. In order to make the time intervals consistent for system 1 and 2, iterative calculating of system-1 state equation are performed to get new coefficients $\bar{A}_1$, $\bar{B}_1$ $\bar{F}_1$. It yields the system in Equ. 5.17 which will be used in the remaining part of this chapter. Note that the time intervals of the new system are all Δ_2. m is the iteration number calculated by $\frac{\Delta_2}{\Delta_1}$.

$$\begin{aligned} &\begin{cases} \boldsymbol{x}_{\mathbf{1}}(i+1) = \tilde{A}_1 \boldsymbol{x}_{\mathbf{1}}(i) + \tilde{B}_1 \boldsymbol{u}_{\mathbf{1}}(i) + \tilde{\boldsymbol{F}}_{\mathbf{1}} \\ \boldsymbol{x}_{\mathbf{2}}(i+1) = \tilde{A}_2 \boldsymbol{x}_{\mathbf{2}}(i) + \tilde{B}_2 \boldsymbol{u}_{\mathbf{2}}(i) + \tilde{\boldsymbol{F}}_{\mathbf{2}} \end{cases} \\ &\tilde{A}_1 = A_1 \Delta_1 + I, \quad \tilde{A}_2 = A_2 \Delta_2 + I \\ &\tilde{B}_1 = B_1 \Delta_1, \quad \tilde{B}_2 = B_2 \Delta_2 \\ &\tilde{\boldsymbol{F}}_{\mathbf{1}} = \boldsymbol{F}_{\mathbf{1}} \Delta_1, \quad \tilde{\boldsymbol{F}}_{\mathbf{2}} = \boldsymbol{F}_{\mathbf{2}} \Delta_2 \end{aligned} \tag{5.16}$$

$$\begin{cases} \boldsymbol{x_1}(i+1) = \bar{A}_1 \boldsymbol{x_1}(i) + \bar{B}_1 \boldsymbol{u_1}(i) + \bar{\boldsymbol{F}}_{\boldsymbol{1}} \\ \boldsymbol{x_2}(i+1) = \tilde{A}_2 \boldsymbol{x_2}(i) + \tilde{B}_2 \boldsymbol{u_2}(i) + \tilde{\boldsymbol{F}}_{\boldsymbol{2}} \end{cases}$$
$$\bar{A}_1 = \tilde{A}_1^m \tag{5.17}$$
$$\bar{B}_1 = \sum_{j=1}^{m} (A_1 \Delta_1 + I)^{j-1} B_1$$
$$\bar{\boldsymbol{F}}_{\boldsymbol{1}} = \sum_{j=1}^{m} (A_1 \Delta_1 + I)^{j-1} \boldsymbol{F_1}$$

Combining Equ. 3.20 and 5.12 yields the linearized equality path constraint in Equ. 5.18.

$$\begin{bmatrix} k_{uf}(\omega_e) & 0 \end{bmatrix} \begin{bmatrix} \boldsymbol{u_1}(i) \\ \boldsymbol{u_2}(i) \end{bmatrix} + b_{uf}(\omega_e) - T_{req} = 0 \tag{5.18}$$

Equ. 3.21 can further yield linear inequality Equ. 5.19 by substituting Equ. 3.13, 3.16 and 3.18.

$$\begin{bmatrix} -\frac{10^6 V_d \eta_{vol}}{120 AFR^* T_{in} R_a} & 0 & 0 \end{bmatrix} \boldsymbol{x_1}(i) + \begin{bmatrix} 1/30 & 0 \end{bmatrix} \boldsymbol{u_1}(i) \leq 0 \tag{5.19}$$

Also, states and controls should be within reasonable ranges as defined in Equ. 3.22 to 3.28. They can be written in matrix format as shown in Equ. 5.20 and 5.21.

$$\begin{bmatrix} P_{in,\min} \\ P_{ex,\min} \\ N_{t,\min} \\ SOC_{\min} \end{bmatrix} \leq \begin{bmatrix} 1 & 0 & 0 & 0 \\ 0 & 1 & 0 & 0 \\ 0 & 0 & 1 & 0 \\ 0 & 0 & 0 & 1 \end{bmatrix} \begin{bmatrix} \boldsymbol{x_1}(i) \\ \boldsymbol{x_2}(i) \end{bmatrix} \leq \begin{bmatrix} P_{in,\max} \\ P_{ex,\max} \\ N_{t,\max} \\ SOC_{\max} \end{bmatrix} \tag{5.20}$$

$$\begin{bmatrix} u_{f,\min} \\ u_{wg,\min} \\ T_{m,\min} \end{bmatrix} \leq \begin{bmatrix} 1 & 0 & 0 \\ 0 & 1 & 0 \\ 0 & 0 & 1 \end{bmatrix} \begin{bmatrix} \boldsymbol{u_1}(i) \\ \boldsymbol{u_2}(i) \end{bmatrix} \leq \begin{bmatrix} u_{f,\max} \\ u_{wg,\max} \\ T_{m,\max} \end{bmatrix} \tag{5.21}$$

Following the similar idea, cost function in Equ. 3.19 can be written as Equ. 5.22. P stands for the number of steps of prediction horizon.

$$\sum_{i=1}^{P} \begin{bmatrix} \frac{4N_e 10^{-6}}{120} & 0 \end{bmatrix} \begin{bmatrix} \boldsymbol{u_1}(i) \\ \boldsymbol{u_2}(i) \end{bmatrix} \Delta_2 + \mu(\boldsymbol{x_2}(P) - \boldsymbol{x_2}(1)) \tag{5.22}$$

From Equ. 5.17 to 5.22, a linear programming problem can be formed in prediction horizon($i = 1, 2, ...P$) and can be written in Equ. 5.23. z is the variable vector to be optimized and contains all states $x(i)$ and controls $u(i)$ sequences in the predicted time. This kind of problem can be solved by many methods, such as simplex, interior point algorithm etc.. [4]. In Matlab there is a linear programming solver called "linprog", which is adopted in this study.

$$\begin{aligned} min \quad & J = Hz \\ & Qz = 0 \\ & Wz \leq 0 \end{aligned} \tag{5.23}$$

5.2.2 Discussion on linearization

The last section mentioned that linearization is Taylor expansion at certain points of state and control variables. The linear time invariant problem formed in last section also implies that Taylor expansion can only be conducted at the first step of prediction horizon and the generated linear model coefficients should be constant during this

period of time. If any of the coefficient is a function of states or controls which is also time variant, it will become a nonlinear programming problem again and lose the meaning of linearization.

The state variables at first step are measurable and can be directly used to evaluate partial differentials. The control variables (u_f, u_{wg} and T_m) need to be selected carefully. The difficulty in here is that the prior knowledge of control law cannot be obtained before solving the problem, but some parameters of the problem are related to control law. Luckily, the ranges of all control variables at first step are obtainable so that one can choose the points within the ranges to do lineariaztion. Considering linear approximation in Equ. 5.24, the shorter distance is between u and a, the smaller error will be between actual and approximated function value. Here, assuming a uniform distribution of u in its range at every time step, a straightforward thinking is to choose a in the middle of this range.

$$f(u) = f(a) + f'(a)(u-a) + h_1(u)(u-a), \qquad \lim_{u \to a} h_1(u) = 0. \tag{5.24}$$

Fig. 5.6 shows a test simulation, which compares the three state trajectories of linear and nonlinear air path models. The linear model 1, 2, 3 are linearized at $u_{f0} = 20, 30, 10 mg/cyl$ and their control signals of u_f are all step signal 20mg/cyl. It is clear in the figure that the linear model in which u_{f0} and u_f are equal has the closest trajectory to the nonlinear model. Table. 5.1 lists the relative errors of each state at the end of its trajectory. The nonlinear model has no errors and the relative errors of the three linear models are calculated. Other parameters for testing in Table. 5.1 is identical with Fig. 5.6.

The linearization in electrical path (system 2) has a little difference. As shown in

Equ. 2.10 SOC dynamics is not a continuous function so that linearization should be applied to the two piecewise functions. Based on the similar idea in air path model, the value of T_{m0} where Taylor expansion is conducted are listed in Equ. 5.25. $T_{m,min}$ and $T_{m,max}$ are the same motor torque limits in Equ. 3.28.

$$T_{m0} = \begin{cases} abs(T_{m,min})/2 & T_m \geq 0 \\ abs(T_{m,max})/2 & T_m \leq 0 \end{cases} \tag{5.25}$$

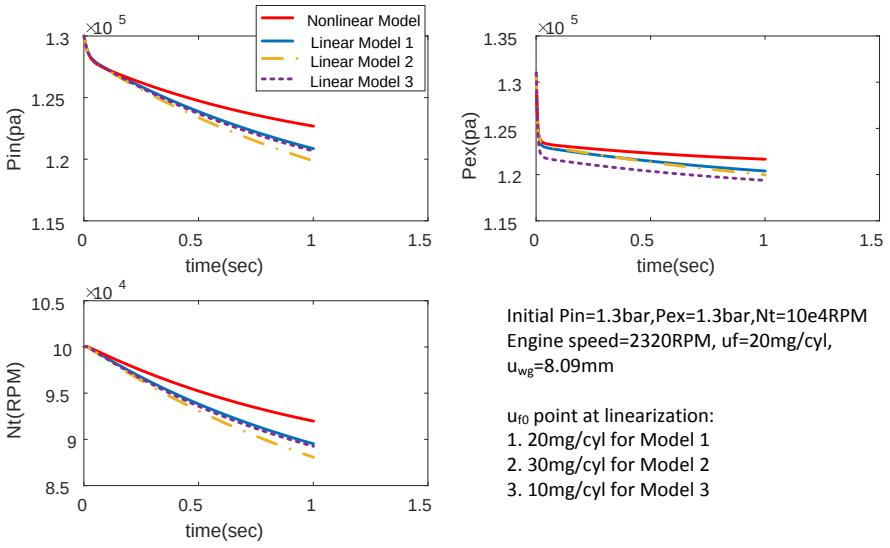

Figure 5.6: Comparison of trajectories of intake pressure,exhaust pressure and turbine shaft speed in linear and nonlinear air path models during step change of fuel injection mass

Table 5.1: Relative error between linear model 1, 2, 3 and nonlinear model for states of air path dynamics

Relative error %	Nonlinear Model	Linear Model 1	Linear model 2	Linear model 3
P_{in}	–	1.47	2.28	1.63
P_{ex}	–	1.07	1.40	1.89
N_t	–	2.67	4.25	2.97

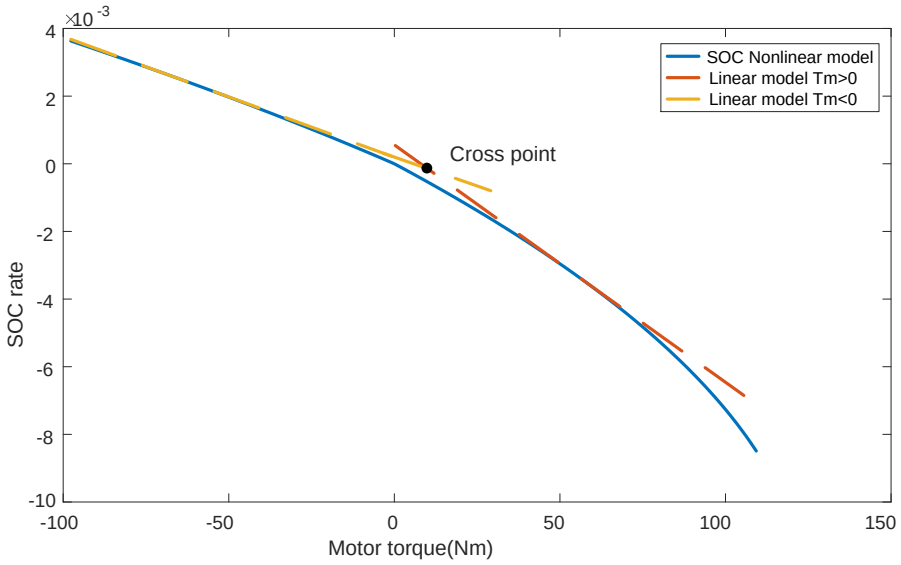

Figure 5.7: Nonlinear and piecewise linear models for SOC rate in the permissible range of motor torque

Fig. 5.7 shows the comparison of SOC change rates for nonlinear and linear SOC models. It can be seen that the error of linearization is larger during discharging than that in charging mode. This is in accordance with the results in paper [5] because

the battery parameters used in this study are also the same as those in the paper.

In order to demonstrate the effect of linearization on cost function, both original and linearized cost function in Equ. 3.19 are evaluated at the first step of prediction horizon(length $P = 1$) to obtain Fig. 5.8 and Fig. 5.9, which represent different requested torques 110Nm and 50Nm respectively. As a consequence of the unattainability of control variables in the remaining prediction horizon, the parameters of cost function cannot be completely evaluated for more than one step. The characteristic of cost function contains the dynamics of SOC so that it should also be linearized according to discharge and charge mode separately.

This chapter introduces two methods to deal with the conjunction between the two linear functions. The first one is that, using their cross point to make the curve continuous. It is shown as solid dot in Fig. 5.8 and 5.9 and it is denoted by "cross point". The second one is that, regardless of continuity, extending linear lines to the up-straight line of zero motor torque to obtain another point shown as triangles in the figures. To clarify the notation in the second method, it is denoted by "zero point". We can see that in Fig. 5.8 the cross point is closer to the expected minimum point in nonlinear cost function; however in Fig. 5.9 the zero point is a better approximation. To examine which method is better, comparative results in the driving cycle simulation between them will be discussed in Section 5.3.

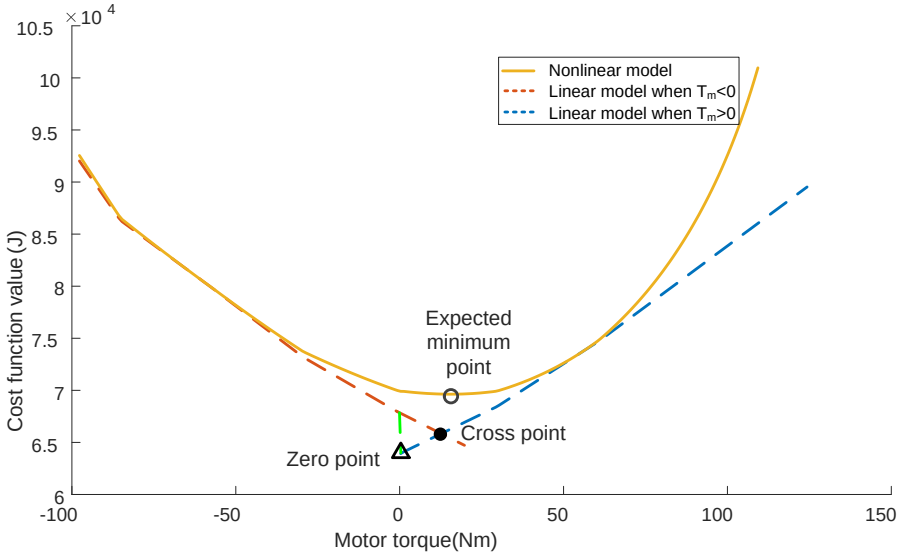

Figure 5.8: The cost function curves of nonlinear and linear models at the first step of prediction horizon. Engine speed N_e=2320RPM, request torque T_{req}=110Nm

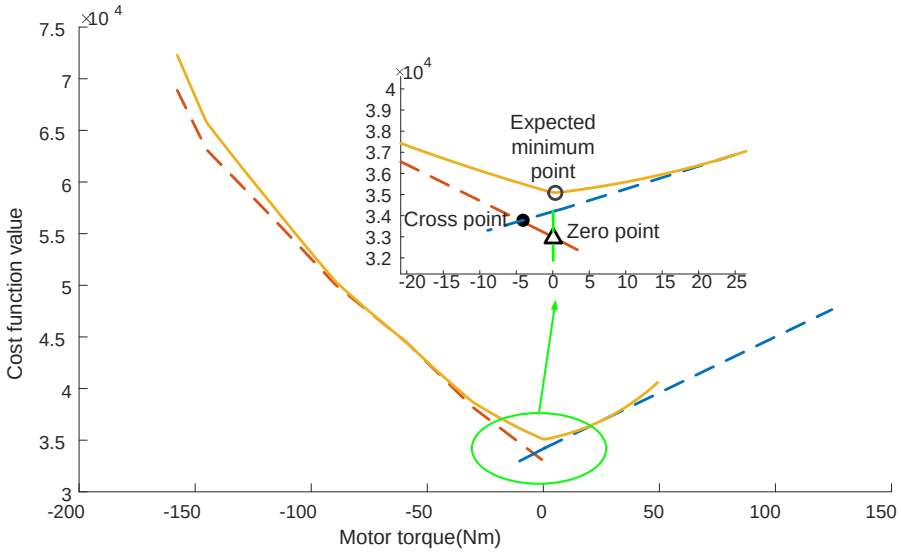

Figure 5.9: The cost function curves of nonlinear and linear models at the first step of prediction horizon. Engine speed N_e=2320RPM, request torque T_{req}=50Nm

Linearization using piecewise functions can introduce an issue in solving the linear programming problem. Because the functions that form the problem are determined by the sign of control variable T_m, one cannot know what kind of problem to solve before giving the control signal. The method of dealing with this issue is that we can form all the possible problems along multi-step prediction and compare the results of them to find the best solution. Basically, the number of different linear programming problems is exponentially related to number of predicted steps as in 2^P. It considers all the combinations of positive and negative T_m at each step in Table 5.2. Note that if $T_{m,min} \geq 0$ or $T_{m,max} \leq 0$, the problems defined in $[T_{m,min},0]$ or $[0,T_{m,max}]$ will be invalid and not a concern in the comparison.

Table 5.2: Defined range of motor torque in different linear programming problems

	Range of T_m at step 1	Range of T_m at step 2	Range of T_m at step 3	...
Problem 1	$[0,T_{m,max}]$	$[0,T_{m,max}]$	$[0,T_{m,max}]$	...
Problem 2	$[T_{m,min},0]$	$[0,T_{m,max}]$	$[0,T_{m,max}]$	...
Problem 3	$[0,T_{m,max}]$	$[T_{m,min},0]$	$[0,T_{m,max}]$	...
...	...	...	...	...

5.3 Case study

5.3.1 Comparison of MPC strategies using nonlinear and linear models

In this section, MPC based energy management strategies adopting both the nonlinear model and linear model are compared. They are labeled as "MPCNLPSC" and "MPCLPSC" in this section. The two strategies use the same engine ON/OFF and gear shifting method as discussed in Section 3.4. Also, the number of predicted steps are all set to 3 in both cases, and one step represents one second in real-time simulation. A third strategy that does not adopt transient but the steady-state engine model is introduced here as a benchmark. This strategy is identical with the one noted by "MBSC" and its control signals are implemented every one second. Here, the third strategy is still noted by "MBSC".

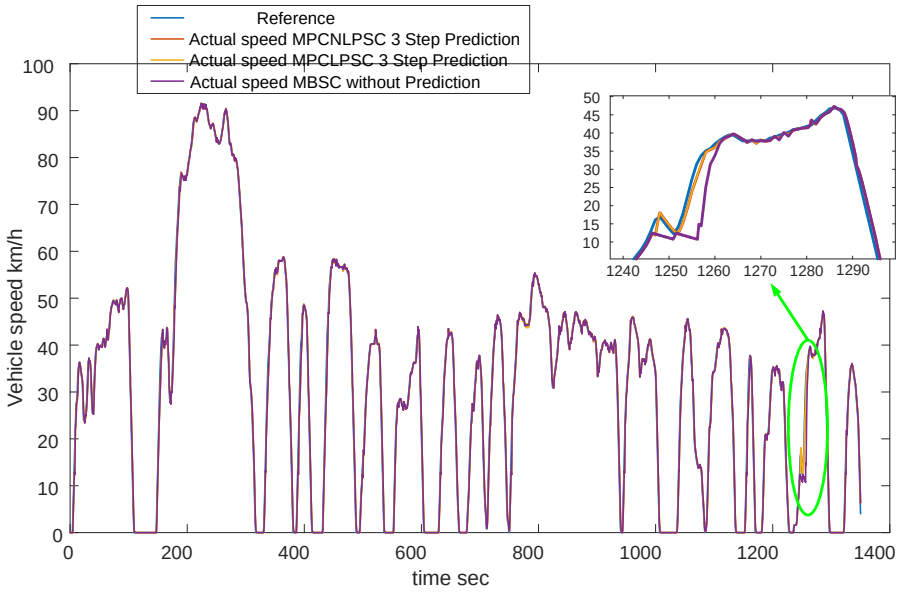

Figure 5.10: Comparison of vehicle speed tracking performance in MPCNLPSC, MPCLPSC and MBSC

Fig. 5.10 shows the vehicle speed tracking performance of the three strategies. Basically, in the whole driving cycle the actual vehicle speeds of the three cases can follow the reference UDDS cycle speed very well except for the time from 1240s to 1260s. The zoom-in figure in this time slot indicates that MBSC fails to catch up the reference speed. The reason is the same as discussed in Section 3.4, which is that the engine torque is not accurately predicted in MBSC. This phenomenon can be seen in Fig. 5.11 during time 1240s∼1260s. Meanwhile, due to the mismatch between actual speed and reference speed, the total requested torque has a sharp spike at time 1250s (see in Fig. 5.13). Then, the requested motor torque is very high at this time and exceeds the maximum torque that it can provide as shown in Fig. 5.12.

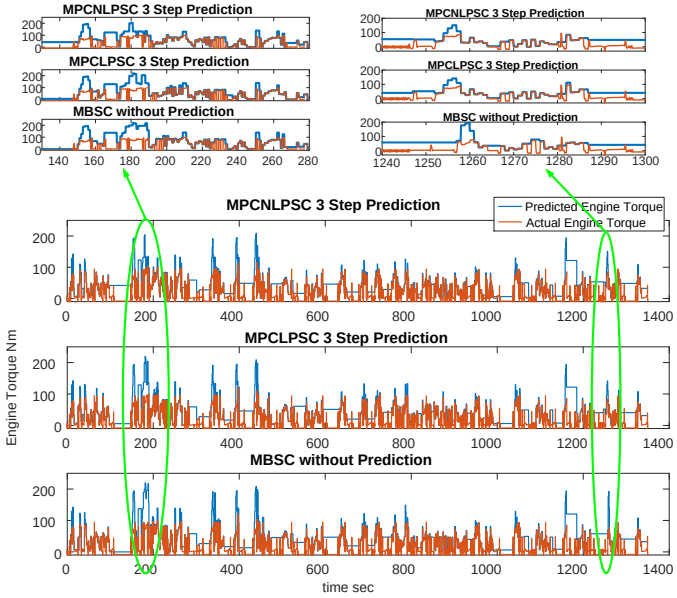

Figure 5.11: Comparison of requested and actual engine torque in MPCNLPSC, MPCLPSC and MBSC

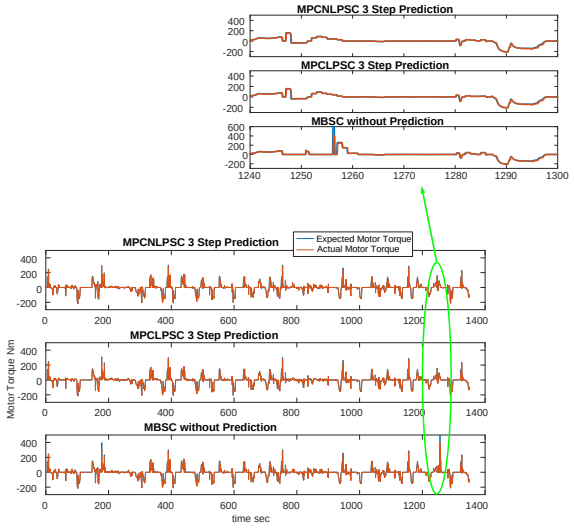

Figure 5.12: Comparison of expected and actual electric motor torque in MPCNLPSC, MPCLPSC and MBSC

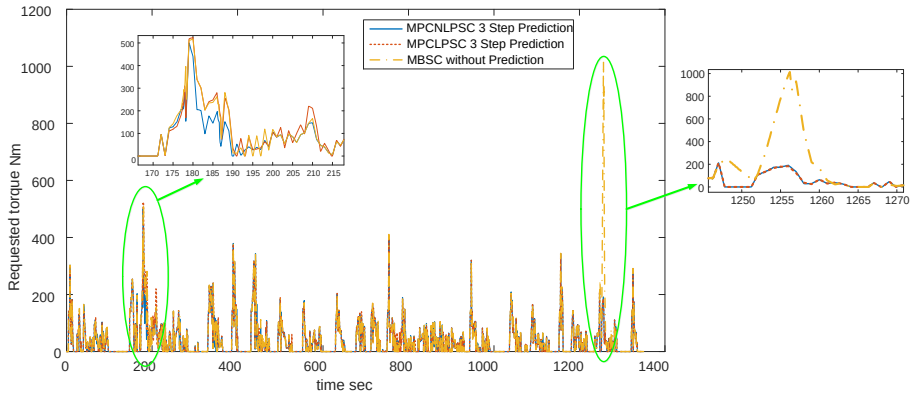

Figure 5.13: Comparison of the total requested torque in MPCNLPSC, MPCLPSC and MBSC

On the other hand, from Fig. 5.10 to 5.13, we can see that MPCNLPSC and MPCLPSC have extremely close trajectories of engine, motor torque and vehicle speed. This indicates the linearized model can give a good estimation on the major characteristics of the original nonlinear model in the energy management problem. In Fig. 5.14, it shows that SOC trajectories of MPCNLPSC and MPCLPSC have very small difference and almost reach to the same SOC point at the end of driving cycle. The error between the linear and nonlinear model leads to the change of engine and motor torque prediction and therefore the torque distribution generated from supervisory controller. However, SOC trajectory of MBSC has relatively large difference compared to the other two strategies, which is mainly caused by its inability of predicting driving cycle and engine transient torque. Fig. 5.15 compares the total fuel consumptions in the three cases. We can see MPCNLPSC consumes the least fuel and MPCLPSC comes the second. MBSC is the worst case among three in fuel consumption and also it has more battery usage by comparing the final SOC in each case.

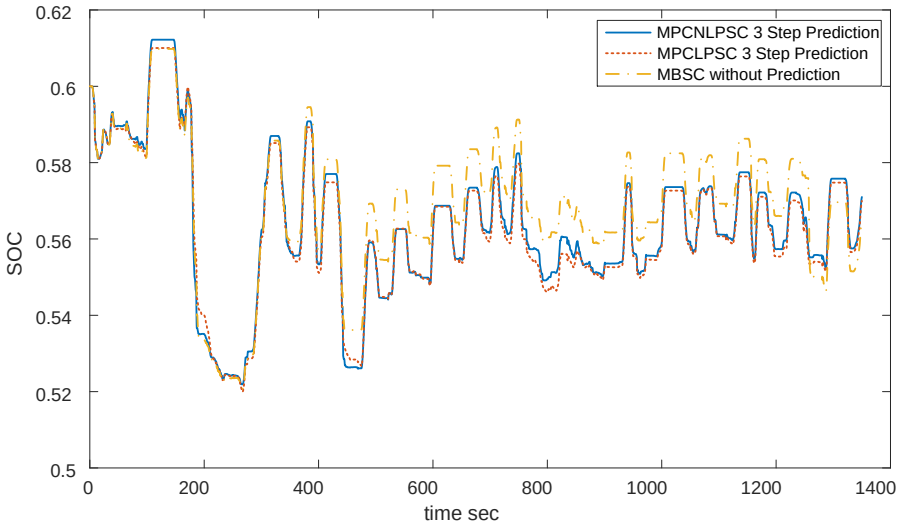

Figure 5.14: SOC trajectories in MPCNLPSC, MPCLPSC and MBSC

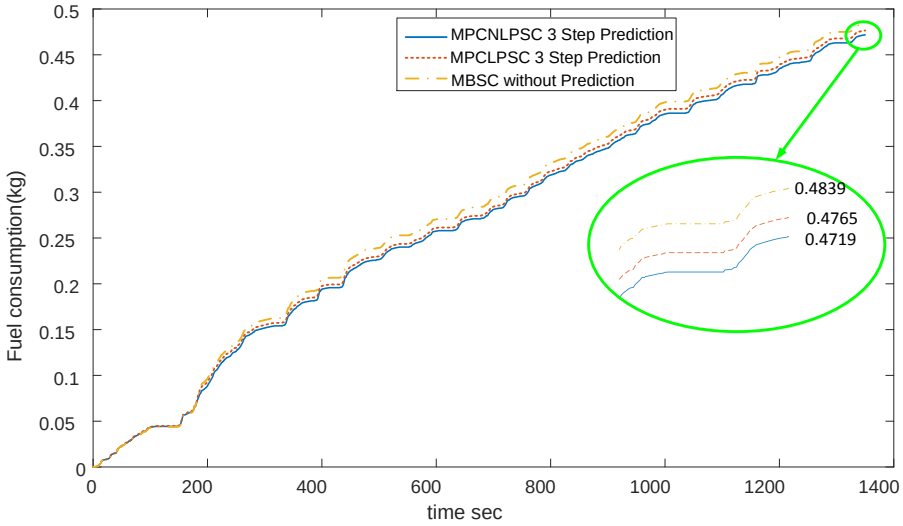

Figure 5.15: Engine fuel consumption trajectories in MPCNLPSC, MPCLPSC and MBSC

5.3.2 Comparison of two linearization methods

In Section 5.2.2, it proposed two different methods for connecting piecewise linearized functions. This section will apply those methods in cycle simulation and compare the performance of them with that using the nonlinear model. For convenience, the one using zero point is noted as "linear model one" and that using cross point is noted as "linear model two". Besides, the strategy using the nonlinear model is used as a benchmark and is supposed to have the best performance. It is still labeled as "MPCNLPSC". The three approaches all use 3 prediction step.

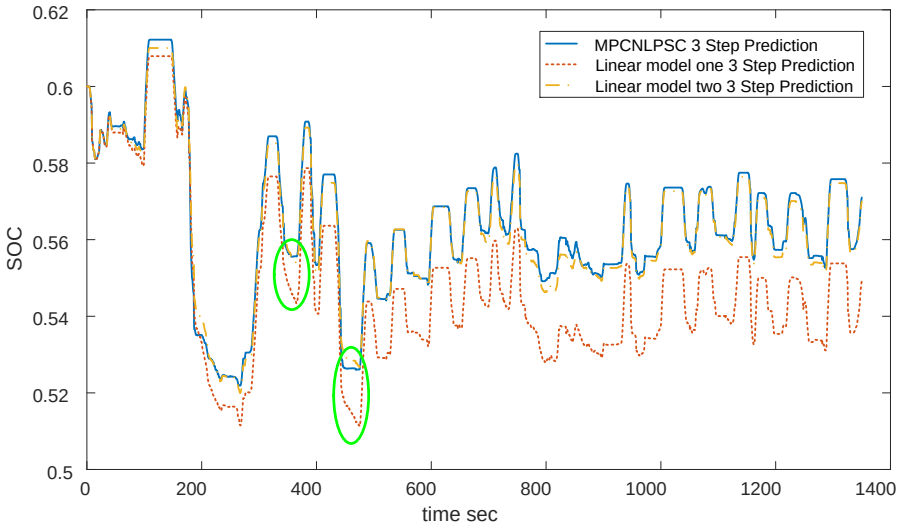

Figure 5.16: SOC trajectories in MPCNLPSC, linear model one and two

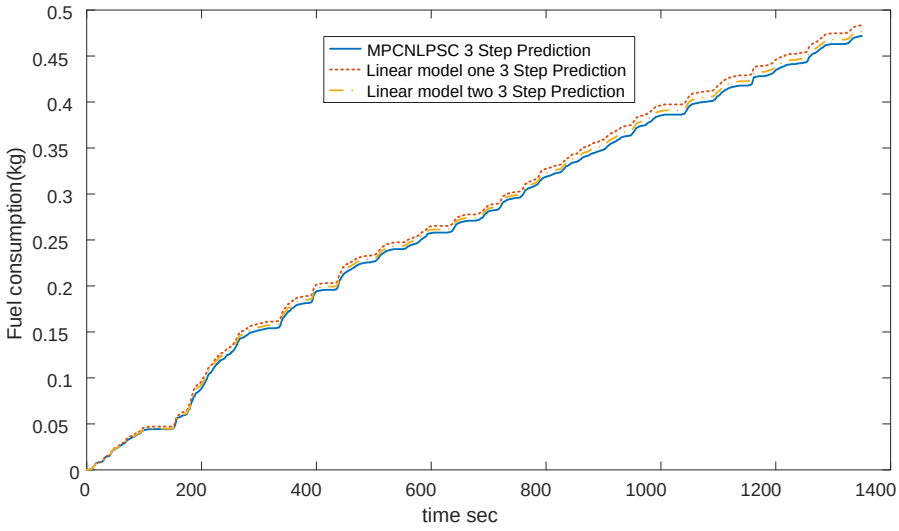

Figure 5.17: Fuel consumptions in MPCNLPSC, linear model one and two

Fig. 5.16 and 5.17 show the SOC and fuel consumption trajectories of the three strategies in UDDS cycle. Clearly, the difference between trajectories of the nonlinear model and "linear model two" is smaller than that between the nonlinear model and "linear model one". Meanwhile, by comparing fuel consumptions at the end of cycle, we can see that "linear model two" is also better that "linear model one". It means linearization method using cross point of two linear functions has better performance in cycle simulation. This is because it has more accurate approximation to the nonlinear model and can find control operations that are closer to MPCNLPSC.

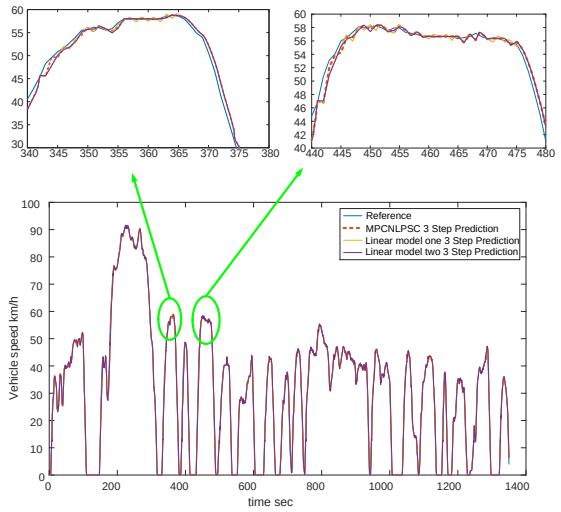

Figure 5.18: Comparison of vehicle speed tracking performances in MPCNLPSC, linear model one and two

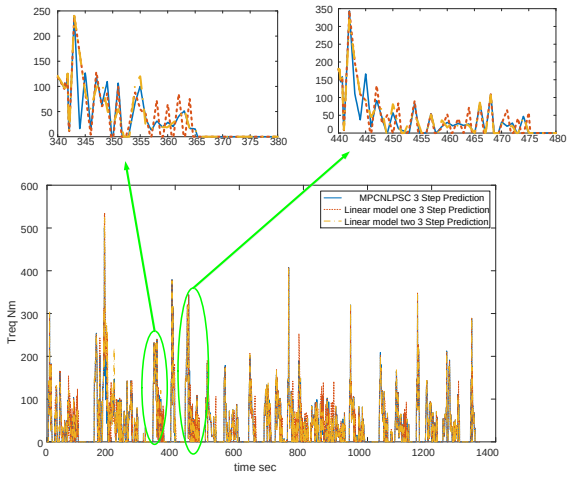

Figure 5.19: Comparison of total requested torque in MPCNLPSC, linear model one and two

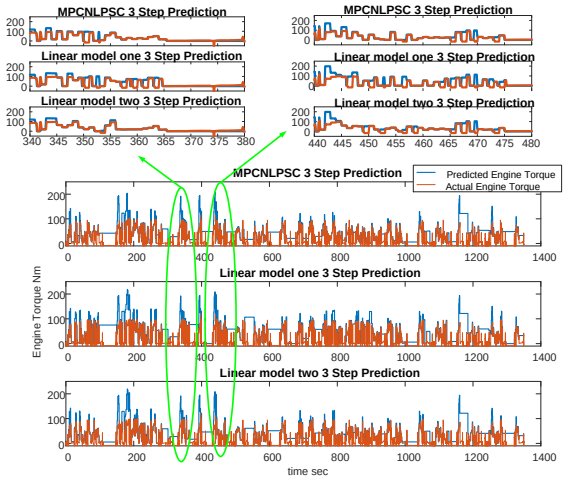

Figure 5.20: Comparison of engine requested and actual torque in MPCNLPSC, linear model one and two

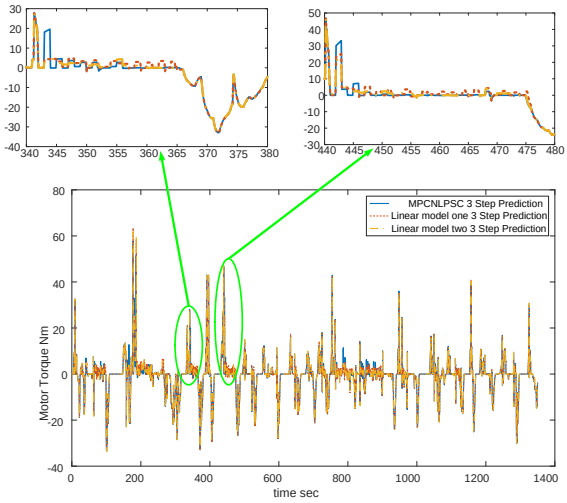

Figure 5.21: Comparison of requested motor torques in MPCNLPSC, linear model one and two

In Fig. 5.19, during time slots 340∼380s and 440∼480s, the red dash curve representing "linear model one" has more fluctuations than the other two curves. This

is mainly because the strategy with "linear model one" gives poorer estimation on engine output torque than the nonlinear model and "linear model two". Therefore, the requested torque cannot be fulfilled more accurately in "linear model one", and the actual vehicle speed of "linear model one" cannot follow the reference properly either (see in Fig. 5.18). Moreover, the upper-level PID controller needs to regulate the requested torque according to the speed error. As a result of the inaccurate engine torque prediction, the engine and motor torque commands calculated from supervisory controllers are also changed accordingly and shown difference among the three cases, which is demonstrated in Fig. 5.20 and 5.21. Particularly, in "linear model one" case during 340∼380s and 440∼480s, more motor torque is requested than other two cases which leads to more SOC consumption shown in green cycle in Fig. 5.16.

Through the comparative analysis between the three strategies, it is not difficult to see that the linear model with "cross point" has better approximation to the nonlinear model in UDDS cycle simulation than that with "zero point". Then, linear model with "cross point" should be considered as a potential alternative to the nonlinear model.

The major advantage of linearization is reducing the computational effort of searching optimal solutions. So in Fig. 5.22 it compares the computing time of predicting different number of steps for strategies using the nonlinear model and linear model two. The two problems are solved by giving the same initial conditions, including vehicle speed, gear ratio, requested torque at first step, state variables SOC, P_{in}, P_{ex}, N_t, etc.. Also, the same vehicle speed profile is applied on the two problems, and one predict step lasts for one second for both of them. Apparently, the

strategy with linear model has tremendous computational advantage over the nonlinear model, although up to 2^{10} linear programming problems need to be solved. One concern about solving piecewise LPs is that the number of problems increases exponentially. As prediction horizon becomes longer enough the computing time can be extremely large. Luckily, in our problem the prediction horizon is not necessarily very long according to the discussion in Section 4.5.

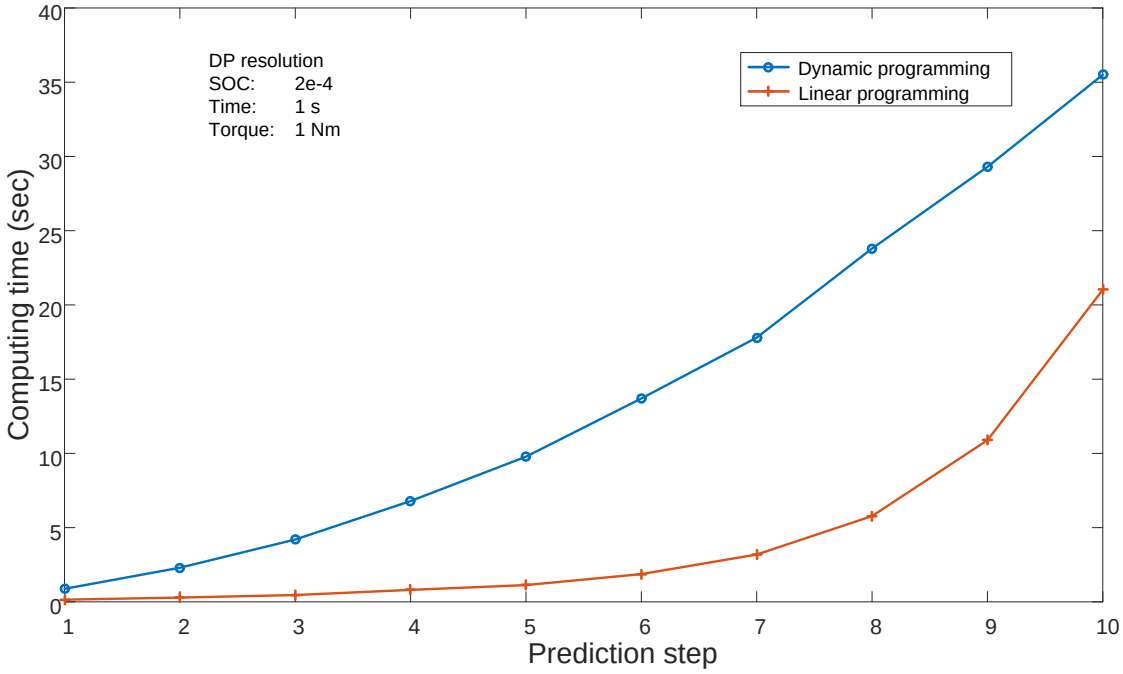

Figure 5.22: Comparison computing time in MPCNLPSC, linear model one

5.4 Conclusions

In order to reduce the computing time of solving nonlinear optimal control problem in the predict horizon, this chapter proposed a method by fully linearizing the models that are used in the problem. With linearized state equations, cost function

and constraint functions, the optimal control problem could be easily solved by converting it into a linear programming problem. Compared with dynamic programming algorithm, the linear method illustrated large advantage in saving computational resources.

Besides, this chapter proposed two different approaches to deal with the conjunction of two piecewise equations for the cost function. They used "cross point" and "zero point" to connect two consecutive linear functions, respectively. Results in driving cycle simulation showed that the approach using "cross point" had better accuracy of approximating the nonlinear model than the one using "zero point", and also revealed better fuel economy.

Reference

[1] Lars Eriksson. Modeling and control of turbocharged si and di engines. *Oil & Gas Science and Technology-Revue de l'IFP*, 62(4):523–538, 2007.

[2] Harvey J Motulsky and Lennart A Ransnas. Fitting curves to data using nonlinear regression: a practical and nonmathematical review. *The FASEB journal*, 1(5):365–374, 1987.

[3] Robert E Kass. Nonlinear regression analysis and its applications. *Journal of the American Statistical Association*, 85(410):594–596, 1990.

[4] George Dantzig. *Linear programming and extensions*. Princeton university press, 2016.

[5] Namwook Kim, Sukwon Cha, and Huei Peng. Optimal control of hybrid electric vehicles based on pontryagin's minimum principle. *IEEE Transactions on Control Systems Technology*, 19(5):1279–1287, 2011.

Chapter 6

Conclusions and future work

6.1 Summary

The fueling control and turbocharger technology are widely used in diesel engines aiming to reduce energy waste and improve engine efficiency. Fueling control includes coordinative control of fuel injection mass and timing. Usually, a maximum engine efficiency at the same engine speed and load can be reached by applying appropriate fuel injection timing. Turbocharger is the device that uses energy from waste gas to boost intake manifold pressure and increase power density and efficiency.

Traditional methods to deal with HEV energy management problems cannot make use of the potentials of those technologies because most of them use efficiency-map based engine model whose inputs are engine toque and speed. It implies that engine control variables cannot effectively influence engine torque production and therefore efficiency. The work in this thesis is mainly inspired by the idea that introducing detailed engine models to energy management strategy design can yield more benefits on HEV fuel economy. Since the objective system becomes complicated due to

the extra degrees of freedom and control variables, this thesis has proposed control techniques to properly deal with the fuel optimization in complex systems.

Chapter 2 proposed an on-line energy management method by using fueling control for a diesel engine. Engine torque was mapped by fuel injection mass and timing. The lowest BSFC at the same output torque and speed was able to be found by searching different combinations of two fueling control variables. This advantage was also exploited in PMP based energy management algorithm and demonstrated considerable ability of reducing fuel consumption from cycle simulation results.

Chapter 3 designed MPC based supervisory control strategy incorporating with engine torque transients. A detailed engine model was employed mainly to capture the air path dynamics that can restrict the engine torque response. Through the simulation results, the actual engine torque can be predicted more accurately than the steady-state engine model. Fuel consumption was further reduced due to the utilization of engine transient characteristics in the energy management strategy.

Chapter 4 proposed a novel control-step learning mechanism for model predictive control and implemented it in the problem proposed in Chapter 3. It exploited the information of control performance from the previous control horizon and used that to evaluate the dependability of control step settings. The control step was updated at the start of each prediction stage. The simulation results showed that the proposed method demonstrated an excellent balance between control performance and computational effort. Meanwhile, the results also proved the strategy's adaptability to the variation of driving cycle.

Chapter 5 mainly described linearization implementation on the energy management strategy in Chapter 3 in order to reduce the computational burden. By properly

linearizing all the functions in the optimal control problem, a linear programming problem was constructed and solved. Two linear methods to deal with function conjunctions were adopted to approximate the cost function, and they were also compared with the nonlinear method. The proposed one showed fairly close performance to the nonlinear method, but much less computing time.

6.2 Limitations and extensions of this research

The work in this thesis primarily focused on validating the idea of introducing engine control techniques to reduce HEV fuel consumption. Gear shifting strategy and clutch control were not particularly considered. For example, gear ratio and shift strategy were predefined according to engine speed and vehicle speed. The transient process during clutch engaging and disengaging was also neglected. So one of directions to extend this research is to employ gear shift and clutch related controls in fuel optimization problem.

Another potential improvement for this research could be implementing the proposed method in power split HEV. In this topology engine speed should be considered as another state instead of an exogenous variable coupled with vehicle speed in parallel topologies. It may bring more opportunities of fuel saving when utilizing transient models in the energy management strategy, since engine performance is sensitive to engine speed. The biggest challenge here is that engine speed is no longer measured. Thus, it need to be considered as a state in the optimal control problem. It will introduce great complexity to the algorithm design and computational effort of solving the problem.

A third extension will be focused on adding robustness to MPC based energy

management strategy. The scope of uncertainty issue in this research is limited to mismatch between MVMs and a tuned GT-SUITE model. In reality, an extensive robustness analysis is needed given the highly complex and uncertain nature of ICE dynamics. To this end, it is encouraging to introduce observer techniques to on-line estimate states or important parameters. It is expected to bring more reliable information to the optimal control problem.

Appendix A

This appendix includes a figure that demonstrates the gear shift strategy used in Chapter III and how to predict the gear ratio in the MPC based energy management strategies.

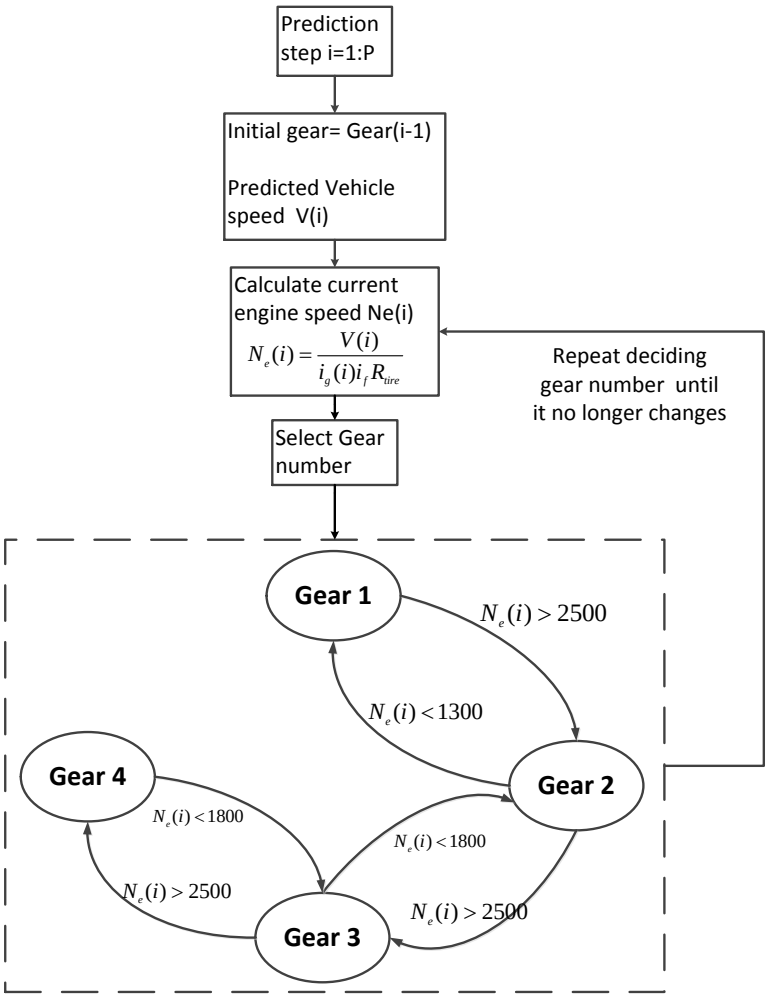

Appendix B

This appendix includes a figure that demonstrates the dynamic programming procedure in Chapter IV.

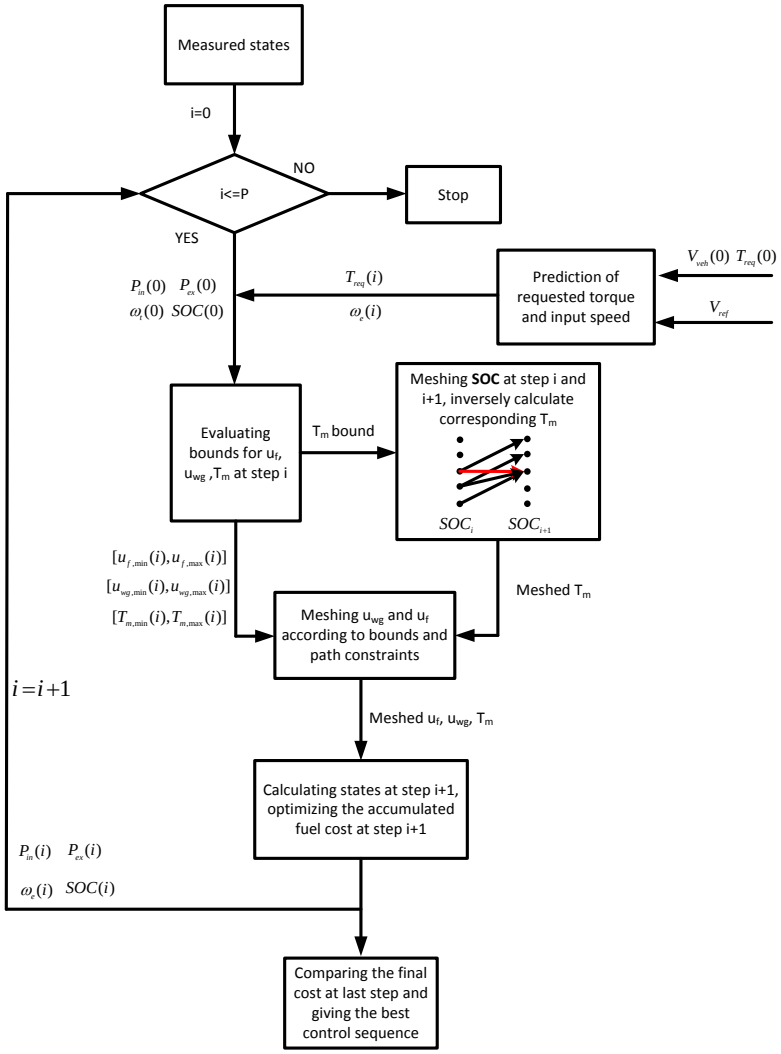

Main reference

[1] Mehrdad Ehsani, Yimin Gao, Stefano Longo, and Kambiz Ebrahimi. *Modern electric, hybrid electric, and fuel cell vehicles*. CRC press, 2018.

[2] Ali Emadi, Mehrdad Ehsani, and John M Miller. *Vehicular electric power systems: land, sea, air, and space vehicles*. CRC press, 2003.

[3] Ching Chue Chan. The state of the art of electric, hybrid, and fuel cell vehicles. *Proceedings of the IEEE*, 95(4):704–718, 2007.

[4] Lino Guzzella, Antonio Sciarretta, et al. *Vehicle propulsion systems*, volume 1. Springer, 2007.

[5] Kamil Çağatay Bayindir, Mehmet Ali Gözüküçük, and Ahmet Teke. A comprehensive overview of hybrid electric vehicle: Powertrain configurations, powertrain control techniques and electronic control units. *Energy Conversion and Management*, 52(2):1305–1313, 2011.

[6] Ching Chuen Chan, Alain Bouscayrol, and Keyu Chen. Electric, hybrid, and fuel-cell vehicles: Architectures and modeling. *IEEE transactions on vehicular technology*, 59(2):589–598, 2010.

[7] Ali Emadi, Kaushik Rajashekara, Sheldon S. Williamson, and Srdjan M. Lukic. Topological overview of hybrid electric and fuel cell vehicular power system architectures and configurations, 2005.

[8] Farzad Rajaei Salmasi. Control strategies for hybrid electric vehicles: Evolution, classification, comparison, and future trends. *IEEE Transactions on vehicular technology*, 56(5):2393–2404, 2007.

[9] Bernd M Baumann, Gregory Washington, Bradley C Glenn, and Giorgio Rizzoni. Mechatronic design and control of hybrid electric vehicles. *IEEE/ASME Transactions On Mechatronics*, 5(1):58–72, 2000.

[10] Clark G Hochgraf, Michael J Ryan, and Herman L Wiegman. Engine control strategy for a series hybrid electric vehicle incorporating load-leveling and computer controlled energy management. Technical report, SAE Technical Paper, 1996.

[11] Hyeoun-Dong Lee and Seung-Ki Sul. Fuzzy-logic-based torque control strategy for parallel-type hybrid electric vehicle. *IEEE Transactions on Industrial Electronics*, 45(4):625–632, 1998.

[12] Gino Paganelli, Sebastien Delprat, Thierry-Marie Guerra, Janette Rimaux, and Jean-Jacques Santin. Equivalent consumption minimization strategy for parallel hybrid powertrains. In *Vehicular Technology Conference, 2002. VTC Spring 2002. IEEE 55th*, volume 4, pages 2076–2081. IEEE, 2002.

[13] Chan-Chiao Lin, Huei Peng, Jessy W Grizzle, and Jun-Mo Kang. Power management strategy for a parallel hybrid electric truck. *IEEE transactions on control systems technology*, 11(6):839–849, 2003.

[14] Dimitri P Bertsekas, Dimitri P Bertsekas, Dimitri P Bertsekas, and Dimitri P Bertsekas. *Dynamic programming and optimal control*, volume 1. Athena scientific Belmont, MA, 1995.

[15] Avra Brahma, Yann Guezennec, and Giorgio Rizzoni. Optimal energy management in series hybrid electric vehicles. In *American Control Conference, 2000. Proceedings of the 2000*, volume 1, pages 60–64. IEEE, 2000.

[16] Yuan Zhu, Yaobin Chen, Guangyu Tian, Hao Wu, and Quanshi Chen. A four-step method to design an energy management strategy for hybrid vehicles. In *American Control Conference, 2004. Proceedings of the 2004*, volume 1, pages 156–161. IEEE, 2004.

[17] Chan-Chiao Lin, Huei Peng, and JW Grizzle. A stochastic control strategy for hybrid electric vehicles. In *American Control Conference, 2004. Proceedings of the 2004*, volume 5, pages 4710–4715. IEEE, 2004.

[18] Namwook Kim, Sukwon Cha, and Huei Peng. Optimal control of hybrid electric vehicles based on pontryagin's minimum principle. *IEEE Transactions on Control Systems Technology*, 19(5):1279–1287, 2011.

[19] Lorenzo Serrao, Simona Onori, and Giorgio Rizzoni. Ecms as a realization of pontryagin's minimum principle for hev control. In *American Control Conference, 2009. ACC'09.*, pages 3964–3969. IEEE, 2009.

[20] Michiel Koot, John TBA Kessels, Bram De Jager, WPMH Heemels, PPJ Van den Bosch, and Maarten Steinbuch. Energy management strategies for vehicular electric power systems. *IEEE transactions on vehicular technology*, 54(3):771–782, 2005.

[21] Hoseinali Borhan, Ardalan Vahidi, Anthony M Phillips, Ming L Kuang, Ilya V Kolmanovsky, and Stefano Di Cairano. Mpc-based energy management of a power-split hybrid electric vehicle. *IEEE Transactions on Control Systems Technology*, 20(3):593–603, 2012.

[22] Saida Kermani, Sebastien Delprat, Thierry-Marie Guerra, Rochdi Trigui, and Bruno Jeanneret. Predictive energy management for hybrid vehicle. *Control Engineering Practice*, 20(4):408–420, 2012.

[23] Metin Gumus, Cenk Sayin, and Mustafa Canakci. Effect of fuel injection timing on the injection, combustion, and performance characteristics of a direct-injection (di) diesel engine fueled with canola oil methyl ester- diesel fuel blends. *Energy & fuels*, 24(5):3199–3213, 2010.

[24] Cenk Sayin and Mustafa Canakci. Effects of injection timing on the engine performance and exhaust emissions of a dual-fuel diesel engine. *Energy conversion and management*, 50(1):203–213, 2009.

[25] Dennis N Assanis, Zoran S Filipi, Scott B Fiveland, and Michalis Syrimis. A predictive ignition delay correlation under steady-state and transient operation of a direct injection diesel engine. *Journal of Engineering for Gas Turbines and Power*, 125(2):450–457, 2003.

[26] Yu Wang and Zongxuan Sun. Dynamic analysis and multivariable transient control of the power-split hybrid powertrain. *IEEE/ASME Transactions on Mechatronics*, 20(6):3085–3097, 2015.

[27] Martin Sivertsson and Lars Eriksson. Optimal transient control trajectories in diesel–electric systemspart i: Modeling, problem formulation, and engine properties. *Journal of Engineering for Gas Turbines and Power*, 137(2):021601, 2015.

[28] Martin Sivertsson and Lars Eriksson. Optimal transient control trajectories in diesel–electric systemspart ii: Generator and energy storage effects. *Journal of Engineering for Gas Turbines and Power*, 137(2):021602, 2015.

[29] John B Heywood et al. Internal combustion engine fundamentals. 1988.

[30] G Fontana and E Galloni. Variable valve timing for fuel economy improvement in a small spark-ignition engine. *Applied Energy*, 86(1):96–105, 2009.

[31] Alain Maiboom, Xavier Tauzia, and Jean-François Hétet. Experimental study of various effects of exhaust gas recirculation (egr) on combustion and emissions of an automotive direct injection diesel engine. *Energy*, 33(1):22–34, 2008.

[32] Adnan Parlak, Halit Yaşar, Can Haşimoglu, and Ahmet Kolip. The effects of injection timing on nox emissions of a low heat rejection indirect diesel injection engine. *Applied Thermal Engineering*, 25(17-18):3042–3052, 2005.

[33] Martin Müller. Volumetric efficiency and pumping torque estimation and compressor recirculation control of turbocharged engines. *SAE International Journal of Engines*, 2(2009-01-0587):344–356, 2009.